DEVELOPMENT, CHARACTERIZATION AND PROCESSING OF MAGNETO-FLUORESCENT NANOSTRUCTURES FOR MULTIMODAL APPLICATIONS

Thesis submitted in fulfilment for the requirements of the Degree of

DOCTOR OF PHILOSOPHY

BY

DIPTI RAWAT

Enrollment Number: 166903

DEPARTMENT OF PHYSICS AND MATERIALS SCIENCE

JAYPEE UNIVERSITY OF INFORMATION TECHNOLOGY
WAKNAGHAT, DISTRICT SOLAN, H.P., INDIA

May 2022

TABLE OF CONTENTS

JAYPEE UNIVERSITY OF INFORMATION TECHNOLOGY
(Established by H.P. State Legislature vide Act No. 14 of 2002)
P.O. Waknaghat, Teh. Kandaghat, Distt. Solan - 173234 (H.P.) INDIA
Website : www.juit.ac.in
Phone No. +91-01792-257999 (30 Lines)
Fax : +91-01792-245362

DECLARATION BY THE SCHOLAR

I hereby declare that the work reported in Ph.D. thesis entitled **"Development, characterization and processing of magneto-fluorescent nanostructures for multimodal applications"** submitted at **Jaypee University of Information Technology, Waknaghat, Solan (H.P), India** is an authentic record of my work carried out under the supervision of **Dr. Ragini Raj Singh and Prof. (Dr.) P.B. Barman.** I have not submitted this work elsewhere for any other degree or diploma. I am fully responsible for the contents of my Ph.D. Thesis.

Dipti Rawat 31/05/2022

(Dipti Rawat)
(Enrollment No.: 166903)
Department of Physics and Materials Science,
Jaypee University of Information Technology, Waknaghat, Solan
(H.P), India
Date: 31/05/2022

JAYPEE UNIVERSITY OF INFORMATION TECHNOLOGY
(Established by H.P. State Legislature vide Act No. 14 of 2002)
P.O. Waknaghat, Teh. Kandaghat, Distt. Solan - 173234 (H.P.) INDIA
Website : www.juit.ac.in
Phone No. +91-01792-257999 (30 Lines)
Fax : +91-01792-245362

SUPERVISOR'S CERTIFICATE

This is to certify that the work reported in the Ph.D. thesis entitled **"Development, characterization and processing of magneto-fluorescent nanostructures for multimodal applications"** submitted by **Dipti Rawat** at **Jaypee University of Information Technology, Waknaghat, India,** is a bonafide record of her original work carried out under our supervision. This work has not been submitted elsewhere for any other degree or diploma.

Supervisors:

31-05-2022

(Dr. Ragini Raj Singh)
(Associate Professor)

&

31/05/2022

(Prof. Dr. P.B. Barman)
Department of Physics and Materials Science,
Jaypee University of Information Technology,
Waknaghat, Solan, H.P. India-173234
Date. 31/05/2022

Dedicated to
My Beloved
Parents

ACKNOWLEDGEMENT

Sometimes it is immensely difficult to put plethora of emotions into mere words. The same perplexity haunts my mind in penning down sincere thanks to all who have contributed in assorted ways in making this compilation a magnificent experience.

Out of a deep-seated conviction, it gives me immense pleasure to express my inveterate gratitude towards my Ph.D. supervisor ***Dr. Ragini Raj Singh*** *for her constructive criticism and proper visualization in a magniloquent way due to her professional acumen and fineness at every stage of this study. She has been in front of my eyes for more than four years motivating me, taking up my new challenges every day, tackling them with all her grit and determination and always thriving to come out victorious. Her unflinching support has always encouraged me to go ahead especially when I felt it was not possible. She shall remain best teacher, my best adviser and my best friend with all my secrets. "Thank you, ma'am," I couldn't have asked for better supervisor than you.*

Besides, I owe gratuitous thanks to ***Prof. (Dr.) P. B. Barman*** *my guide & Head of the Department who has always been there with his fatherly hand, whenever I needed it the most. His excellent monitoring and counseling have always energized me to work hard. Without his necessary scolds and important advices, it would have been impossible for this naughty child to be on track and compile this thesis.*

I express my gratefulness to ***Prof. (Dr.) Rajendra Kumar Sharma*** *(Vice Chancellor),* ***Prof. (Dr.) Vinod Kumar*** *(Advisor & Ex- Vice Chancellor),* ***Prof. Samir Dev*** *(Director and Academic Head),* ***Prof. (Dr.) Ashok Gupta*** *(Dean Academics & Research)* ***Maj Gen Rakesh Bassi*** *(Registrar & Dean of Students) and* ***Mr. Sanjay Kumar Verma*** *(Assistant Registrar Academics) who had been very supportive and helpful throughout this journey. I have lots of praises and appreciation to all my learned teachers* ***Prof. (Dr.) Sunil Kumar Khah, Prof. (Dr.) Vineet Sharma, Dr. Rajesh Kumar, Dr. Surajit Kumar Hazra & Dr. Sanjeev Tiwari*** *Department of Physics and Materials Science, JUIT. I also thanks* ***Prof. (Dr.) Pankaj Sharma & Dr. Dheeraj Sharma.*** *Heartfelt thanks to* ***Mr. Kamlesh Mishra, Mr. Ravendra Tiwari and Mr. Deepak Singh*** *for being so compassionate and supportive though this journey.*

A good support system is important to survive and staying sane in Ph.D. A special thanks to my partners in crime of all the fun times ***my friends Ekta, Sanjay & Rahul*** *without*

whose endless gossips and fights this journey would never have been possible. I am grateful to seniors from our research group ***Dr. Asha Sharma, Dr. Rajinder Kumar, Dr. Hitanshu Kumar, Dr. Ankush Thakur & Mr. Shiv Kumar Sharma*** *for standing by me whenever I needed the most. I also thank all of my research colleagues.*

My vocabulary fails and I actually become bankrupt when it comes to express my gratitude and thankfulness towards my mains, my father and mother and my younger siblings. Whether it is the way you comforted me when I was down, or the way in which your hugs magically wiped out my frowns. Mom & dad, you have been there every moment, to make sure my life turned out this way. It is actually impossible to thank you adequately for everything you've done, from loving me unconditionally to raising me to this day. I could not have asked for better parents or role-models.

I would like to express my special thanks to ***Dr. Tiratha Raj Singh*** *for encouraging me by his positive attitude towards every facet of life.*

Thank you, God, for giving me patience, perseverance and determination to work through all these years and indeed, throughout my life.

Lastly, I want to state for any errors that may remain in this work, the responsibility is entirely my own while the expertise in this study belongs to those acknowledged above.

A big thank you my Lady love! My guide ***Dr. Ragini Raj Singh***

Thanks to all of you!

Dipti

Abstract

The seed mediated aqueous growth approach has been developed for the selective and controlled fabrication of “core-shell nanostructures (CSNs)”, that combines various functionalities of “ferromagnetic-core” and “semiconducting-shell” within a solo material that has tuneable magnetic and fluorescence characteristics. CSNs have been developed in a way that can meet the demand for “magneto-fluorescent” properties in a single unit. Shell thickness and core in the nanostructured particle have been tuned precisely. The current research focuses on CSNs made of soft ferrite and hard ferrite. CSNs were compared in a study where the core was annealed at two different temperatures. A new assembly of “magneto-fluorescent” CSNs was created using a magnetic core of Nickel Zinc ferrite (Soft ferrites) and Strontium Hexaferrite (Hard ferrite) and a fluorescent semiconducting shell of CdS quantum dots (QDs) which is having brilliant “physical and chemical” characteristics of discrete magnetic core and discrete QD’s shell. These CSNs have been created to address several constraints of the iron-oxide based “magneto-fluorescent” or “magneto-plasmon nanostructures” that had previously been examined in the field. CdS QDs were successfully generated on the SHF/NZF surface, and “UV–visible spectroscopy, photoluminescence spectroscopy, VSM, and FTIR” revealed a clear add-on with good stability and intactness of core and shell. To explore the elaborative impacts of different structural combinations of CSNs in order to reach the optimal arrangement with “high-luminescence” and “magnetic” results, optical and magnetic characterizations were done. The magnetic/nonmagnetic nanostructure interface was examined. Despite the “non-magnetic (di-magnetic)” nature of CdS QDs, that is obviously an "optically-active" and "magnetically-inactive" material, considerable “exchange-bias” has been seen in some of the CSNs. The existence of "exchange-bias" has been confirmed by a shift in the susceptibility derivative as well as a change in "magnetic-anisotropy." High coercivity in SHF/CdS CSNs demonstrates the SHF's hard-magnetic character, which persists even after core-shell formation, and implies CSNs formation, as there is no interaction between the core and shell interface. Hysteresis derivatives provide information about new structural properties. Finally, stable and efficient CSNs were successfully formulated, with no exchange bias or shift. These “magneto-fluorescent nanostructures” have capability to be used in “spintronics”, as well as “*In-vivo* drug administration”, diagnosis, and imaging applications in the nanomedicine sector, according to recent findings/discoveries.

LIST OF ACRONYM AND ABBREVIATIONS	
Symbol	**Abbreviations**
g	Grams
h	Hours
ml	Millilitres
α	Alpha
β	Beta
λ	Lambda
H_c	Coercivity
K	Anisotropy
^oC	Degree Celsius
%	Percent
nm	Nanometre
CSNs	Core-Shell nanostructures
QDs	Quantum Dots
MPs	Magnetic nanoparticles
NPs	Nanoparticles
DSM	Derivative Spectroscopy methods
PL	Photoluminescence
NZF	Nickel Zinc ferrite
SHF	Strontium hexa ferrite
CdS	Cadmium Sulphide
UV-Vis	Ultraviolet Visible Spectroscopy
SFD	Switching Field Distribution
VSM	Vibrating Sample Magnetometer
EDX	Energy dispersive X-ray Spectroscopy
XRD	X-ray Diffractometer
FT-IR	Fourier Transform infrared Spectroscopy
HR-TEM	High resolution transmission electron spectroscopy

LIST OF FIGURES

LIST OF TABLES

LIST OF PUBLICATIONS

PUBLICATIONS IN INTERNATIONAL REFEREED JOURNALS:

1. **Rawat D,** Singh RR. "Avant-grade magneto/fluorescent nanostructures for biomedical applications: Organized and comprehensive optical and magnetic evaluation". ***Nano-Structures & Nano-Objects.*** 2021 Apr 1; 26:100714. Cite score -7.8.
2. **Rawat D,** Sethi J, Sahani S, Barman PB, Singh RR. "Pioneering and proficient magneto fluorescent nanostructures: Hard ferrite based hybrid structures". ***Materials Science and Engineering: B.*** 2021 Mar 1;265:115017. (I.F-4)
3. **Rawat D,** Barman PB, Singh RR. "Corroboration and efficacy of Magneto-Fluorescent (NiZnFe/CdS) Nanostructures Prepared using Differently Processed Core". ***Scientific reports.*** 2019 Oct 22;9(1):1-2. (I.F-4.3)
4. **Rawat D,** Barman PB, Singh RR. "Multifunctional magneto-fluorescent NiZnFe@ CdS core-shell nanostructures for multimodal applications". ***Materials Chemistry and Physics***. 2019 Jun 1;231:388-96. (I.F-4)
5. **Rawat D,** Kumar R, Barman PB, Singh RR. "Experimental and theoretical verification of cation distribution and spin canting effect via structural and magnetic studies of NiZnCo ferrite nanoparticles." ***Journal of the Australian Ceramic Society.*** 2022 Feb 22*; 58*(1), 101-111. (I.F-1.5)

PUBLICATIONS IN CONFERENCE:

Rawat Dipti, Asha Kumari, and Ragini Raj Singh. "Structural and luminescent properties of multifunctional nanostructures." **In *AIP Conference Proceedings*. *AIP Publishing,*** (2018).

Rawat Dipti, and Ragini Raj Singh. " Development of High Coercivity/High Fluorescence Hybrid nanostructures." **Letters in Applied Nanobioscience,** (2022).

PUBLISHED BOOK CHAPTER

Rawat Dipti, Asha Kumari, and Ragini Raj Singh. "Synthesis and Functionalization of Magnetic and Semiconducting Nanoparticles for Catalysis.". **In book: *Functionalized Nanomaterials for Catalytic Application, (*2021)** Online ISBN: 9781119809036 ***Wiley Online Library***

CONFERENCES/WORSHOPS ATTENDED:

1. **National conference on Advanced Materials and Nanotechnology** (AMN-2018) held at JIIT, (AIP conference proceeding), 2018.
2. **Third International** Conference **on Advanced Materials (ICAM 2019)** August 09-11, 2019 at Mahatma Gandhi University, Kottayam, Kerala, India, 2019.
3. **Virtual** International Conference **on Environmental Sustainability and Smart Agriculture"** Organized by Centre of Excellence in Sustainable Technologies for Rural Development [CESTRD], Department of Biotechnology and Bioinformatics, Jaypee University of Information, Technology, INDIA on 18th- 19th September 2020
4. **Ist National Students** Conference **on Spectroscopy (NSCoS 2020)**, jointly organized by SciRox (Science Club), Guru Nanak Dev University, Amritsar and Chemical Research Society of India from 16 - 17 October 2020.
5. **Online Workshop on Rietveld** Refinement Method **organized by UGC-DAE Consortium for Scientific Research,** Mumbai Centre in association with Indore Centre from 22 - 24 September 2020.
6. **National Seminar on Raman Spectroscopy** organized by Vigyan Bharat, November12, 2019 Himachal Pradesh University Biological Society (HUBS), Himachal Pradesh, India.
7. **Five Days National** Workshop **on** Innovative **Techniques of Characterization, Optimization & Data Analysis (ITCOD)**", from 8th -12th July'19 Chitkara University, Rajpura, Punjab, India.
8. **National Hands-on** Workshop **on Characterization Techniques and Nanomaterials Applications**" from20th to 25th January 2020, Chitkara University, Punjab.

CHAPTER-1

INTRODUCTION TO MULTIFUNCTIONAL MAGNETO-FLUORESCENT CORE-SHELL NANOSTRUCTURES

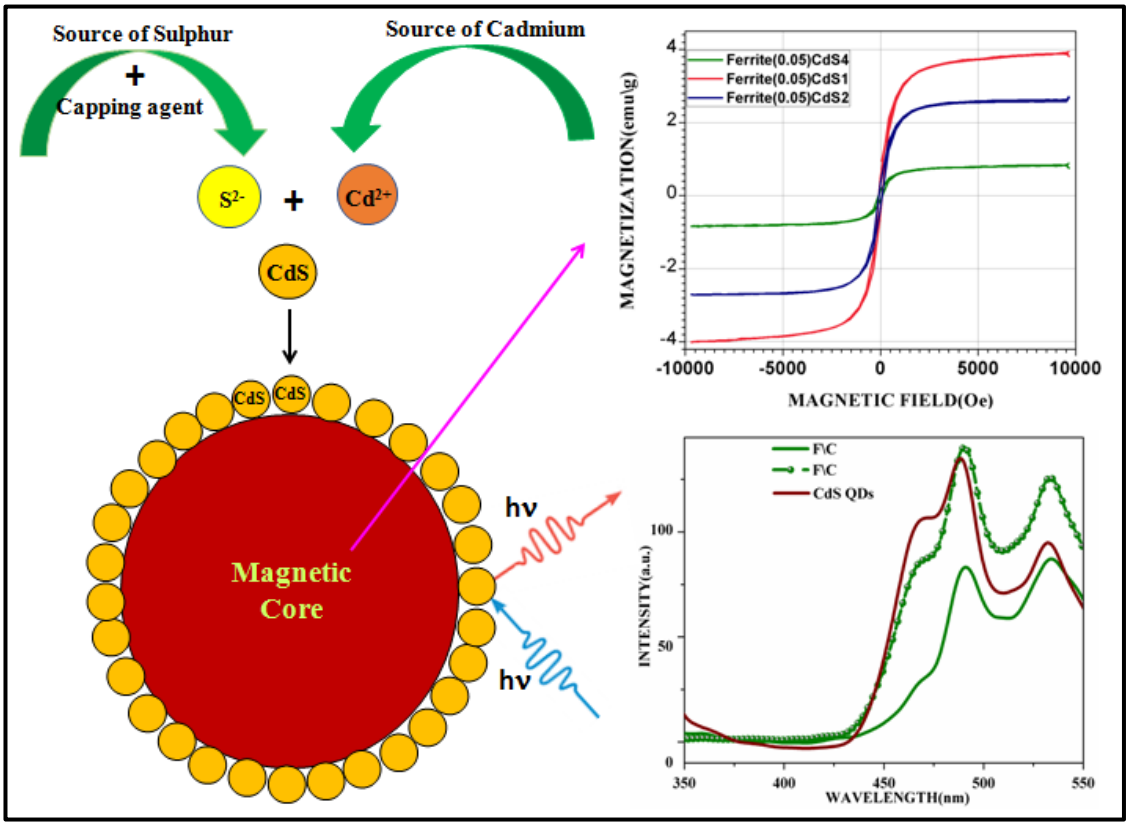

1.1 Introduction

The "seed mediated aqueous growth approach" has been flourish for the selective and controlled fabrication of core-shell nanostructures (CSNs), which combine the various functions of ferromagnetic core and semiconducting shell in a single material with tuneable fluorescence and magnetic characteristics. The magnetic cores of "Nickel Zinc Ferrite (NZF) and Strontium Hexa Ferrite (SHF) and the fluorescent semiconducting shells of CdS quantum dots (QDs)" were used to create a new set of magneto-fluorescent CSNs. This magnet within semiconductor model satisfies the necessity for simultaneous targeting and tracking, proving to be a valuable tool in "targeted drug delivery, serving as a dual-modal imaging probe for in vivo multiphoton cell-dynamics, MRI, and cell-sorting applications". Figure 1.1 shows the emblematic illustration for the CSN.

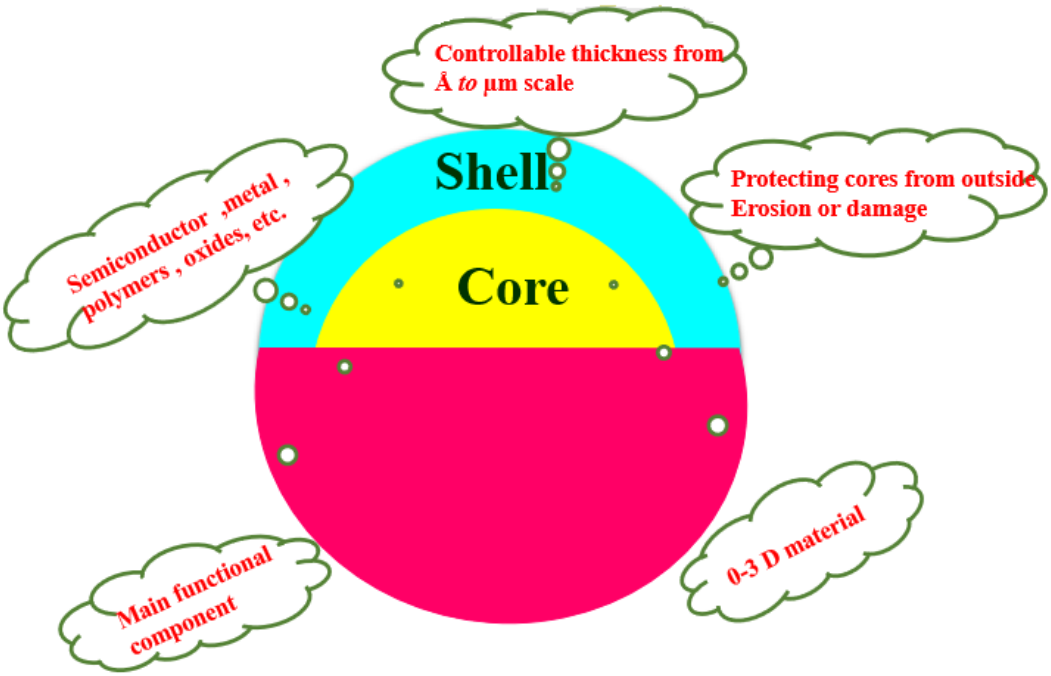

Figure 1.1: Shows the schematic for the CSNs

In general core–shell nanoparticles (NPs) are biphasic materials with different entities joined together using various mechanisms. The unusual features, that these particles can display as a result of the assortment of core and shell material, geometry, and design have raised the interest of researchers. [1-4]. The general classification of CSNs is shown in Figure 1.2 based on material type (along with the most common synthetic methods) and shell parameters.

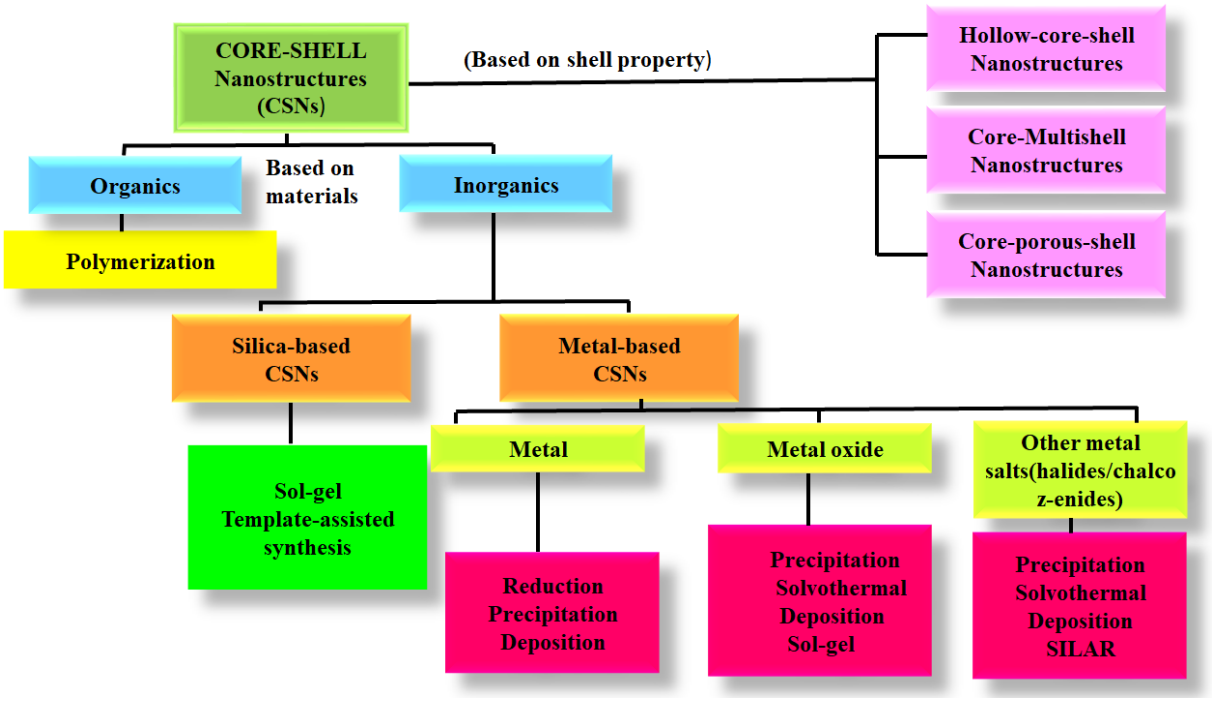

Figure 1.2: The general classification of CSNs is shown in Figure 2 based on material type (along with the most common synthetic methods) and shell parameters

Core-shell designs have been engineered to boost the activity, stability, or the reactive sites for their wide-ranging series of applications in memory devices, biomedicine, catalysis and in spintronic [5-36]. Multifunctional core shell nanostructures have emerged as today's most exciting smart materials. New nanoparticles with an optical signature in addition to supplementary physical qualities are predominantly relevant, allowing optical addressability for particle tracking and monitoring as well as other properties [37-40]. Integrating noble metals and semiconducting QDs into a structure is an effective way to impart optical characteristics at the nanoscale. Interesting features have resulted from interfacial regions because of the interaction in between different natured entities [41]. Management of an electron's charge and spin at the atomic level in magnetic/nonmagnetic heterostructures could lead to the advancement of QDs-based spintronic devices, demanding additional research. Recently experimentation on bulk “Fe/MgO” has yielded fascinating interfacial results, owing to the suggested existence of FeO interactions at the surface [42-44]. In bulk materials these effects are very weak and are not detected in bulk magnetic measurements. Due to the spatial confinement, the magnetic exchange interaction in this device will be more strongly perturbed than in its bulk equivalent. This can impact the electronic structure and lead to charge carrier exchange between the ferromagnetic and semiconducting phases observing these effects in

FM/nonmagnetic systems [45]. The structural and compositional characteristics of CSNs that can affect their catalytic capabilities are shown in Figure 1.3.

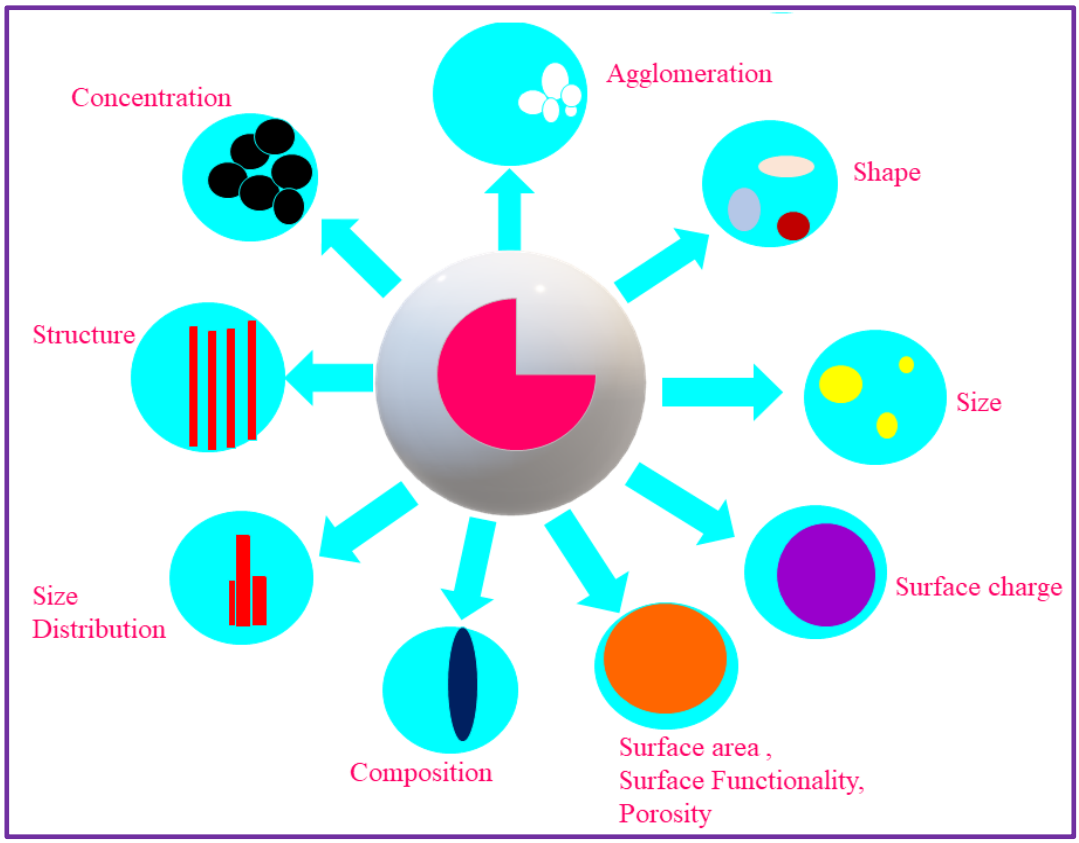

Figure 1.3: CSNs structural and compositional characteristics that influence catalytic capabilities

1.2 Magnetic Nanoparticles

Nanoparticles are materials having a diameter of 1 to 100 nanometres (nm). When a magnetic field is applied to a material, it causes it to respond. “Ferromagnetic, paramagnetic, diamagnetic, antiferromagnetic, and ferrimagnetic” are the diverse categories. The net magnetic moment in ferromagnetic materials is due to unpaired electrons. When a ferromagnetic substance is positioned in a magnetic field, the magnetic moments mark-up sideways the path of the applied field, resulting in a significant net magnetic moment. When a paramagnetic substance is positioned in applied field, it produces a feeble over-all magnetic moment. While the diamagnetic materials have zero magnetic moment because of no unpaired electrons.

Antiferromagnetic materials are made up of distinct atoms at different lattice positions. Atoms have equal magnetic moments but opposing magnetic directions, resulting in a net magnetic moment of zero. Ferrimagnetic materials are also made up of various atoms

but with antiparallel magnetic moments residing on different lattice sites. Antiferromagnetic materials have net magnetic moments that do not balance out because their magnitudes are different, resulting in a net impulsive magnetic moment. Ferrimagnetic materials, on the other hand, have net magnetic moments that do not balance out because their magnitudes are different. Antiferromagnetic and ferrimagnetic materials act similarly to ferromagnetic materials in a magnetic field [46]. Figure 1.4. depicts the many types of magnetism, with arrows indicating spin orientations.

Some geometric and magnetic data, regarding magnetic nanoparticles (MNPs) must be understood in order to better analyse MNPs. The form, size, crystal structure and composition, of nanoparticles are all considered as geometric data. Under magnetic parameters we have "saturation magnetization, residual magnetization, coercivity, and blocking temperature". The magnetic characteristics of MNPs are dominated by the following aspects, which give them certain distinctive properties:

(a) Effects of "finite size"

(b) "Surface effects", such as dangling bonds, oxidation, the presence of surfactants, surface strain, etc.

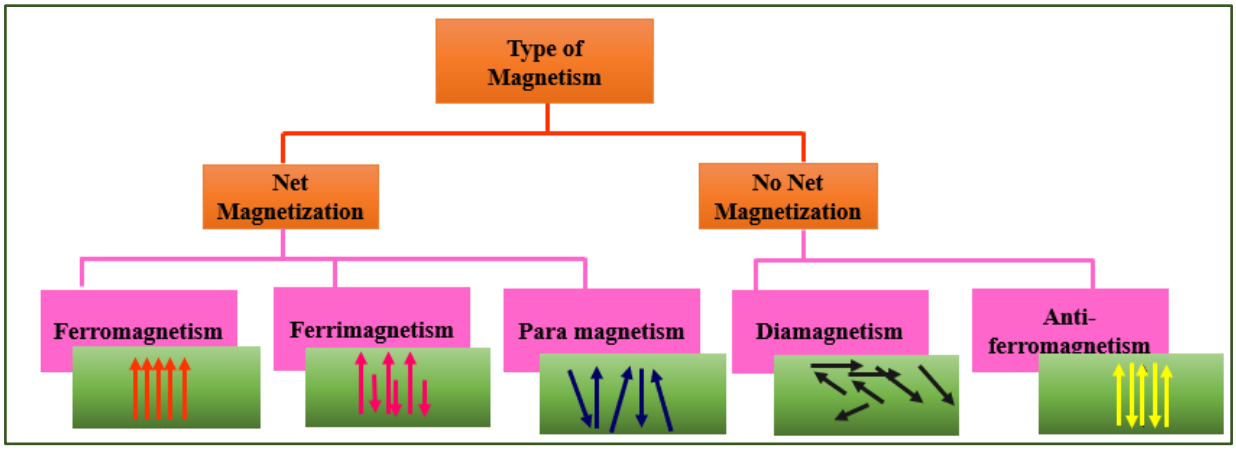

Figure 1.4: Shows the different type of magnetism with nature of the spin orientation

1.2.1 Ferrite Nanoparticles

Thousands of years ago, ferrites were discovered [47-48]. Magnetic iron-ore was used to make the primary compass (Fe_3O_4). The ferrite spinel structure has 24 cations (Fe^{2+}, Zn^{2+}, Co^{2+}, etc.) and 32 O^{2-} anions per unit cell. There are 96 potential cation sites in unit cell ("64

T-sites and 32 O-sites positions"). T- sites are a fraction of the magnitude of O-sites. The "spinel structure" is often described as a cubic closed-pack of oxygen ions with the formula $(A)[B_2]\ O_4$.

The spinel structure of ferrite can be written as $(Me^{2+})\ [Fe_2^{3+}]\ O_4$ in general. The trivalent cations are Fe^{3+} cations, while the divalent cations are Me^{2+} cations. The Fe^{3+} atoms occupy octahedral positions in the "spinel structure" while Me^{2+} atoms occupy tetrahedral positions although Me^{2+} is found in a tetrahedral configuration. $(Me^{2+})\ [Fe^{3+}{}_2]\ O_4$, which is regular "spinel structure", is obtained at x = 0. When x = 1, the inverse spinel structure (Fe^{3+}) $[Me^{2+}Fe^{3+}]\ O_4$ is obtained [49-50]. Ferrites of various sizes and synthesis processes have been shown to have different structure, content, cation distribution, and magnetic characteristics than their bulk counterparts [51-58]. "In spinel ferrites, all cations' magnetic moments are oriented in the same direction at the octahedral lattice locations. All cations on the tetrahedral lattice sites have magnetic moments that are antiparallel to those on the octahedral lattice sites, but directed in the same direction" [59].

It was revealed that the magnetization of Zn ferrite nanoparticles is substantially higher than that of its bulk form. [60]. Due to its regular spinel structure, $ZnFe_2O_4$ exhibits paramagnetic behaviour in its bulk form, with Zn^{2+} ions inserted entirely at T sites. The Fe^{3+} cations and Zn^{2+} cations are distributed among the O and T lattice sites as a result of this migration, there is change in their magnetic properties as well. When the Zn/Fe ratio exceeds 0.5, the magnetization of Zn ferrite is found to decline [61]. The difference in net magnetic moments between the two sublattices grows, leading to improved net magnetization in the NPs which is contrary of what was detected.

Despite many researches on these ferrite nanoparticles' magnetic properties, their magnetic behaviour is still unknown. Recent research on ferrite nanoparticles [62] and Fe nanoparticles coated with magnetic oxides [63] has revealed a complex image of the nanoparticles. Several discoveries suggest that surface structure faults could cause magnetic disorder to spread into the centre within a given layer thickness. These discrepancies may be because of the factors affecting the magnetic behaviour of nanoparticles, comprising particle size distribution, surface and interior flaws, and dipolar and exchange interactions between particles the nanoparticle has a range of spin distributions due to the exchange coupling between the surface and the centre.

The presence of point defects in ferrites, such as oxygen and cation vacancies at the O-sites, may structurally compensate for their non-stoichiometry. As a consequence of the non-stoichiometry of the zinc ferrites' composition, many factors emerge, including shifts in the "lattice parameter", the emergence of "secondary phases", and the emergence of "point defects".

Since Zn^{2+} ions can be incorporated at the O-sites, the composition of Zn ferrite nanoparticles is non-stoichiometric. However, particle size, synthesis processes, and ambient variables are said to influence the degree of inversion [64]. The dispersal of cations within nanoparticles' spinel lattice has been found to affect nanoparticle [65-67].

In "high resolution electron microscopy (HRTEM)" micrographs, the edge of an agglomeration of NPs with dimension of 8 nm revealed normal crystallinity [51]. The magnetic properties of these nanoparticles were greatly affected by this structure. NPs with dimensions larger than 3 nm exhibit ferrimagnetism, according to H-M measurements. All nanoparticles did not attain saturation magnetization at ambient temperature and high magnetic fields. This is due to the occurrence of magnetically deceased coating that becomes more visible as the sample size decreases [68].

"In a study on nanostructure nickel ferrite ($NiFe_2O_4$) with grain sizes of 13, 20, 26, and 51 nm, the smallest and biggest grain-sized samples demonstrated surface spin canting and shift in coordination of the iron ions at T-sites and O-sites with reduction in grain size" [69]. All samples with the smallest grain size had a lower magnetization value, which was related to conversion of structure from "inverse" to "mixed spinel" form [69]. The magnetic properties of the NPs changes as a result of nanoparticle size, synthesis methods, and synthesis conditions. It's critical to comprehend how different fabrication methods and particle sizes might alter the magnetic characteristics of ferrite nanoparticles.

1.2.1.1 Soft Ferrites

Soft ferrites can easily modify their magnetization and function as magnetic field conductors since they have a low coercivity. They're used to make ferrite cores, which are effective magnetic cores for high-frequency inductors, transformers, and antennas, as well as other microwave parts, in the electronics sector. Soft ferrites are magnetic materials with a high resistivity and a low coercivity field. With a small amount of magnetic field, they can be quickly magnetized and demagnetized. Since soft ferrites have a low coercivity and a high

retentivity, they can easily reverse magnetization without losing much energy, have low hysteresis losses, and have low eddy current losses [70]. These materials are best for high frequency applications because of low loss. MgZn ferrite, CoZn ferrite, NiZn ferrite, and other soft ferrites are common examples. They are used in “transformer cores, magnetic recording heads, inductors, and other applications because of their high saturation magnetization, high resistivity, and high permeability” [71]. Crystal structure for the nickel zinc ferrite designed with the help of Vista software [72] is shown in Figure 1.5.

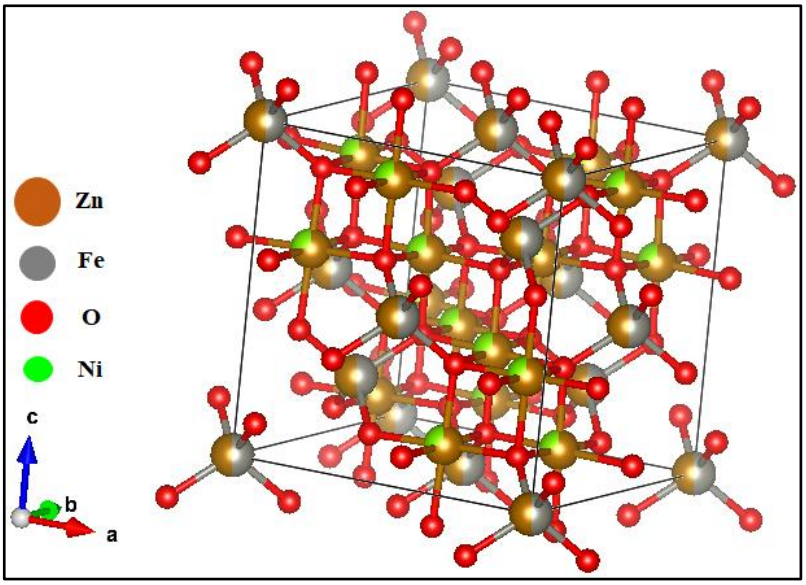

Figure 1.5: Crystal structure for the Nickel Zinc ferrite

1.2.1.2 Hard Ferrites

“Hard ferrites” also called permanent magnets are tough to demagnetize due to their strong coercivity. Permanent magnets are utilised in refrigerator magnets, loudspeakers, and small electric motors, among other applications. [73-74]. After magnetization, hard ferrite is a permanent magnet with a strong coercivity and retentivity rating. The most important property of hard ferrite is its high coercivity, which is described as a high value of magneto crystalline anisotropy energy. They can't be magnetized or demagnetized with a tiny amount of field, and they need a lot of fields to be magnetized or demagnetized. These ferrites have high magnetic permeability and are made up of barium, iron or strontium oxides. Hard magnets have a higher propensity to store more magnetic field than iron and are commonly used in household items, especially as refrigerator magnets. Strontium ferrite, barium ferrite, and cobalt ferrite are examples of hard ferrites that are used as permanent magnets, magnetic

recording media, and so on. Figure 1.6. Shows the crystal structure for the strontium hexaferrite designed with the help of Vista software [75].

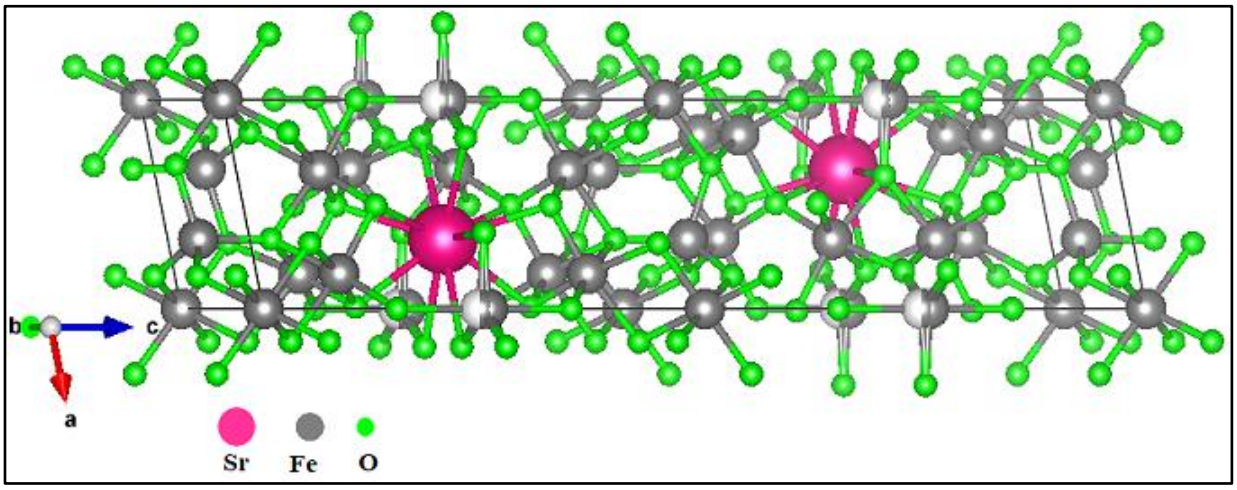

Figure 1.6: Crystal structure for the Strontium hexaferrite

1.2.2 Synthesis techniques for the ferrites

A large portion of MNP-based research papers published in recent decades has focused on effective methods for preparing MNPs that are stable, shape-controlling, size-controlled and homogeneous-precipitation, microemulsion, thermal decomposition, solvothermal, sonochemical, microwave assisted, chemical vapors deposition, combustion synthesis, carbon arc, laser pyrolysis synthesis" are some of the proven and approved methods for MNPs synthesis that have been identified so far.

In this segment, we'll go through some of the most common MNP preparation methods. Each approach has its own set of benefits and drawbacks. The choice of synthesis methods is also influenced by the final application area. As a result, basic parameters such as "desired particle or cluster size, shape, crystal structure, surface chemistry, reactivity, tolerance to working temperature after preparation, pH stability, and dispersion capability, possibility of collection after participating in catalysis, whether to be used in powder form or thin film form, and so on" influence the synthesis process chosen. Figure 1.7. depicts various synthesis processes for the creation of magnetic NPs.

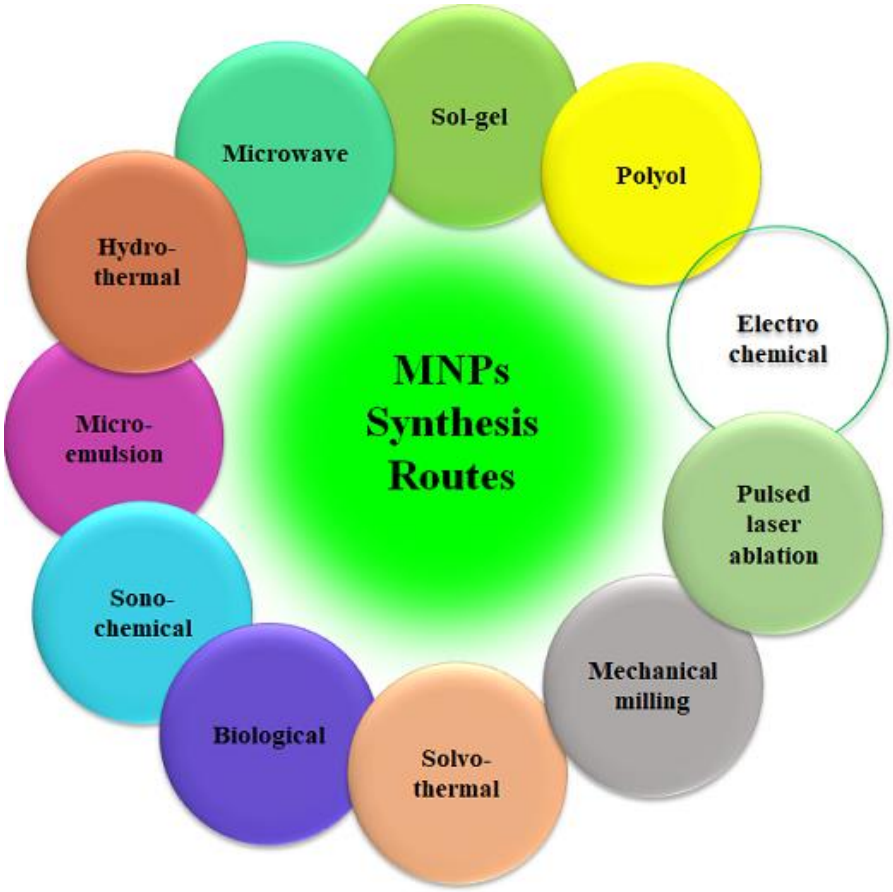

Figure 1.7: Synthesis techniques for the magnetic nanoparticles

1.2.2.1 Co- precipitation Route

"Co-precipitation route" is the maximum consistent and oldest method for MNPs creation [76]. For example, iron oxide nanoparticles were produced utilising the "Co-precipitate approach from a water-based solution containing Fe (II) and Fe (III) in anaerobic ambient conditions by adding a base for pH". [77]. The morphology and structure of MNPs are all determined by factors such as the reaction temperature, Fe (II): Fe (III) salt ratio, and medium pH [78]. Once the synthesis prerequisites were accomplished, the synthesis of magnetic nanoparticles became efficaciously repeatable. In both acidic and basic conditions, maghemite has extraordinary chemical stability. The use of a stabilising agent such as "polyvinyl alcohols" in a chainlike assembly indicating the quantity of adequate surfactant for stability has recently been disclosed, with the usage of magnetic NPs with monodispersed and changeable dimensions. [79]. The "co-precipitation route" is the widely applicable synthesis route for achieving iron oxide NPs.

1.2.2.2 Hydrothermal Method

“Using temperatures of 125°C to 250°C and pressures of 0.3 to 4 MPa, powdery iron oxide-based NPs with a crystallite size of approx. 40 nm were produced via a hydrothermal approach with a saturation magnetization of 90 emu/ g” [66]. The stoichiometry of the salts has an impact on the particle size dispersal and crystallite size of NPs [80]. Disadvantage of the “hydrothermal route” is the slow reaction kinetics at a particular temperature; however, this disadvantage is overawed by using microwaves. “Microwave-assisted synthesis” improves crystallization kinetics.

1.2.2.3 Micro-emulsion Method

“A microemulsion is a thermodynamically stable and isotropic dispersion made by combining two immiscible solvents with a layer of surfactant molecules at the interface” [81]. Surfactants usually have "hydrophilic heads" and "hydrophobic tails" that are oil soluble, resulting in interface monolayer [82]. As opposed to synthesis methods, there are many benefits to using the microemulsion technique. For example, requirement of simple equipment, nanomaterials are achieved in great form and composition, size control, desired crystal structure, can be produced. Micro-droplets of water up to 50 nm in size, are disseminated in a continuous hydrocarbon phase to form water-in-oil micro-emulsions [83]. When two identical “water-in-oil” micro-emulsions containing the necessary reagents were mixed, micro-droplets were created, which would collide, combine, and split repeatedly, resulting in the formation of precipitate within the micelles. Following the reaction's completion, ethyl-alcohol, acetone, or other solvents are added to absorb the precipitate by centrifugation or filtration. Mixed metal-iron oxide NPs are materials used for a variety of applications, especially for electronic applications [84]. Micro-emulsions are referred to as "nano-reactors" because they produce nanoparticles. The microemulsion method is used to make a wide variety of magnetic nanomaterials with reasonable size and shape control [85-86].

1.2.2.4 Sono-chemical Method

The “ultrasound field” for the controlled size distribution is used in the synthesis [87-88]. “Sono-chemical method” uses "acoustic cavitation phenomenon" and is intended for preparations where bubbles in solution are continuously developing, expanding, and collapsing. The ampule containing the solution-blend is mounted in an ultrasound reactor “at pressure (>20 MPa), temperature range (>5000 K), and cooling rate of (1010 Ks^{-1})”, and NPs are produced by the coalescence of formed bubbles, which is accompanied by micro-jets and shock waves moving at 400 km/h [89]. The "nuclear development" and "secondary

nucleation" can be halted by these tendencies. In comparison to other approaches, the sono-chemical technique has been shown to be more efficient, convenient, rational, and environmentally friendly [90]. As a result, the “sono-chemical route” may be a viable synthesis procedure for improving the magnetic response of MNPs while also facilitating better particle size distribution control.

1.2.2.5 Sol-gel Method

“Sol-gel method” is an effective aqueous path for the NPs preparations. The method is based on the “hydroxylation and condensation” which results in the creation of a “sol”. To make the solution, the nitrate or chlorides were first mixed in water. The resulting “sol" is then ‘‘gelled" by extracting the water, resulting in a viscid gel. The structure formed during the “sol-gel” process has a significant impact on gel properties. The formation of a colloidal gel is influenced by basic catalysis, while the polymeric shape of the gel is influenced by acidic catalysis. The entire sol-gel reaction takes place at ambient conditions; however, annealing is required for the better achievement of the final crystalline state. In the “sol-gel” phase, salt ratio, pH, synthesis temperature, are of the parameters that have a direct impact on reaction kinetics, reaction growth, and the properties of the gel produced [91-92]. The advantages of the “sol-gel” method include that based on the experimental conditions chosen, are (i) the high likelihood of obtaining pure crystalline or amorphous phases, and (ii) the controlled quality of the reaction products. “Sol-gel” synthesis is essentially a synthesis technique carried out at low-temperature range, which is one of the method's main features and advantages. The process is biocompatible due to the low synthesis temperature. As a result, the “sol-gel” process is a the widely used scheme for preparing nanoparticles that are then biologically processed. Only issue with the process is that it produces 3-D networks, which means in the process it is difficult to form isolated, disengaged nano-sized units [93].

1.2.2.6 Biological Method

The rise of green chemistry has established the consideration of nanotechnology around the globe [94]. The key goal of the biological strategy is to use chemical manipulations to either remove or minimize hazardous materials [95]. Biological synthesis, which involves the formation of metallic nanomaterials from plant extracts, is currently being investigated as a high-priority and exciting research field. The biological way to make MNPs is the least poisonous and harmless way to make environmentally friendly and reliable nanomaterials with an extensive array of biological applications. Figure 1.8. shows some of the applications of MNPs in nano medicines.

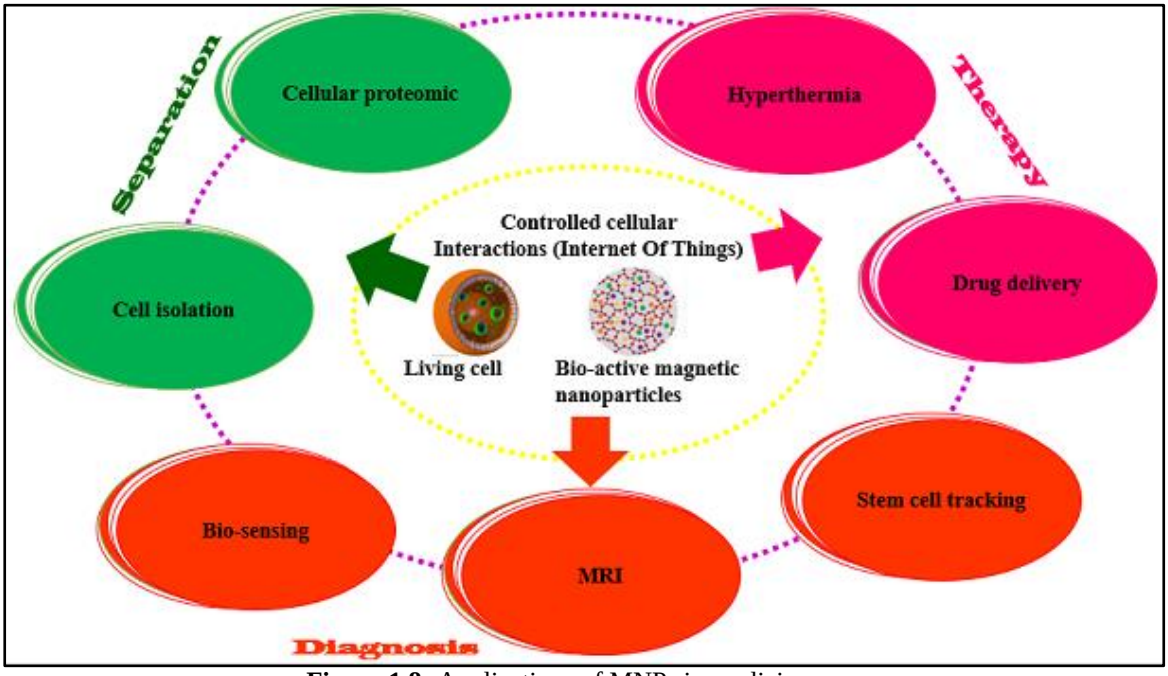

Figure 1.8: Applications of MNPs in medicine

1.3 Quantum Dots

QDs are nanometre-sized luminous semiconducting crystals with remarkable physical and chemical properties due to their small size and compact structure. QDs have different electronic and optical features. QDs are made up of elements from the periodic table's groups "III–V, II–VI, or IV–VI, such as CdS, CdSe, CdTe, CdS@ZnS, CdSe@ZnS, and CdSeTe@ZnS". These QDs are commonly used in biosensing applications due to their excellent fluorescence properties. A nanostructure is classified as (1) 2-D, such as quantum wells, (2) 1-D, such as quantum wires, or (3) 0-D, such as dots [96-99]. "QDs are 0-D relative to the bulk, and the limited number of electrons results in discrete quantized energies in the density of states (DOS) for non-aggregated 0-D structures. The staircase's step size is proportional to the reciprocal of the QDs' radius" [100-101].

1.3.1 Fluorescent Quantum Dots (Group II-VI)

The bulk level of a material has physical properties that are independent of its size. However, at the nanoscale, the idea is completely different. If the size of nanomaterials approaches the nanoscale, properties such as optical properties change. QDs emits in the range of visible to near-infrared. The emission of detectable QDs under excitation is visible to the naked eye.

The size of the QDs, as well as the substance, determines the emission profile of the QDs. Small sized QDs emit near the blue side of the spectrum, while large sized QDs emit near the red side. "Visible II-VI group QDs such as CdSe and CdSe/ZnS QDs have been recognised in multipurpose photonic applications such as optical fibre amplifiers, solar cells, and LEDs due to their bright and remarkable emission patterns". These visible QDs have also been used in medical and biological research as optical temperature probes [102].

1.3.2 Synthesis methods for Quantum Dots

1.3.2.1 Top-Down Synthesis Processes

"Electron beam lithography", "reactive-ion etching", and "wet chemical etching" are widely used to attain QDs with dimension of less than 30 nm. For orderly experimentations on the "quantum confinement effect", laser beams or directed ion have been used to make 0-D dot arrays. Etching, which has been around for over 20 years, is crucial in these nanofabrication progressions. This etching method is identified as reactive ion etching when the active species are ions (RIE). Selective etching of the substrate is accomplished via masking pattern. RIE with a mixture of BCl_3 and Ar are used to fabricate GaAs/AlGaAs in the range of approx. 40 nm [103-104]. Figure 1.9. Gives the flow chart for the various synthesis approaches and techniques for the Quantum dots (QDs).

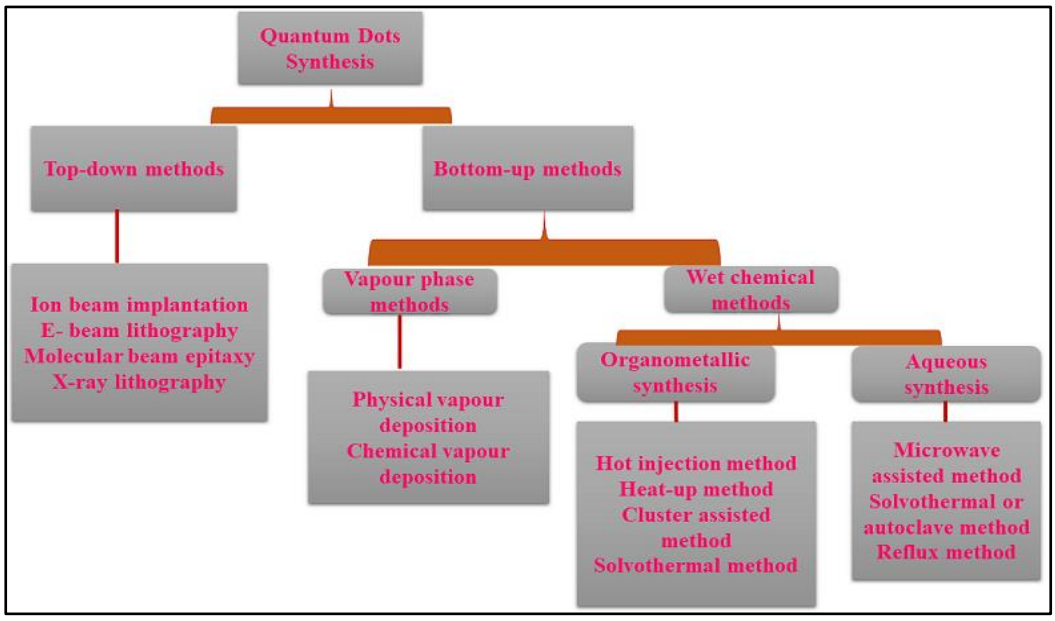

Figure 1.9: Synthesis approaches and techniques for the Quantum dots (QDs)

QDs can also be manufactured with exceptionally high lateral precision using "focused ion beam (FIB) techniques". To crackle the semiconductor substrate surface, highly

concentrated rays from a heated metal source can be implemented in a straight line. The size, shape, and the QDs inter-particle distance are all dependent on the magnitude of the ion beam [105]. Ion beam nanofabrication can create “scanning ion beam images” (similar to “scanning electron microscope” micrographs) with high resolution at predetermined locations [105]. However, this is a time-consuming, low-throughput process that uses costly equipment and results in surface damage. “Electron beam lithography”, accompanied by etching or lift-off methods, is another way to create patterns with QDs measurements. This method allows for a great deal of versatility in the development of nanostructured structures. This technique can be used to create any form of QDs, wires, or rings with precise separation and periodicity. This method was used to make “III-V” and “II-VI” QDs with dimension as minor as 30 nm with great success.

1.3.2.2 Bottom-up Approach

The QDs were synthesized using a variety of self-assembly techniques, which can be widely divided into “wet-chemical” and “vapor-phase approaches”. (1) “Wet-chemical” approaches include “microemulsion”, “sol-gel”, competitive reaction chemistry, “hot-solution decomposition”, and “electrochemistry”. (2) "Molecular beam epitaxy (MBE)", "sputtering", “liquid metal ion sources”, and “aggregation of gaseous monomers” are examples of "vapor-phase processes."

1.3.2.2.1 Wet-Chemical Methods

“Wet-chemical methods” are based on traditional precipitation methods, with parameters carefully controlled for an only solution or a mixture of solutions. Both nucleation and restricted growth of nanoparticles are inevitably involved in the precipitation method. Homogeneous, heterogeneous, and secondary nucleation are the three forms of nucleation. Temperature, stabilisers or micelle formation, precursor concentrations, anionic to cationic species ratios, and solvent can all be used to make QDs of the chosen morphology. The following sections go into some of the most popular synthesis methods.

1.3.2.2.2 Sol-Gel Process

For several years, “sol-gel techniques” have been used to make NPs, counting QDs [106-108]. “Hydrolysis, condensation (sol formation), and growth” are the prime stages in the method. In a nutshell, the metal precursor hydrolysis and condenses in the medium to form a “sol”, which is then polymerized to form a network (gel). CdS, ZnO [109], and PbS [106] are examples of

QDs synthesized using this process. The procedure is straightforward, cost-effective, and scalable. The key drawbacks of the sol-gel method are its wide size distribution and high defect concentration [110].

1.3.2.2.3 Microemulsion Process

At room temperature, "microemulsion processes" are widely used to synthesize QDs. Typical "microemulsions, i.e., oil-in-water, and reverse microemulsions, i.e., water-in-oil", are the two types of microemulsions. For the production of QDs, the reverse micelle process is used, in which two immiscible liquids are combined and stirred to create an emulsion. "The size of the micelle, which is regulated by the molar ratio of water and surfactant, limits the growth of the resulting QDs (W)" [111]. "II-VI core and core/shell QDs, such as CdS CdS:Mn/ZnS [108-109], ZnS/CdSe, CdSe/ZnSe [111], ZnSe, and IV-VI QDs, have been prepared using the reverse micelle technique". This method has many advantages, including simple regulation of QDs dimension by adjusting the ratio of water to surfactant, better size dispersal as that of "sol gel process", and ease of QDs dispersion. Low yield and the inclusion of impurities and defects are some of the drawbacks.

1.3.2.2.4 "Hot-Solution Decomposition Process"

"Hot-Solution Decomposition Process" is a well-known approach for the creation of QDs, which was initially explored in detail by Bawendi and colleagues in 1993. [112]. Precursors from Group II elements, "such as alkyl [113], acetate [114], carbonate [115], and oxides, are combined with phosphene or bis(trimethyl-silyl) precursors from Group VI. In a dry box, a mixture of Cd-precursor and tri-n-octyl-phosphine (TOP) selenide is prepared and injected into the flask at a temperature of 300 °C with intense stirring. The injection of precursors into the flask at the same time as TOPO results in homogeneous nucleation of QDs, with relatively slow growth of QDs by 'Ostwald ripening.'" Smaller QDs lose mass to larger QDs during Ostwald ripening due to their higher free energy, gradually disappearing. At 230–250 °C, the net effect is a steady increase in the size of QDs. The reaction time and temperature are primarily responsible for the final size of the QDs. During the first few hours, aliquots from the flask can be withdrawn at regular intervals and the optical absorption edge can be used to achieve a desired particle size. II-VI [116-120], IV-VI [121], and III-V QDs [122] have all been synthesized using this process.

1.4 Core-shell nanostructures

CSNs are emerging as a unique class of nano structures owing to specific benefits such as ease of surface functionalization and modification accordingly. CSNs come in a variety of forms, together with silica-based, metallic, up conversion, magnetic, and carbon-based core-shell structures among others. The current study looks at expansions and advances of core-shell systems, as “newly generated properties, the effect of parameter control, surface modifications, functionalization, and last but not least, promising applications in the fields of drug delivery and tissue engineering”, all while keeping reach, demand, and challenges in mind. This work also paves the way for important future research into multi-core and shell-based functional nano-systems.

1.5 Core-Shell multifunctional nanostructures

Various types of core-shell multifunctional nanostructures have been produced for a number of purposes. We created a core-shell nanostructure that is similar to a "magnet in semiconductor." The magnetic core is encased in a shell of non-magnetic semiconductors. Different types of multifunctional core-shell nanostructures have been created. Since the field of magneto-fluorescent nanocomposites is in its early stages, classification of these materials is complicated and subjective. Core-shell nanostructures make up the majority of these nanocomposites. We can distinguish different types of magneto-fluorescent nanocomposites in general.:

1. A magnetic core encased in a silica shell with fluorescent components;
2. MNPs coated with fluorescently labelled polymer;
3. MNPs coated with fluorescent bilipid;
4. A fluorescent entity bound covalently to magnetic core through a spacer;
5. Magnetic/semiconductor core-shell system;
6. QDs; doped with magnetic material.

1.5.1 Fluorophore Encapsulated MNPs with Silica-coating

There are numerous advantages to using silica as a covering for MNPs in the creation of “magneto-fluorescent nanocomposites”. The silica coating prevents any fluorophores from being quenched by the magnetic cores. The silica surface can be chemically functionalized, allowing different fluorescent and biological organisms to bind to the exterior. It also aids in particle aggregation prevention and increases solution steadiness. “Since magnetite's isoelectric point is at pH 7, it's important to coat the particles more to keep them stable in the pH range6–10. The application of a thin layer of silica lowers the isoelectric point to about pH 3, improving steadiness near to neutral pH” [123]. Finally, since there is no chance of

desorption of the tightly covalently bound silica shells, silica coating has a major advantage over conventional surfactant coatings. A number of studies have been published that use a silica-coating method to create fluorescent-magnetic nanocomposites.

1.5.2 Polymer-coated Magnetic Cores Treated with Luminescent Units

Polymers or polyelectrolytes (PE)-based self-assembly techniques have recently grabbed much consideration. The process has many benefits, including the ability to adjust the thickness of the polymer coating and the ability to deposit a single layer of charged particles. researchers used this method to prepare magnetic-fluorescent nanocomposites by manipulating the interactions of PE with the "-vely charged" surface of MNPs, followed by CdTe QDs addition of Zeta potential measurements, which show how the surface charge changes when treated with an oppositely charged species, confirmed the existence of the polyelectrolyte.

1.5.3 Fluorescently Labelled Lipid-coated Magnetic Nanoparticles

Nanoparticles are commonly coated with lipid layers to enhance their stability and biocompatibility. This method involves coating the surface of nanoparticles with amphiphilic lipid molecules, which can then be connected to a variety of organisms. There have been many studies on the use of this method to create magneto-fluorescent nanocomposites. In some research work, biotin was conjugated to MNPs coated with an oleate bilipid layer in order to bind streptavidin-fluorescein isothiocyanate [124]. Zhang and co-workers [125] used a similar method to create a sandwich-type immunoassay by using a Schiff base reaction to functionalize dextran-coated MNPs with CdTe QD [126].

1.5.4 Magnetic Core Directly Linked to Fluorescent Entity via a Molecular Spacer

To avoid quenching by the paramagnetic core, directly connecting luminous moiety to a magnetic core necessitates the use of a sufficiently long molecular linker. The most popular approach is to use MNPs capped with a stabilizing agent that includes many functional groups that can be further functionalized. This process produced new nanocomposites that could be used in more biological research [127]. "Cheon and colleagues [128] developed a monodisperse organic-stable suspension of 9 nm Fe_3O_4 nanoparticles, which they phase transferred into aqueous solution using 2,3-DMSA. used ultrasonic effects to create a covalent bond between the nickel oxide surface and the carboxylic acid groups of a porphyrin molecule, resulting in porphyrin-coated magnetic nickel nanowires". The main goal of this research was to create organized nanowire arrays with increased anisotropy [129-130].

1.5.5 Magnet in semiconductor type core-shell nanostructures

The magnetic core is surrounded by a non-magnetic layer, resulting in a new class of core-shell multifunctional nanostructures. Example of such type are the $NiZnFe_2O_4$/CdS and $SrFe_{12}O_{19}$/CdS where $NiZnFe_2O_4$ and $SrFe_{12}O_{19}$ form the magnetic core, while CdS QDs form the shell.

1.6 Core-Shell nanostructures synthesis methods

The commonly used method for the core-shell synthesis is the solution growth methods, with two steps: in the first step, core structure is synthesized and secondly the coating of core material with shell content is achieved. “Chemical vapour deposition (CVD)” or “pulsed laser deposition (PLD)” are two popular gas-phase synthesis techniques [131-132].

These techniques, require several steps, with the shell material typically being deposited onto an already established core substrates [133-135]. The core-shell processing has been examined for these well-established techniques, and the various parameters that influence particle formation have been identified. Some of the authors recently used electron beam evaporation to create core-shell nanostructures in a novel way [136-137]. The core-shell particles by the mean of gas phase technique are synthesized in single step without the use of substrates in the process. As a result, this process could be a more cost-effective way to make core–shell nanostructures. Previous nano powders made with this method were developed at rates of kg/h [138-140]. The reaction cannot be observed in real time since the “electron beam evaporation process” is a “high-energy” method. As a result, the resulting particles are thoroughly characterized in order to shed light on how they came to be. Future researchers who want to use the electron beam evaporation method to make new forms of core–shell particles will benefit from this work.

“Wet chemical approach” is alternative convenient procedure for the core-shell synthesis. CSNs are synthesized using polar and nonpolar solvents in this process. It's a form of traditional precipitation method that involves nucleation and growth stages. By adjusting synthesis constraints such as pH, and temperature, nanostructures of the desired form, composition, and size can be developed. Homogeneous nucleation, heterogeneous nucleation, and secondary nucleation are all possible classifications for nucleation.

1.7 Applications of magneto-fluorescent core-shell nanostructures

Magneto-fluorescent composites in biomedical applications have three interesting properties: super paramagnetism, fluorescence, their capability to be targeted which make these

nanostructures exciting biomedical research tools. Their applications to identification and isolation, cancer diagnosis and treatment, fluorescent and MR imaging will be addressed in the following pages.

1.7.1 Detection and separation of biomolecules

"Through high-affinity contacts between an antibody and an antigen or a ligand and a receptor, targeting ligands attached to magneto-fluorescent nanocomposites generate target-functional nanocomposites capable of identifying and sorting target molecules from complex mixtures". [141-145]. High sensitivity and accuracy, time savings, wide range, and ease of procedure are all advantages of this method.

1.7.2 Fluorescent and MR imaging

Magnetic resonance and fluorescent imaging are non-invasive approaches having substantial impact on disease detection in past years. "MRI provides excellent imaging in vivo and in vitro" [146]. Magneto-fluorescent NPs can be used as multimodal contrast agents in both fluorescent and MR imaging, providing extra delicate imaging at the molecular and cellular levels [147]. "Furthermore, after being modified by the addition of a targeting ligand, multifunctional NPs may be used to target particular tissues or cells in order to improve the effects of tomography agents" [148]. Figure 1.10 shows some of the imaging modalities of CSNs used for biomedical fields.

1.7.3 Diagnosis of cancer and its treatment

Cancer is a fatal illness that usually has little to no symptoms until it is advanced to a late stage. Early diagnosis and prompt care are the best ways for patients to increase their survival rates. "Magneto-fluorescent composite NPs have been used to target cells in recent years. This is normally performed by conjugating them with a targeted ligand, such as a monoclonal antibody specific to the target" [149]. These NPs should have both magnetic and luminescent properties. These molecules aid in the detection and treatment of cancer. In addition, targeted NPs that delivers anticancer medications to cancer cells selectively will have less adverse effects than chemotherapy.

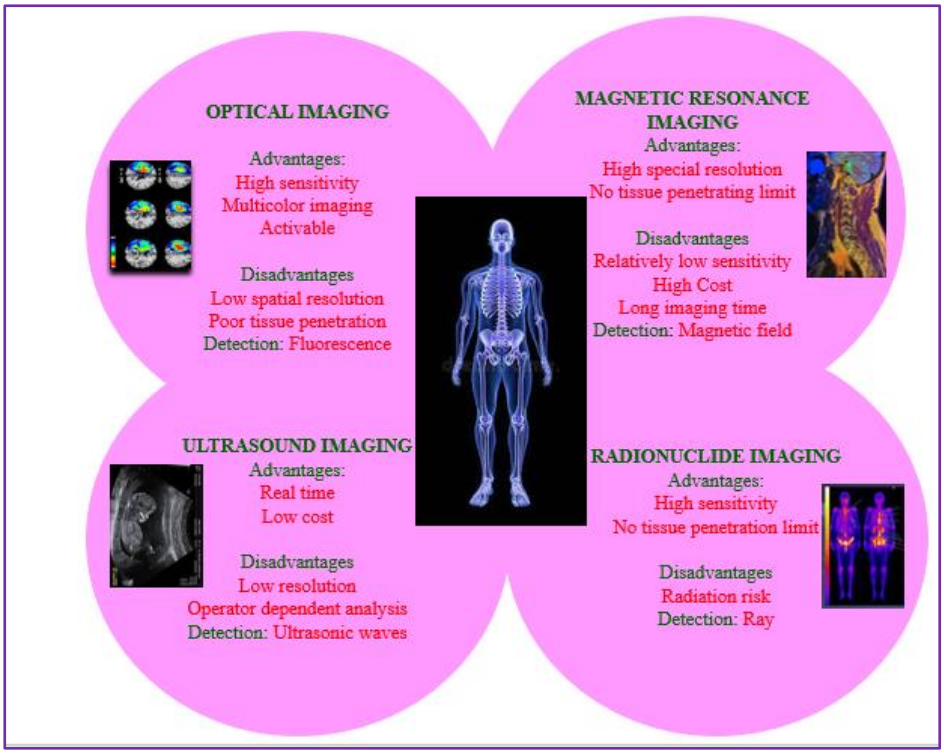

Figure 1.10: Main imaging modalities of CSNs used for biomedical fields

Table 1.1: Different reports on applications of Ferrites, CdS QDs and their CSNs in diverse fields are listed in table

	Applications	Research Group	References
$NiZnFe_2O_4$	Hyperthermia and drug targeting	Park JI et al	10.1021/ja0156340
	Nuclear magnetic resonance [NMR] imaging	Liu C et al	10.1021/cm0403457
	Drug delivery	Casula et al	10.1021/ja056139x
	Bio separation	Vestal CR et al	10.1021/nl034816k
	Magneto Relaxometry	Murthy N et al	10.1016/S0168-3659
$SrFe_{12}O_{19}$	Permanent memory devices	Vicky V. Mody et al	10.1515/ejnm-2012-0008/
	Magnetic separation	Akira Ito et al	10.1263/jbb.100.1
CdS QDs	Quantum Dot Sensitized Solar Cell	Vogel R et al	https://www.ncbi.nlm.nih.gov /pmc/articles/PMC5445848/
	Quantum Dot Dispersed Solar Cell	Wang Y et al	doi: 10.1016/0009-2614(92)87047-S
	Fluorescence for Bioimaging	Michalet X et al	10.1126/science.1104274
	Multimodal imaging capabilities	Santra S et al	10.1002/adma.200500018
$NiZnFe_2O_4$/CdS	Controlled Drug Delivery and Specific Targeting	Rajib Ghosh Chaudhuri et al	10.1021/cr100449
$SrFe_{12}O_{19}$/CdS	Cell sorting	Veronica Iacovacci et al	10.5772/62865

1.8 Motivation behind the work

Requirement of aqueous mediated synthesis of stable magneto-fluorescent nanostructures for multimodal biomedical applications.

1.9 Objectives of the thesis

Objective 1: "Synthesis and characterization of nickel zinc ferrite ($NiZnFe_2O_4$), cadmium sulphide (CdS) QDs and their core-shell nanostructures for drug delivery applications".

Objective 2: "Synthesis and characterization of strontium hexaferrite ($SrFe_{12}O_{19}$), cadmium sulphide (CdS) QDs and their core-shell nanostructures for magnetic cell sorting applications".

Objective 3: Comparison of hard-soft ferrite-based core/shell nanostructures based on structural, morphological, optical, magnetic and functional analysis.

Several characterization tools and techniques have been used to know the properties and discussed in the next chapter. Subsequently in coming chapters each and every objective will be presented and discussed in thoroughly.

1.10 Outline of thesis

Chapter 1. General introduction of multifunctional nanostructure is described. Different type of core-shell with their applications in various field are discussed briefly.

Chapter 2. Experimental techniques used for core-shell preparation of nanostructures with the core of hard ferrite and with the core of soft ferrite annealed at different temperature are described. This section also includes the characterization techniques that are used to know the structural, morphological, optical and the magnetic properties of the core-shell system.

Chapter 3. This chapter describes the synthesis of soft ferrite-based (NZF) core-shell nanostructure with CdS QDs shell synthesized by "*sol-gel"* method with the NZF annealed at two different temperatures. This chapter also include measurement of morphological, structural, optical, elemental, and magnetic properties which has been done by XRD, FESEM, EDX, TEM, UV, PL and VSM studies. The interface effect of magnetic core and the non-magnetic shell is also discussed.

Chapter 4. This chapter describes the synthesis of hard ferrite-based (SHF) core-shell nanostructure with CdS QDs shell synthesized by "*sol-gel"* method with the SHF annealed at two different temperatures. This chapter also include measurement of morphological,

elemental, optical, structural, and magnetic properties which has been done by XRD, FESEM, EDX, TEM, UV, PL and VSM studies. The interface effect of magnetic core and the non-magnetic shell is also discussed.

Chapter 5. This chapter includes the comparison of the best results obtained by the CSNs formed with the hard ferrite and the soft ferrite- based core-shell nanostructures. The structural, morphological, elemental, optical and the magnetic properties of prepared samples have been measured from XRD, FESEM, EDX, UV, PL and VSM techniques respectively. The comparison of properties based on the difference in core material is also included in this chapter.

Chapter 6. This chapter deals with the overall summery and conclusion of the work.

1.11 REFERENCES

[1] Burda C., Chen X., Narayanan R., & El-Sayed, M. A., "Chemistry and properties of nanocrystals of different shapes". Chemical reviews, vol105(4), pp. 1025-1102, Apr. 2005.

[2] Kamat, P. V. Photophysical., "photochemical and photocatalytic aspects of metal nanoparticles". The Journal of Physical Chemistry B, vol 106(32), pp. 7729-7744, Aug. 2002.

[3] Frederix, F., Friedt, J. M., Choi, K. H., Laureyn, W., Campitelli, A., Mondelaers, D., & Borghs, G. "Biosensing based on light absorption of nanoscaled gold and silver particles". Analytical chemistry, vol 75(24), pp. 6894-6900, Dec. 2003.

[4] Praharaj, S., Nath, S., Ghosh, S. K., Kundu, S., & Pal, T., "Immobilization and recovery of Au nanoparticles from anion exchange resin: resin-bound nanoparticle matrix as a catalyst for the reduction of 4-nitrophenol". Langmuir, vol 20(23), pp. 9889-9892, Nov. 2004.

[5] Campbell, C. T., Parker, S. C., & Starr, D. E., "The effect of size-dependent nanoparticle energetics on catalyst sintering". Science, vol. 298(5594), pp. 811-814, Oct. 2002.

[6] T. A. Skotheim, Handbook of Conducting Polymers, vol. 1, 1986.

[7] Kumar, K. S., Kumar, V. B., & Paik, P., "Recent advancement in functional core-shell nanoparticles of polymers: synthesis, physical properties, and applications in medical biotechnology". Journal of Nanoparticles, 2013.

[8] Andersson, P., Forchheimer, R., Tehrani, P., & Berggren, M., "Printable all-organic electrochromic active-matrix displays". Advanced Functional Materials, vol. 17(16), pp. 3074-3082, Nov. 2007.

[9] Liu, Y., & Cui, T., "Polymeric integrated AC follower circuit with a JFET as an active device". Solid-state electronics, vol 49(3), pp. 445-448, Mar. 2005.

[10] Lee, S. K., Cho, J. M., Goo, Y., Shin, W. S., Lee, J. C., Lee, W. H., ... & Moon, S. J., "Synthesis and characterization of a thiazolo [5, 4-d] thiazole-based copolymer for high performance polymer solar cells". Chemical Communications, vol 47(6), pp. 1791-1793, 2011.

[11] Chua, L. L., Zaumseil, J., Chang, J. F., Ou, E. C. W., Ho, P. K. H., Sirringhaus, H., & Friend, R. H. (2005). General observation of n-type field-effect behaviour in organic semiconductors. Nature, 434(7030), 194-199.

[12] Tsao, H. N., Cho, D., Andreasen, J. W., Rouhanipour, A., Breiby, D. W., Pisula, W., & Müllen, K.., "The influence of morphology on high-performance polymer field-effect transistors". Advanced Materials, vol 21(2), pp. 209-212, Jan. 2009.

[13] Daniel, M. C., & Astruc., "Gold nanoparticles: assembly, supramolecular chemistry, quantum-size-related properties, and applications toward biology, catalysis, and nanotechnology". Chemical reviews, vol 104(1), pp. 293-346, Jan. 2004.

[14] Gawande, M. B., Bonifácio, V. D., Varma, R. S., Nogueira, I. D., Bundaleski, N., Ghumman, C. A. A., ... & Branco, P. S., "Magnetically recyclable magnetite–ceria (Nanocat-Fe-Ce) nanocatalyst–applications in multicomponent reactions under benign conditions". Green chemistry, vol. 15(5), pp. 1226-1231, 2013.

[15] Gawande, M. B., Branco, P. S., & Varma, R. S., "Nano-magnetite (Fe 3 O 4) as a support for recyclable catalysts in the development of sustainable methodologies". Chemical Society Reviews, vol 42(8), pp. 3371-3393, 2013.

[16] Lu, A. H., Salabas, E. E., & Schüth, F., Magnetic nanoparticles: synthesis, protection, functionalization, and application. Angewandte Chemie International Edition, vol. 46(8), pp.1222-1244, Feb. 2007.

[17] Geim, A. K., & Novoselov, K. S., "The rise of graphene". In Nanoscience and technology: a collection of reviews from nature journals, pp. 11-19, 2010.

[18] Georgakilas, V., Bourlinos, A. B., Zboril, R., Steriotis, T. A., Dallas, P., Stubos, A. K., & Trapalis, C., "Organic functionalisation of graphenes". Chemical Communications, vol. 46(10), pp. 1766-1768, 2010.

[19] Georgakilas, V., Otyepka, M., Bourlinos, A. B., Chandra, V., Kim, N., Kemp, K. C., ... & Kim, K. S., "Functionalization of graphene: covalent and non-covalent approaches, derivatives and applications". Chemical reviews, vol. 112(11), pp. 6156-6214, Nov. 2012.

[20] Pykal, M., Šafářová, K., Machalová Šišková, K., Jurečka, P., Bourlinos, A. B., Zbořil, R., & Otyepka, M., "Lipid enhanced exfoliation for production of graphene nanosheets". The Journal of Physical Chemistry C, vol. 117(22), pp. 11800-11803. Jun 2013.

[21] Zbořil, R., Karlický, F., Bourlinos, A. B., Steriotis, T. A., Stubos, A. K., Georgakilas, V., ... & Otyepka, M., "Graphene fluoride: a stable stoichiometric graphene derivative and its chemical conversion to graphene." Small, vol. 6(24), pp. 2885-2891, Dec. 2010.

[22] Zeng, H. C., "Integrated nanocatalysts". Accounts of chemical research, vol. 46(2), pp. 226-235. Feb. 2013.

[23] Bell, A. T., "The impact of nanoscience on heterogeneous catalysis". Science, vol. 299(5613), pp. 1688-1691, Mar. 2003.

[24] Wittstock, A., Zielasek, V., Biener, J., Friend, C. M., & Bäumer, M., "Nanoporous gold catalysts for selective gas-phase oxidative coupling of methanol at low temperature". Science, vol. 327(5963), pp. 319-322, Jan. 2010.

[25] Pecher, J., & Mecking, S., "Nanoparticles of conjugated polymers". Chemical reviews, vol. 110(10), pp. 6260-6279, Oct. 2010.

[26] Silva, R., & Asefa, T., "Noble Metal-Free Oxidative Electrocatalysts: Polyaniline and Co (II)-Polyaniline Nanostructures Hosted in Nanoporous Silica". Advanced Materials, vol. 24(14), pp. 1878-1883, Apr. 2012.

[27] Baruwati, B., Polshettiwar, V., & Varma, R. S., "Glutathione promoted expeditious green synthesis of silver nanoparticles in water using microwaves". Green chemistry, vol. 11(7), pp. 926-930, 2009.

[28] Baruwati, B., & Varma, R. "High value products from waste: grape pomace extract-a three-in-one package for the synthesis of metal nanoparticles". ChemSusChem, vol. 2(11), pp. 1041-1044, Jan. 2009.

[29] Zoppellaro, G., Tuček, J., Herchel, R., Šafářová, K., & Zbořil, R., "Fe3O4 nanocrystals tune the magnetic regime of the Fe/Ni molecular magnet: a new class of magnetic superstructures". Inorganic chemistry, vol. 52(14), pp. 8144-8150, Jul. 2013.

[30] Hu, M., Furukawa, S., Ohtani, R., Sukegawa, H., Nemoto, Y., Reboul, J., ... & Yamauchi, Y., "Synthesis of Prussian blue nanoparticles with a hollow interior by controlled chemical etching". Angewandte Chemie International Edition, vol. 51(4), pp. 984-988, Jan. 2012.

[31] Gawande, M. B., Shelke, S. N., Zboril, R., & Varma, R. S., "Microwave-assisted chemistry: synthetic applications for rapid assembly of nanomaterials and organics". Accounts of chemical research, 47(4), pp. 1338-1348, Apr. 2014.

[32] Burda, C., Chen, X., Narayanan, R., & El-Sayed, M. A., "Chemistry and properties of nanocrystals of different shapes". Chemical reviews, vol. 105(4), pp. 1025-1102, Apr. 2005.

[33] Duncan, C. T., Biradar, A. V., Rangan, S., Mishler, R. E., & Asefa, T., Trimming nanostructured walls while fluorinating their surfaces: A route to making and widening pores of nanoporous materials and efficient catalysts. Chemistry of Materials, 22(17), 4950-4963, Sep. 2010.

[34] Zaera, F., "Nanostructured materials for applications in heterogeneous catalysis". Chemical Society Reviews, vol. 42(7), pp. 2746-2762, 2013.

[35] Park, J. C., Kim, A. Y., Kim, J. Y., Park, S., Park, K. H., & Song, H., "ZnO–CuO core–branch nanocatalysts for ultrasound-assisted azide–alkyne cycloaddition reactions". Chemical Communications, vol. 48(68), pp. 8484-8486, 2012.

[36] Baruah, J. M., & Narayan, J., "Dilute magnetic semiconducting quantum dots: Smart materials for spintronics". Nonmagn. Magn. Quantum Dots, pp. 87-199 Apr. 2018.

[37] Gibson RF. A review of recent research on mechanics of multifunctional composite materials and structures. Compos Struct, vol. 92(12), pp. 2793–2810, Nov.2010

[38] Suh WH, Suh YH, Stucky GD. Multifunctional nano systems at the interface of physical and life sciences. Nano Today, vol. (41), pp. 27–36, Feb. 2009.

[39] Bigall NC, Parak WJ, Dorfs D. Fluorescent, magnetic and plasmonic-Hybrid multifunctional colloidal nano objects. Nano Today, vol.7(4), pp. 282–296, Aug. 2012.

[40] Lee JE, Lee N, Kim T, Kim J, Hyeon T. Multifunctional mesoporous silica nanocomposite nanoparticles for theragnostic applications. Accounts Chem Res. Vol. 44(10), pp. 893–902, Oct. 2011.

[41] Liu, X., & Hersam, M. C. Interface characterization and control of 2D materials and heterostructures. Advanced Materials, vol. 30(39), pp. 1801586. Sep. 2018.

[42] Wang, S. G., Han, G., Yu, G. H., Jiang, Y., Wang, C., Kohn, A., & Ward, R. C. C. (2007). Evidence for FeO formation at the Fe/MgO interface in epitaxial TMR structure by X-ray photoelectron spectroscopy. Journal of magnetism and magnetic materials, vol. 310(2), pp.1935-1936, Mar. 2007.

[43] Yuasa, S., Nagahama, T., Fukushima, A., Suzuki, Y., & Ando, K. (2004). Giant room-temperature magnetoresistance in single-crystal Fe/MgO/Fe magnetic tunnel junctions. Nature materials, vol.3(12), pp. 868-871, Dec. 2004.

[44] Yu, G. H., Chai, C. L., Zhu, F. W., Xiao, J. M., & Lai, W. Y. Interface reaction of NiO/NiFe and its influence on magnetic properties. Applied Physics Letters, vol. 78(12), 1706-1708, Mar. 2001.

[45] Jaffres, H., & Fert, A. Spin injection from a ferromagnetic metal into a semiconductor. Journal of applied physics, vol. 91(10), pp. 8111-8113. May. 2002.

[46] Issa, B., Obaidat, I. M., Albiss, B. A., & Haik, Y. Magnetic nanoparticles: surface effects and properties related to biomedicine applications. International journal of molecular sciences, vol. 14(11), pp. 21266-21305, Nov. 2013.

[47] Manhas, A., Singh, M., Hussain, M. I., Javed, Y., & Sharma, S. K. (2021). Progress in Ferrites Materials: The Past, Present, Future and Their Applications. In *Spinel Nanoferrites* (pp. 1-40). Springer, Cham.

[48] Ortiz-Quiñonez, J. L., Pal, U., & Villanueva, M. S. (2018). Structural, magnetic, and catalytic evaluation of spinel Co, Ni, and Co–Ni ferrite nanoparticles fabricated by low-temperature solution combustion process. *ACS omega*, *3*(11), 14986-15001.

[49] Smit, J., & Wijn, H. P. J. Ferrites, Philips technical library. Eindhoven, The Netherlands, vol. 278, 1959.

[50] Makovec, D., & Drofenik, M. Non-stoichiometric zinc-ferrite spinel nanoparticles. Journal of Nanoparticle Research, vol. 10(1), pp. 131-141, Dec. 2008.

[51] Makovec D., Kodre A., Gyergyek S., Arčon I., Jagodič M., Drofenik M. *Influence of synthesis method on structural and magnetic properties of cobalt ferrite nanoparticles.* J. Nanoparticle Res. Vol. 12(4), pp. 1263–1273. May. 2010.

[52] Ammar S., Jouini N., Fiévet F., Stephan O., Marhic C., Richard M., Villain F., Cartier dit Moulin C., Brice S., Sainctavit P. *Influence of the synthesis parameters on the cationic distribution of ZnFe2O4 nanoparticles obtained by forced hydrolysis in polyol medium.* J. Non. Cryst. Solids. Vol.345, *pp.* 658–662. Oct. 2004.

[53] Sato T., Haneda K., Seki M., Iijima T. *Morphology and magnetic properties of ultrafine $ZnFe_2O_4$ particles.* Appl. Phys. A. *vol.*50(1), pp. 13–16. Jan. 1990.

[54] Kamiyama T., Haneda K., Sato T., Ikeda S., Asano H. *Cation distribution in ZnFe2O4 fine particles studied by neutron powder diffraction.* Solid State Commun. Vol. 81(7) pp. 563–566. Feb. 1992.

[55] Jeyadevan B., Tohji K., Nakatsuka K. *Fine structure*. J. Appl. Phys. Vol.76, pp. 6325–6327.1994.

[56] Hamdeh H.H., Ho J.C., Oliver S.A., Willey R.J., Oliveri G., Busca G., Introduction I. Magnetic properties of partially-inverted zinc ferrite aerogel powders. *J. Appl. Phys.* vol. 81(4), pp.1851–1858. Feb. 1997.

[57] Makovec D., Kodre A., Arčon I., Drofenik M. *Structure of manganese zinc ferrite spinel nanoparticles prepared with co-precipitation in reversed microemulsions.* J. Nanoparticle Res. Vol. 11(5) pp. 1145–1158. Jul. 2009.

[58] Makovec D., Kodre A., Arčon I., Drofenik M. *The structure of compositionally constrained zinc-ferrite spinel nanoparticles*. J. Nanoparticle Res. Vol.13(4), pp.1781–1790, Apr. 2011.

[59] Bellouard, C., Mirebeau, I., & Hennion, M. *Magnetic correlations of fine ferromagnetic particles studied by small-angle neutron scattering.* Physical Review B, vol. *53*(9), 5570. Mar. 1996.

[60] Omelyanchik A, Salvador M, D'Orazio F, Mameli V, Cannas C, Fiorani D, Musinu A, Rivas M, Rodionova V, Varvaro G, Peddis D. Magnetocrystalline and surface anisotropy in cofe2o4 nanoparticles. Nanomaterials. vol10(7), pp. 1288. Jul. 2020.

[61] Del Bianco L, Hernando A, Multigner M, Prados C, Sánchez-López JC, Fernandez A, Conde CF, Conde A. Evidence of spin disorder at the surface–core interface of oxygen passivated Fe nanoparticles. Journal of applied physics. Vol. 84(4) pp. 2189-92 Aug. 1998.

[62] Gazeau F, Dubois E, Hennion M, Perzynski R, Raikher Y. Quasi-elastic neutron scattering on γ-Fe2O3 nanoparticles. EPL (Europhysics Letters). Vol. 40(5), pp. 575, Dec.1997.

[63] Hennion M, Bellouard C, Mirebeau I, Dormann JL, Nogues M. Dual spin dynamics of small fe particles. EPL (Europhysics Letters). Vol. 25(1), pp.43. 1994.

[64] Makovec, D., Košak, A., & Drofenik, M. *The preparation of MnZn-ferrite nanoparticles in water–CTAB–hexanol microemulsions*. Nanotechnology, vol. 15(4), pp. S160, Jan. 2004.

[65] Sivakumar, N., Narayanasamy, A., Shinoda, K., Chinnasamy, C. N., Jeyadevan, B., & Greneche, J. M. *Electrical and magnetic properties of chemically derived*

nanocrystalline cobalt ferrite. Journal of applied Physics, vol. *102*(1), 013916, Jul. 2007.

[66] Tirosh, E., Shemer, G., & Markovich, G. *Optimizing cobalt ferrite nanocrystal synthesis using a magneto-optical probe.* Chemistry of materials, vol. *18*(2), pp. 465-470. Jan. 2006.

[67] Li, S., John, V. T., O'Connor, C., Harris, V., & Carpenter, E. *Cobalt-ferrite nanoparticles: Structure, cation distributions, and magnetic properties.* Journal of Applied Physics, 87(9), pp. 6223-6225, May. 2000.

[68] Berkowitz, A. E., Schuele, W. J., & Flanders, P. J. *Influence of crystallite size on the magnetic properties of acicular γ-Fe2O3 particles.* Journal of Applied Physics, vol. *39*(2), pp. 1261-1263, Feb. 1968.

[69] Jacob, J., & Khadar, M. A. *Investigation of mixed spinel structure of nanostructured nickel ferrite.* Journal of applied physics, vol. 107(11), pp. 114310, Jun. 2010.

[70] Parker, G. (2001). Encyclopedia of materials: science and technology. 2001.

[69] Dahiya, M. S., Tomer, V. K., & Duhan, S. Metal–ferrite nanocomposites for targeted drug delivery. In Applications of Nanocomposite Materials in Drug Delivery. pp. 737-760, *Woodhead Publishing*, Jan. 2018.

[71] Atay, H. Y. (2016). *Innovative High-tech Ceramics Materials.* Ashutosh Tiwari, Mohammad Rabia Alenezi and Seong Chan Jun, 93. Sep. Jun. 2016.

[72] Momma, K., & Izumi, F. (2011). VESTA 3 for three-dimensional visualization of crystal, volumetric and morphology data. *Journal of applied crystallography*, *44*(6), 1272-1276.

[73] Haspers, J. M. *Ferrites: Their properties and applications.* In Modern Materials, vol. 3, pp. 259-341. Jan. 1962.

[74] Lodhia, J., Mandarano, G., Ferris, N. J., Eu, P., & Cowell, S. F. (2010). *Development and use of iron oxide nanoparticles (Part 1)*: Synthesis of iron oxide nanoparticles for MRI. Biomedical imaging and intervention journal, *vol. 6*(2), pp. e12, Jul. 2010.

[75] Rawat, D., Sethi, J., Sahani, S., Barman, P. B., & Singh, R. R. (2021). Pioneering and proficient magneto fluorescent nanostructures: Hard ferrite-based hybrid structures. *Materials Science and Engineering: B*, *265*, 115017.

[76] Surowiec, Z., Budzyński, M., Durak, K., & Czernel, G. *Synthesis and characterization of iron oxide magnetic nanoparticles*. Nukleonika, vol. *62*. 2017.

[77] Pikula, T., Dzik, J., Guzdek, P., Mitsiuk, VI., Surowiec, Z., Panek, R., Jartych, E., Magnetic properties and magnetoelectric coupling enhancement in Bi5Ti3FeO15 ceramics. Ceram. Int., vol. 43, pp. 11442-9, Oct. 2017.

[78] Gul, S., Khan, SB., Rehman, IU., Khan, MA., Khan, MI., A Comprehensive review of magnetic nanomaterials modern day theranostics. Front. Mater. Sci., vol. 6, 179, Jul. 2019.

[79] Guo, Y., Wang, Z., Shao, H., and Jiang, X. (2013). Hydrothermal synthesis of highly fluorescent carbon nanoparticles from sodium citrate and their use for the detection of mercury ions. Carbon., vol.52, pp.583-589, Feb. 2013.

[80] Kumar, R., Kumar, H., Kumar, M., Singh, R. R., & Barman, P. B. Enhanced saturation magnetization in cobalt doped Ni-Zn ferrite nanoparticles. Journal of Superconductivity and Novel Magnetism, vol. 28(12), pp. 3557-3564, Dec. 2015.

[81] Rawat, D., Kumari, A., & Singh, R. R. Synthesis and Functionalization of Magnetic and Semiconducting Nanoparticles for Catalysis. Functionalized Nanomaterials for Catalytic Application, pp. 261-302, Jun. 2021.

[82] García-Cano, I., Serrano-Maldonado, C. E., Olvera-García, M., Delgado-Arciniega, E., Peña-Montes, C., Mendoza-Hernández, G., & Quirasco, M. Antibacterial activity produced by Enterococcus spp. isolated from an artisanal Mexican dairy product, Cotija cheese. LWT-Food Science and Technology, vol. 59(1), pp. 26-34. Nov. 2014.

[83] Tadic, M., Panjan, M., Damnjanovic, V., & Milosevic, I. Magnetic properties of hematite (α-Fe2O3) nanoparticles prepared by hydrothermal synthesis method. Applied Surface Science, vol. 320, pp. 183-187, Nov. 2014.

[84] Suresh, S. Semiconductor nanomaterials, methods and applications: a review. Nanosci. Nanotechnol, vol. 3(3), pp. 62-74, 2013.

[85] Mohanraj, V. J., & Chen, Y. (2006). Nanoparticles-a review. Tropical journal of pharmaceutical research. vol. 5(1), pp. 561-573, 2006.

[86] Petica, A., Florea, A., Gaidau, C., Balan, D., & Anicai, L. Synthesis and characterization of silver-titania nanocomposites prepared by electrochemical method with enhanced photocatalytic characteristics, antifungal and antimicrobial activity. Journal of Materials Research and Technology, vol. 8(1), pp.41-53, Jan. 2019.

[87] Zhang, X. F., Liu, Z. G., Shen, W., & Gurunathan, S. Silver nanoparticles: synthesis, characterization, properties, applications, and therapeutic approaches. International journal of molecular sciences, vol. 17(9), pp. 1534, Sep. 2016.

[88] Abbasi, E., Milani, M., Fekri Aval, S., Kouhi, M., Akbarzadeh, A., Tayefi Nasrabadi, H., ... & Samiei, M. (2016). Silver nanoparticles: synthesis methods, bio-applications and properties. Critical reviews in microbiology, vol. 42(2), pp. 173-180, Mar. 2016.

[89] Seku, K., Gangapuram, B. R., Pejjai, B., Kadimpati, K. K., & Golla, N. Microwave-assisted synthesis of silver nanoparticles and their application in catalytic, antibacterial and antioxidant activities. Journal of Nanostructure in Chemistry, vol. 8(2), pp. 179-188. Jun. 2018.

[90] Arole, V. M., & Munde, S. V. Fabrication of nanomaterials by top-down and bottom-up approaches-an overview. J. Mater. Sci, vol. 1, pp. 89-93, 2014.

[91] Zhang, F., Wang, X., Liu, H., Liu, C., Wan, Y., Long, Y., & Cai, Z. Recent advances and applications of semiconductor photocatalytic technology. Applied Sciences, vol. 9(12), pp. 2489. Jan. 2019.

[92] Grammatikopoulos, P., Steinhauer, S., Vernieres, J., Singh, V., & Sowwan, M. Nanoparticle design by gas-phase synthesis. Advances in Physics: X, vol. 1(1), pp. 81-100, Jan. 2016.

[93] Pareek, V., Bhargava, A., Gupta, R., Jain, N., & Panwar, J. Synthesis and applications of noble metal nanoparticles: a review. Advanced Science, Engineering and Medicine, vol.9(7), pp. 527-544, Jul. 2017.

[94] Kumar, H., Barman, P. B., & Singh, R. R. Effect of size and shell: enhanced optical and surface properties of CdS, ZnS and CdS/ZnS quantum dots. Physica E: Low-Dimensional Systems and Nanostructures, vol. 67, pp. 168-177. Mar. 2015.

[95] Henglein, A. (1992). Chemistry and Optical Properties of Small Metal Particles in Aqueous Solution. MRS Online Proceedings Library (OPL), vol. 272. 1992.

[96] Camargo, E. R., Popa, M., Frantti, J., & Kakihana, M. Wet-chemical route for the preparation of lead zirconate: An amorphous carbon-and halide-free precursor synthesized by the hydrogen peroxide-based route. Chemistry of materials, vol. 13(11), 3943-3948. Nov. 2001

[97] Satyanarayana, V. N. T. K., Karakoti, A. S., Bera, D., & Seal, S. One dimensional nanostructured materials. Prog. Mater. Sci, vol. 52(5), pp. 699-913, 2007.

[98] Bera D., Kuiry S.C., Seal S. Synthesis of nanostructured materials using template-assisted electrodeposition. JOM. 2004;56:49–53. doi: 10.1007/s11837-004-0273-5.

[99] Alivisatos, A. P. Science 271 933 Alivisatos AP 1996. J. Phys. Chem, vol. 100, pp. 13226, 1996.

[100] Bera, D., Qian, L., & Holloway, P. H. Phosphor quantum dots. Luminescent materials and applications, vol. (25), 19. Mar. 2008.

[101] Mahajan M.R.S., Dubey R.B., Mahajan J., ―Characteristics and properties of CdSe quantum dots‖, Int. J. Latest Res. Sci. Tech, vol. 2, pp. 457-459, 2013.

[102] Scherer, A., Craighead, H. G., & Beebe, E. D. Gallium arsenide and aluminum gallium arsenide reactive ion etching in boron trichloride/argon mixtures. Journal of Vacuum Science & Technology B: Microelectronics Processing and Phenomena, vol. 5(6), pp. 1599-1605, Nov. 1987.

[103] Tsutsui, K., Hu, E. L., & Wilkinson, C. D. Reactive ion etched II-VI quantum dots: dependence of etched profile on pattern geometry. Japanese journal of applied physics, 32(12S), pp. 6233, Dec. 1993.

[104] Chason, E., Picraux, S. T., Poate, J. M., Borland, J. O., Current, M. I., Diaz de La Rubia, T., ... & Tasch, A. F. (1997). Ion beams in silicon processing and characterization. Journal of applied physics, vol. 81(10), pp. 6513-6561. May. 1997.

[105] Debasis, B., Lei, Q., & Subir, S. Photoluminescence of ZnO quantum dots produced by a sol—gel process [J]. Opt Mater, vol. 30, pp. 1233, 2008.

[106] Anderson, L. S. Semiconductor clusters in the sol-gel process: quantized aggregation, gelation, and crystal growth in concentrated ZnO colloids. J. Am. Chem. Soc, vol. 113, pp. 2826-2833, 1991.

[107] Bera, D., Qian, L., & Holloway, P. H. Time-evolution of photoluminescence properties of ZnO/MgO core/shell quantum dots. Journal of Physics D: Applied Physics, vol. 41(18), pp. 182002. Aug. 2008.

[108] Bang, J., Yang, H., & Holloway, P. H. Enhanced and stable green emission of ZnO nanoparticles by surface segregation of Mg. Nanotechnology, vol. 17(4), pp. 973. Jan. 2006.

[109] Sashchiuk, A., Lifshitz, E., Reisfeld, R., Saraidarov, T., Zelner, M., & Willenz, A. Optical and conductivity properties of PbS nanocrystals in amorphous zirconia sol-gel films. Journal of sol-gel science and technology, vol. 24(1), pp. 31-38. May. 2002.

[110] Mallouk, T. E., Webber, S. E., & White, J. M. Demonstration of a shell-core structure in layered CdSe-ZnSe small particles by X-ray photoelectron and Auger spectroscopies. J. Phys. Chem, vol. 96, pp. 3812-3811. 1992.

[111] Yang, H., Santra, S., & Holloway, P. H. Syntheses and applications of Mn-doped II-VI semiconductor nanocrystals. Journal of nanoscience and nanotechnology, vol. 5(9), pp. 1364-1375. Sep. 2005.

[112] Yang, H., Holloway, P. H., Cunningham, G., & Schanze, K. S. CdS: Mn nanocrystals passivated by ZnS: Synthesis and luminescent properties. The Journal of chemical physics, vol. 121(20), pp.10233-10240. Nov. 2004.

[113] Murrag, C. B., Norris, D. B., & Bawendi, M. G. ‘Synthesis and characterization of nearly monodisperse CdE (E= S, Se, Te) semiconductor nanocrystallite. J. Am. Chem. Soc, vol. 115(19), pp. 8706-8715. 1993.

[114] Qu, L., & Peng, X. Control of photoluminescence properties of CdSe nanocrystals in growth. Journal of the American Chemical Society, vol.124(9), pp. 2049-2055, Mar. 2002.

[115] Yu, W. W., Wang, Y. A., & Peng, X. Formation and stability of size-, shape-, and structure-controlled CdTe nanocrystals: ligand effects on monomers and nanocrystals. Chemistry of Materials, vol. 15(22), pp. 4300-4308, Nov. 2003.

[116] Talapin, D. V., Haubold, S., Rogach, A. L., Kornowski, A., Haase, M., & Weller, H. A novel organometallic synthesis of highly luminescent CdTe nanocrystals. The Journal of Physical Chemistry B, vol. 105(12), pp. 2260-2263. Mar. 2001.

[117] Singh, S., Rama, N., & Ramachandra Rao, M. S. Influence of d-d transition bands on electrical resistivity in Ni doped polycrystalline ZnO. Applied physics letters, vol. 88(22), pp222111, May. 2006.

[118] Yang, H., Lee, H., & Holloway, P. H. Anisotropic growth of luminescent Eu3+-or Er3+-doped Gd2O3 nanocrystals. Nanotechnology, vol. 16(12), pp. 2794, Oct. 2005.

[119] Chena, H. S., Wang, S. J. J., Lo, C. J., & Chi, J. Y. (2005). White-light emission from organics-capped ZnSe quantum dots and application in white-light-emitting diodes. Applied Physics Letters, vol.86, pp.131905, 2005.

[120] Bakueva, L., Musikhin, S., Hines, M. A., Chang, T. W., Tzolov, M., Scholes, G. D., & Sargent, E. H. Size-tunable infrared (1000–1600 nm) electroluminescence from PbS quantum-dot nanocrystals in a semiconducting polymer. Applied physics letters, vol. 82(17), pp. 2895-2897, Apr. 2003.

[121] Battaglia, D., & Peng, X. Formation of high quality InP and InAs nanocrystals in a noncoordinating solvent. Nano Letters, vol. 2(9), pp. 1027-1030, Sep. 2002.

[122] Guo, J., Yang, W., Deng, Y., Wang, C., & Fu, S. Organic-dye-coupled magnetic nanoparticles encaged inside thermoresponsive PNIPAM microcapsules. small, vol. 1(7), pp. 737-743, Jul. 2005.

[123] Zenke, M., Offergeld, A., Becker, C., Baek, J. H., Ding, X., Döring, Y., ... & Guhe, Z. Gene Function in Cell Growth, Differentiation & Development. Helmholtz-Institute for Biomedical Engineering Annual Report, vol. 12, 2005.

[124] Yu, H., Gao, Z., Feng, Z., Shu, Y., Xiang, N., Zhou, L., ... & Yang, W. Clinical characteristics of 26 human cases of highly pathogenic avian influenza A (H5N1) virus infection in China. PloS one, vol. 3(8), e2985, Aug. 2008.

[125] Xu, C., Mu, L., Roes, I., Miranda-Nieves, D., Nahrendorf, M., Ankrum, J. A., ... & Karp, J. M. Nanoparticle-based monitoring of cell therapy. Nanotechnology, vol. 22(49), 494001, Nov. 2011.

[126] Sahoo, Y., Goodarzi, A., Swihart, M. T., Ohulchanskyy, T. Y., Kaur, N., Furlani, E. P., & Prasad, P. N. Aqueous ferrofluid of magnetite nanoparticles: fluorescence labeling and magnetophoretic control. The Journal of Physical Chemistry B, vol. 109(9), pp. 3879-3885, Mar. 2005.

[127] Huh, Y. M, Jun Y–W, Song H–T, Kim S, Choi JS, Lee JH, Yoon S, Kim KS, Shin JS, Suh JS, Cheon J: In vivo magnetic resonance detection of cancer by using multifunctional magnetic nanocrystals. J Am Chem Soc, vol. 127, pp. 12387-12391, 2005.

[128] Gao, J., Gu, H., & Xu, B. Multifunctional magnetic nanoparticles: design, synthesis, and biomedical applications. Accounts of chemical research, vol. 42(8), pp. 1097-1107, Aug. 2009.

[129] Liu, Z., Kiessling, F., & Gätjens, J. Advanced nanomaterials in multimodal imaging: design, functionalization, and biomedical applications. Journal of Nanomaterials, vol. 2010. Jun. 2010.

[130] Ghosh Chaudhuri, R., & Paria, S. Core/shell nanoparticles: classes, properties, synthesis mechanisms, characterization, and applications. Chemical reviews, vol. 112(4), pp. 2373-2433. Apr. 2012.

[131] Nomoev, A. V., Bardakhanov, S. P., Schreiber, M., Bazarova, D. G., Romanov, N. A., Baldanov, B. B., ... & Syzrantsev, V. V. Structure and mechanism of the formation of core–shell nanoparticles obtained through a one-step gas-phase synthesis by electron beam evaporation. Beilstein journal of nanotechnology, vol. 6(1), pp. 874-880, Mar. 2015.

[132] Sahu, G., Wang, K., Gordon, S. W., Zhou, W., & Tarr, M. A. Core-shell Au–TiO 2 nanoarchitectures formed by pulsed laser deposition for enhanced efficiency in dye sensitized solar cells. RSC advances, vol. 2(9), pp. 3791-3800, 2012.

[133] Ishii, M., Kato, H., Hashimoto, I., & Homma, Y. Graphite-encapsulated alumina nanoparticles fabricated by hot-filament chemical vapor deposition. Materials Express, vol. 3(4), pp. 355-359, Dec. 2013.

[134] Ishii, M., Kato, H., Hashimoto, I., & Homma, Y. Synthesis of sapphire nanoparticles with graphite shells by hot-filament chemical vapor deposition. Materials Express, vol. 4(2), pp. 135-143, Apr. 2014.

[135] Temuujin, J., Bardakhanov, S. P., Nomoev, A. V., Zaikovskii, V. I., Minjigmaa, A., Dugersuren, G., & Van Riessen, A. Preparation of copper and silicon/copper powders by a gas evaporation-condensation method. Bulletin of Materials Science, vol. 32(5), pp. 543, Oct. 2009.

[136] Nomoev, A. V., & Bardakhanov, S. P. Synthesis and structure of Ag-Si nanoparticles obtained by the electron-beam evaporation/condensation method. Technical Physics Letters, 38(4), pp. 375-378, Apr. 2012.

[137] Lysenko, V. I., Bardakhanov, S., Korchagin, A., Kuksanov, N., Lavrukhin, A., Salimov, R., ... & Nomoev, A. Possibilities of production of nanopowders with high power ELV electron accelerator. Bulletin of Materials Science, vol. 34(4), pp. 677-681, Jul. 2011.

[138] Bardakhanov, S. P., Korchagin, A. I., Kuksanov, N. K., Lavrukhin, A. V., Salimov, R. A., Fadeev, S. N., & Cherepkov, V. V. Nanopowder production based on technology of solid raw substances evaporation by electron beam accelerator. Materials Science and Engineering: B, vol. 132(1-2), pp. 204-208, Jul. 2006.

[139] Bardakhanov, S. P., Korchagin, A. I., Kuksanov, N. K., Lavrukhin, A. V., Salimov, R. A., Fadeev, S. N., & Cherepkov, V. V. Dokl. Phys, 2006.

[140] Wang, G., Gao, Y., Huang, H., & Su, X. Multiplex immunoassays of equine virus based on fluorescent encoded magnetic composite nanoparticles. Analytical and bioanalytical chemistry, vol. 398(2), pp. 805-813, Sep. 2010.

[141] Wang, G., Xie, P., Xiao, C., Yuan, P., & Su, X. Magnetic fluorescent composite nanoparticles for the fluoroimmunoassays of newcastle disease virus and avian virus arthritis virus. Journal of fluorescence, vol. 20(2), 499-506, Mar. 2010.

[142] Pan, Y., Zhao, Q., Li, S., Li, Z., Zhou, X., Zhang, Q., & Sun, L. Fluorescent-magnetic nanocomposites grafted with mannose derivatives: preparation, characterization, and bioapplication. Journal of nanoparticle research, vol. 16(4), pp. 1-14, Apr. 2014.

[143] Hu, J., Wen, C. Y., Zhang, Z. L., Xie, M., Hu, J., Wu, M., & Pang, D. W. Optically encoded multifunctional nanospheres for one-pot separation and detection of multiplex DNA sequences. Analytical chemistry, vol. 85(24), pp. 11929-11935, Dec. 2013.

[144] Tsai, H. Y., Chang, C. Y., Li, Y. C., Chu, W. C., Viswanathan, K., & Fuh, C. B. Detection of carcinoembryonic antigen using functional magnetic and fluorescent nanoparticles in magnetic separators. Journal of Nanoparticle Research, vol. 13(6), pp. 2461-2467, Jun. 2011.

[145] Lambregts, D. M., Maas, M., Stokkel, M. P., & Beets-Tan, R. G. Magnetic resonance imaging and other imaging modalities in diagnostic and tumor response evaluation. In Seminars in radiation oncology, Vol. 26, No. 3, pp. 193-198, Jul. 2016.

[146] Shen, J., Li, Y., Zhu, Y., Yang, X., Yao, X., Li, J., ... & Li, C. Multifunctional gadolinium-labeled silica-coated Fe 3 O 4 and CuInS 2 nanoparticles as a platform for in vivo tri-modality magnetic resonance and fluorescence imaging. Journal of Materials Chemistry B, vol. 3(14), pp. 2873-2882, 2015.

[147] Glasgow, M. D., & Chougule, M. B. Recent developments in active tumor targeted multifunctional nanoparticles for combination chemotherapy in cancer treatment and imaging. Journal of biomedical nanotechnology, vol. 11(11), pp. 1859-1898, Oct. 2015.

[148] Xing, X., Zhang, B., Wang, X., Liu, F., Shi, D., & Cheng, Y. An “imaging-biopsy” strategy for colorectal tumor reconfirmation by multipurpose paramagnetic quantum dots. Biomaterials, vol. 48, pp. 16-25, Apr. 2015.

[149] Shen, M., Jia, W., Lin, C., Fan, G., Jin, Y., Chen, X., & Chen, G. (2014). Facile synthesis of folate-conjugated magnetic/fluorescent bifunctional microspheres. Nanoscale research letters, vol. 9(1), pp. 1-8, Dec. 2014.

CHAPTER -2

SYNTHESIS, CHARACTERIZATION AND EVALUATION TECHNIQUES

$$6NH_3+6Cl^- \rightarrow 4NH_4Cl+2HCl+N_2\uparrow$$

$$CS(NH_2)_2+OH^- \rightarrow CH_2N_2+H_2O+HS^-$$

$$HS^-+OH^- \rightarrow S^{2-}+H_2O$$

$$Cd^{2+}+S^{2-} \rightarrow CdS$$

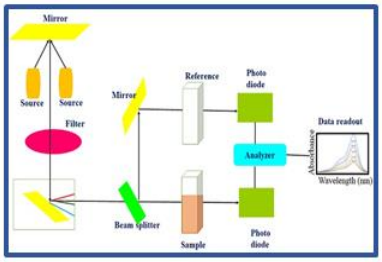

$$\frac{1}{d^2} = \frac{4}{3}\left(\frac{h^2+hk+k^2}{a^2}\right) + \frac{l^2}{c^2}$$

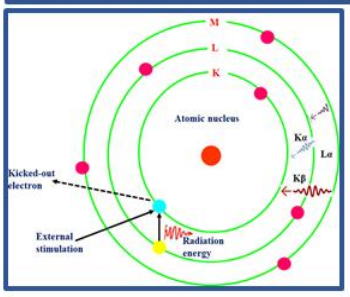

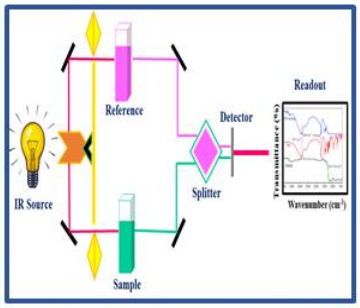

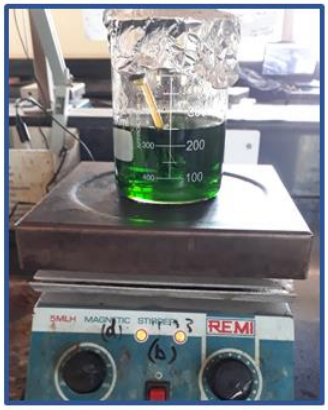

2.1 Introduction

Chapter gives thorough statistics on the synthesis methods of $NiZnFe_2O_4$, $SrFe_{12}O_{19}$, $NiZnFe_2O_4$/CdS CSNs and the $SrFe_{12}O_{19}$/CdS CSNs. Distinct set of CSNs were synthesised using three different loadings of core i.e., 0.2g, 0.1g and 0.05g, also the shell particle size is altered using the different concentration of 2-mercaptoethenol which is used as the capping agent in all the synthesized core-shell nanostructures. "X-ray diffraction (XRD), Transmission Electron Microscope (TEM), UV-vis absorption spectroscopy (UV-vis), photoluminescence (PL) spectroscopy, Vibrating Sample Magnetometer (VSM), and Fourier Transmission Infrared Spectroscopy" were used to investigate structural, morphological, optical, and magnetic parameters, as well as the existence of various functional groups and the study of different types of bonds (using FT-IR). This chapter details about all of the investigational practices which were employed in this examine. Discrete synthesis approaches for the ferrites and their core-shell nanostructures have been discussed in chapter 1. Out of all these methods we have selected "sol-gel" technique for the ferrite synthesis and the seed mediated aqueous "wet chemical aqueous route" for the synthesis of core-shell nanostructures because of their improved replicability, economic efficacy, and environmental friendliness. To stabilise particle size, these synthesis process necessitates the use of a capping agent. Sulfhydryl and carboxyl functional groups in capping agents are commonly selected.

2.2 Synthesis of $NiZnFe_2O_4$ Magnetic Nanoparticle

2.2.1 Chemicals required for $NiZnFe_2O_4$ synthesis

Nickel nitrate hexahydrate ($Ni(NO_3)_2.6H_2O$), Zinc nitrate hexahydrate ($Zn(NO_3)_2.6H_2O$) Ferric nitrate nonahydrate ($Fe(NO_3)_3.9H_2O$), citric acid monohydrate and $C_6H_8O_7.H_2O$ ammonia solution (25%) was taken as pH controller for synthesis. The precursors (AR Grade, Merck) were utilised without additional purification as received. During the synthesis, double-distilled water was used.

2.2.2 Synthesis procedure of $NiZnFe_2O_4$

We attempted to synthesise multiple batches of $NiZnFe_2O_4$ (NZF)in order to find the best synthesis procedure to move forward with. The metal nitrate aqueous solution was made by dissolving stoichiometric quantities of nitrates in double distilled water under continuous stirring for 30 minutes. Then, in 1:3 nitrates to citric acid molar ratio, an aqueous solution of citric acid monohydrate was incorporated to the above mixture. To achieve the appropriate pH

of 7, aqueous ammonia solution was added drop by drop to the mixture. The mixture was maintained to temperature of 75°C±2°C with constant stirring until it turned into gel. In an oven, the gel was dried for 24 hours at 1100±5°C. The resulting product was then annealed for five hours at 900°C and 1100°C to produce the required $Ni_{0.6-x}Zn_{0.4}Fe_2O_4$ nanoparticles. Figure 2.1 depicts a schematic diagram of the sol-gel process. The chemical reaction of ferrites generated by the sol-gel scheme is as follows:

(1) $(0.6\text{-}x)\ Ni\ (NO_3)_2.6H_2O+(0.4)\ Zn\ (NO_3)_2.6H_2O+2Fe\ (NO_3)_3.9H_2O+9C_6H_8O_7.H_2O+NH_3$

$$\xrightarrow{\Delta} Ni_{0.6-x}Zn_{0.4}Fe_2O_4+4N_2\uparrow+54CO_2\uparrow+49H_2\uparrow+8H_2O$$

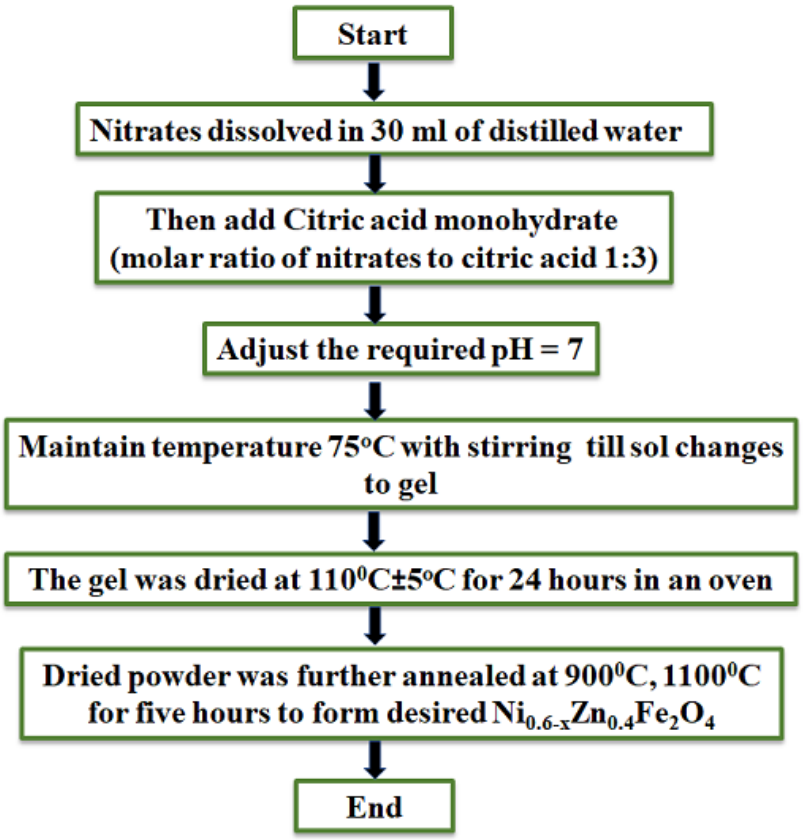

Figure 2.1: Process flow for sol-gel synthesis of $NiZnFe_2O_4$.

2.3 Synthesis of $SrFe_{12}O_{19}$ Magnetic Nanoparticle

2.3.1 Chemicals required for $SrFe_{12}O_{19}$ synthesis

"Ferric nitrate nonahydrate, Strontium nitrate, citric acid monohydrate and ammonium solution (25%) as a pH controller were used in the development of $SrFe_{12}O_{19}$". The compounds (AR Grade) were employed without additional purification and double-distilled water was employed in the synthesis.

2.3.2 Synthesis procedure of $SrFe_{12}O_{19}$

The citrate precursor route was used to make $SrFe_{12}O_{19}$ (SHF). The ideal proportion of metal nitrate was liquified in double distilled water. As a chelating agent, citric acid aqueous solution was added to the nitrate solution mixture. In a molar ratio of 1.57, metal nitrates and citric acid monohydrate were mixed together, according to the composition of strontium ferrite. The pH was then maintained at 7 using an ammonium solution. On constant stirring at 80°C, a homogeneous solution was obtained. The mixture was then evaporated between 75±2^{o} while waiting for mixture to change into gel. To obtain nanocrystalline hexaferrite, the obtained gel was first heat up at 110°C for 5 hours prior being calcined at 900°C and 1000°C (4 hours) to extract preferred residue. Figure 2.2 shows the schematic diagram of the sol-gel process.

The following is the chemical reaction of nanoparticles prepared by the sol-gel method:

(a) Equation involved in the formation of

precursor powder from gel.

$$\text{Gel} \rightarrow Fe_2O_3 + SrO + NH_4NO_3 + CO_2 \uparrow$$

$$SrO + CO_2 \rightarrow SrCO_3$$

$$SrCO_3 + 2\gamma - Fe_2O_3 \rightarrow SrFe_2O_4$$

$$SrFe_2O_4 + 5\gamma - Fe_2O_3 \rightarrow SrFe_{12}O_{19}$$

$$Sr(NO_3)_2 + 12Fe(NO_3)_3.9H_2O + C_6H_8O_7.H_2O + NH_4OH \rightarrow SrFe_{12}O_{19} + NH_4NO_3 + CO_2 + H_2O$$

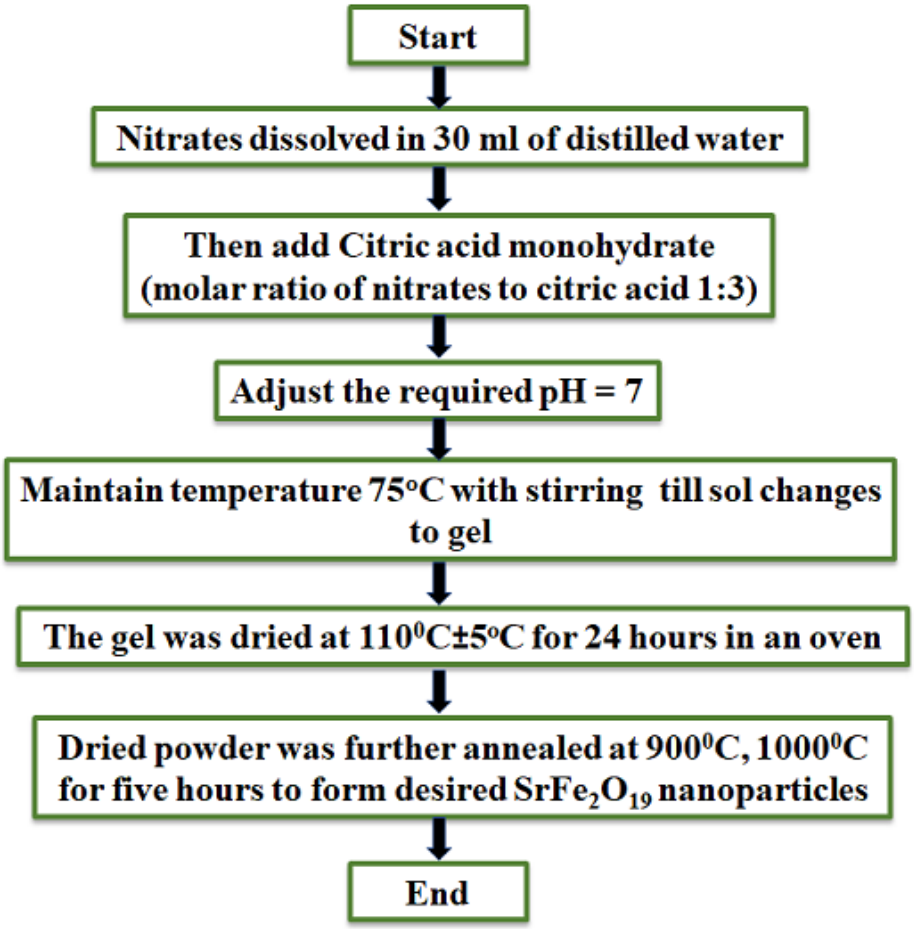

Figure 2.2: Procedure for the sol-gel synthesis of $SrFe_{12}O_{19}$

2.4 Synthesis of Poly CdS and CdS quantum Dots

2.4.1 Chemicals required for CdS synthesis

The reaction process used extra pure ammonium chloride (NH_4Cl), cadmium chloride ($CdCl_2$), ammonia solution (25%) (NH_4OH), thiourea $CS(NH_2)_2$ and 2-mercaptoethanol ($HOCH_2CH_2SH$). The cadmium and sulphur sources are $CdCl_2$ and thiourea, respectively. Merck India chemicals were used in the synthesis. Both analytical grade chemicals were used as it is, with no further refining. Throughout the synthesis, ultra-pure distilled water (Milli-Q, Millipore) was used.

2.4.2 Synthesis procedure of Poly CdS synthesis

We attempted to synthesise many batches of CdS QDs in order to find the best synthesis method for moving forward. The finalised synthesis process for poly CdS is a wet chemical process at 70°C. Double distilled water was used as the solvent for the processing of hydrophilic QDs, the cadmium and sulphur sources are $CdCl_2$ and thiourea, respectively. Ammonia solution was opted as a complexing agent in the process. In current experiment, the

reaction is comprised of NH_4Cl, $CdCl_2$ and thiourea in a 1:1.5:3 molar ratio. The pH was set at 7.5 using NH_3. Following the complete mixing of chlorides in double distilled water, dropwise additions of ammonia solution were made until the pH touched 7.5 value. Dissolved the required measure of thiourea when the pH reached at 7.5. Then solution was continuously stirred for 3 hours. CdS QDs were rinsed several times after the reaction was completed using a centrifuge machine. Figure 2.3 shows the process flow for poly CdS synthesis.

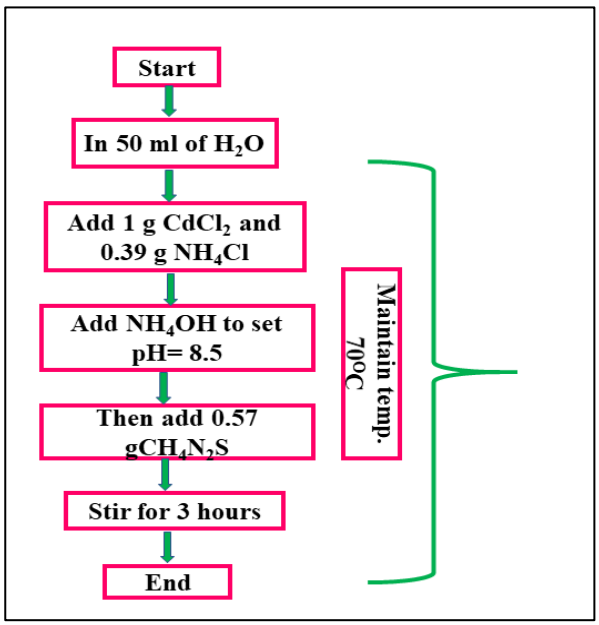

Figure 2.3: Process flow for poly CdS synthesis

2.4.3 Procedure for the synthesis of CdS1, CdS2 and CdS4 QDs

CdS quantum dots (QDs) were prepared via aqueous "wet chemical route" at an optimal temperature of 70°C. The precursors used in the synthesis of CdS QDs were the same as those used in the synthesis of poly CdS. However, to maintain particle size, we have used 5% 2-ME (2-Mercaptoethanol) as a stabilising agent. Different sized CdS QDs were synthesised using diverse amount of 5% 2-ME, independently. On the completion of reaction, centrifugation and the filtration of powder was carried out. The procedure for synthesising all kinds of CdS QDs particles are shown in Figures 2.1 and 2.2. Figure 2.4 shows the process flow for poly CdS synthesis.

The overall reaction for the formation of CdS QDs is outlined below.

2(a) $CdCl_2 \rightarrow Cd^{2+}+2Cl^-$

$NH_4Cl_2 \rightarrow NH_4+2Cl^-$

$Cd^{2+}+2OH^- \rightarrow Cd(OH)_2$

2(b) $6NH_3+6Cl^- \rightarrow 4NH_4Cl+2HCl+N_2\uparrow$

2(c) $CS(NH_2)_2+OH^- \rightarrow CH_2N_2+H_2O+HS^-$

$HS^-+OH^- \rightarrow S^{2-}+H_2O$

$Cd^{2+}+S^{2-} \rightarrow CdS$

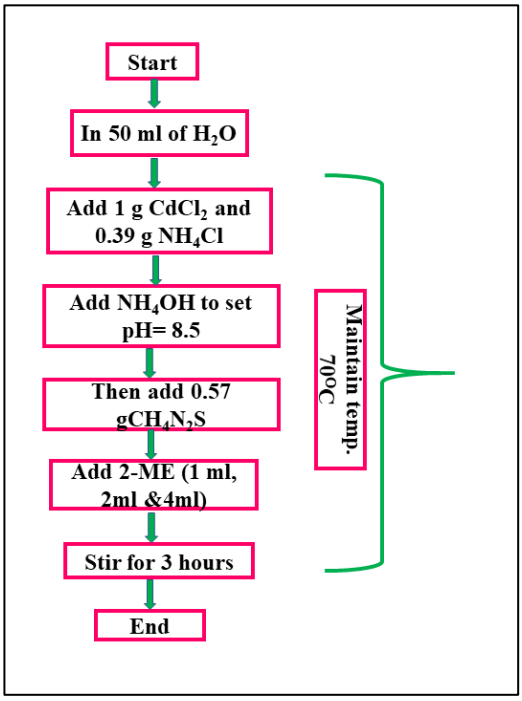

Figure 2.4: Process flow for CdS1, CdS2 and CdS4 QDs synthesis

2.5 Synthesis of $NiZnFe_2O_4$/CdS Core-shell Nanostructure

2.5.1 Chemicals required for $NiZnFe_2O_4$/CdS synthesis

The following chemicals were used in the synthesis: nickel nitrate hexahydrate $(Ni(NO_3)_2.6H_2O$ zinc $(Zn(NO_3)_2.6H_2O)$ nitrate hexahydrate ,ferric nitrate nonahydrate $(Fe(NO_3)_3.9H_2O)$, citric acid monohydrate $C_6H_8O_7.H_2O$, cadmium chloride $(CdCl_2)$, ammonium chloride (NH_4Cl), The compounds (AR Grade, Merck) were utilised as acquired, with no more refinement.

2.5.2 Synthesis procedure of $NiZnFe_2O_4$/CdS

We used the sol-gel process to make Ni-Zn ferrite and the wet chemical method to make CdS quantum dots. Equations (1) and (2) show the chemical reactions for Ni-Zn ferrite synthesised

by sol-gel and CdS QDs synthesised by wet chemical methods, respectively. Following that, we developed $NiZnFe_2O_4$/CdS core-shell nanostructures by dissolving diverse loadings of ferrite (0.2 gm, 0.1 gm, and 0.05 gm) in the CdS solution mixture and adjusting the pH to 7.5 during the CdS synthesis process. The thiourea was then added to the prepared solution. After dissolution of thiourea, a stabilising agent 2-mercaptoethenol was added to attain various sized quantum dots shell. The reaction was heated and stirred continuously for three hours. After that, samples were washed and collected for analysis. Figure 2.5 depicts the process flow for synthesis of $NiZnFe_2O_4$/CdS CSNs.

$NH_4Cl_2 \rightarrow NH_4 + 2Cl^-$

$Cd^{2+} + 2OH^- \rightarrow Cd(OH)_2$

2(b) $6NH_3 + 6Cl^- \rightarrow 4NH_4Cl + 2HCl + N_2\uparrow$

2(c) $CS(NH_2)_2 + OH^- \rightarrow CH_2N_2 + H_2O + HS^-$

$HS^- + OH^- \rightarrow S^{2-} + H_2O$

$Cd^{2+} + S^{2-} \rightarrow CdS$

Throughout overall reaction:

$CdCl_2 + (NH_2)_2CS + 2NH_4OH \rightarrow CdS + CH_2N_2 + 2NH_4Cl + 2H_2O$

The overall reaction for the core-shell formation is described below.

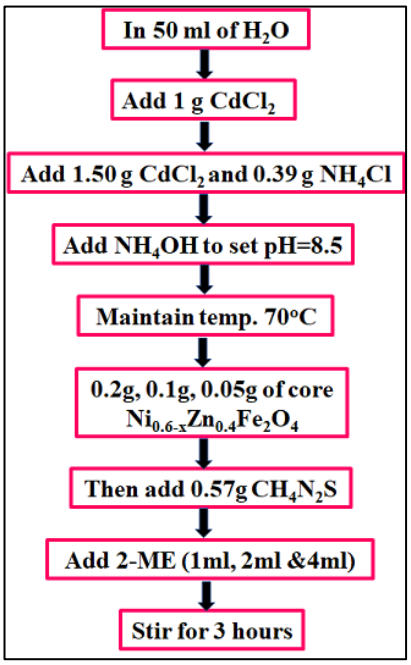

Figure 2.5: Procedure for synthesis of CdS1, CdS2, CdS4 and $NiZnFe_2O_4$/CdS core-shell nanostructures

2.6 Synthesis of $SrFe_{12}O_{19}$/CdS Core-shell Nanostructure

2.6.1 Chemicals required for $SrFe_{12}O_{19}$/CdS synthesis

Ferric nitrate nonahydrate, strontium nitrate, citric acid monohydrate, cadmium chloride ($CdCl_2$), ammonium chloride (NH_4Cl), thiourea $CS(NH_2)_2$ and ammonium solution (25 %) as pH controller. 2-mercaptoethenoal is used as stabilizing agent. The compounds (AR Grade, Merck) were employed without extra purification as obtained. During the synthesis, double-distilled water was used.

2.6.2 Synthesis procedure of $SrFe_{12}O_{19}$/CdS

SHF core-shell nanostructures with CdS quantum dots were produced using an aqueous method with water as the solvent. The entire core-shell is designed using the "seed growth process." The growth of CdS QDs on the ferrite surface is aided by the presence of strontium hexaferrite as a substrate. CdS QDs acted as seeds that sprouted on the surface of Strontium hexaferrite. The aqueous sol-gel approach is used in the synthesis of SHF. To make a mixture of metal nitrate precursors, stoichiometric ratios of nitrates with optimised compositions were mixed in distilled water and agitated until the nitrates were completely dissolved. Aqueous solution of citric acid monohydrates was thawed in the nitrate solution to retain the nitrate to citric acid molar ratio at 1:3. Ammonia solution was used to boost the pH to 7. The solution was then heated for several hours at a temperature range of 85^{o}C with persistent stirring till the liquid solution transformed into a viscous gel. The gel was dried in a hot air oven at 110°C for 24 hours. The dry powder was then annealed for five hours at 900^{o}C and 1000^{o}C to form the desired SHF nanoparticles. SHF were incorporated as a substrate during the CdS QDs synthesis to prepare SHF/CdS CSNs. The CdS solution is made according to the instructions in the previous papers we have reported. SHF nanoparticles were inserted into the CdS QDs solution as synthesised SHF nanoparticles, and then thiourea was injected instantly, followed by 2-mercaptoethanol solutions for different combinations of core and shells. Figure 2. 6 depicts the process flow for $SrFe_{12}O_{19}$/CdS CSNs.

Reaction involved:

$$Gel \rightarrow Fe_2O_3 + SrO + NH_4NO_3 + CO_2 \uparrow$$

$$SrO + CO_2 \rightarrow SrCO_3$$

$$SrCO_3 + 2\gamma - Fe_2O_3 \rightarrow SrFe_2O_4$$

$$SrFe_2O_4 + 5\gamma - Fe_2O_3 \rightarrow SrFe_{12}O_{19}$$

$$Sr(NO_3)_2 + 12Fe(NO_3)_3.9H_2O + C_6H_8O_7.H_2O + NH_4OH \rightarrow SrFe_{12}O_{19} + NH_4NO_3 + CO_2 + H_2O$$

(b) Reaction involved in the growth of CdS seeds over the substrate.

(i) $CdCl_2 \rightarrow Cd^{2+} + 2Cl^-$

$$NH_4Cl \rightarrow NH_4 + 2Cl^-$$

$$Cd^{2+} + 2OH^- \rightarrow Cd(OH)_2$$

(ii) $6NH_3 + 6Cl^- \rightarrow 4NH_4Cl + 2HCl + N_2 \uparrow$

(iii) $CS(NH_2)_2 + OH^- \rightarrow CH_2N_2 + H_2O + HS^-$

$$HS^- + OH^- \rightarrow S^{2-} + H_2O$$

$(Cd^{2+} + S^{2-} \rightarrow CdS$

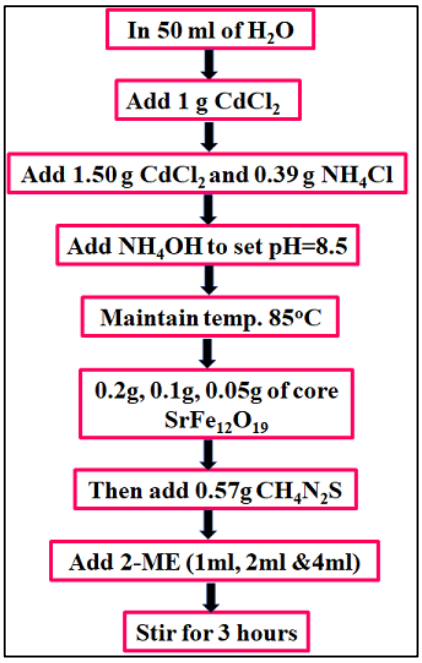

Figure 2.6: Procedure for synthesis of CdS1, CdS2, CdS4 and $SrFe_{12}O_{19}$/CdS CSNs

2.7 Characterization techniques

2.7.1 X-ray diffractometer (XRD)

In the field of material science, "X-ray powder diffraction" is a striking means in the investigation of structural properties of nanomaterials. XRD is made up of three main components: An X-ray tube, an X-ray detector, and a sample holder. The "Shimadzu (XRD 6000) X-Ray diffractometer" used for experiments is shown in Figure 2.7. XRD is a common non-destructive method for crystalline material characterization. This technique provides data on crystal structure, atomic spacing, phases, desired structure positionings, and a variety of further constraints like crystal defects, size and strain.

A sample XRD graph is a stain of sporadic atomic measurements in a specific substance. A cathode ray tube produces X-rays, which are subsequently sieved to produce unicolor radiation, which is then collimated to concentrate in the sample's direction (Figure 2.8). Diffracted rays are generated when the incident beam interacts with the sample. Bragg's law determines the distance between diffracted atomic planes by relating the λ of electromagnetic energy to the lattice spacing and the angle of diffraction, i.e. $n\lambda = 2d\sin\theta$. Since each sample has a different value of d-spacings, changing the diffraction peak to d-spacings allows for sample identification [1].

Figure 2.7: "Shimadzu (XRD 6000) X-Ray diffractometer"

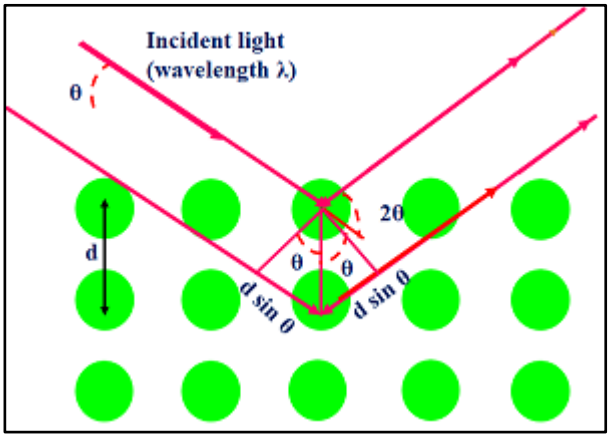

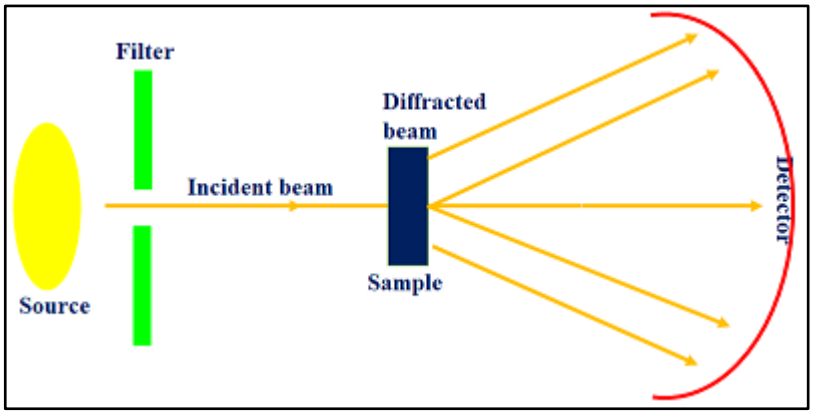

Figure 2.8: Diagram for Bragg's and "X-ray diffraction"

2.7.2 "Transmission electron microscopy (TEM)"

"Transmission electron microscopy" (TEM) is a method for visualising and analysing a specimen's crystal structure and microstructure. A photograph of "Hitachi (H-7500) a transmission electron microscope (TEM)" is shown in Figure 2.9 [2] along with the detailed schematic (Figure 2.10). By illuminating a sample with an electron beam, a TEM image is produced. The focal, intermediate, and projector lenses in the image producing device below the sample location are in charge for focusing the electron towards the specimen and thus responsible for creating exceedingly magnified image onto the screen. The pictures that are created are unicolor and can be stored on systems.

For the observation of a sample, TEM proposes two modes: diffraction mode and picture mode. Diffraction mode, generates a project for specimen by lighting the region with

an electron beam. The diffraction pattern by TEM and XRD identical. The image mode is used to create an image from the sample's illuminating field.

Figure 2.9: Picture of "Transmission electron microscope (TEM): Hitachi (H-7500)"

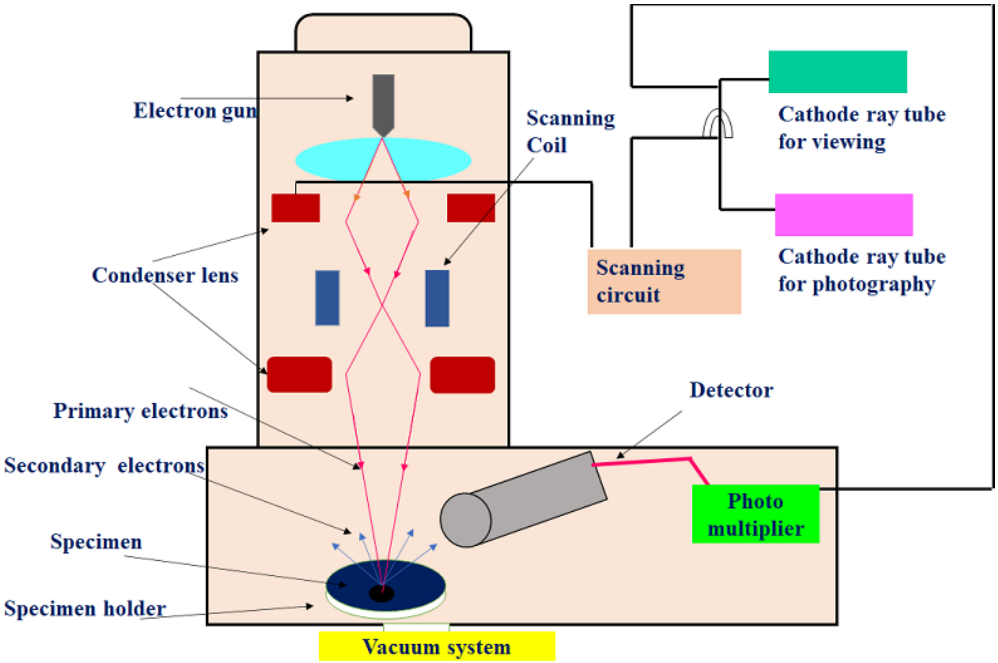

Figure 2.10: Ray diagram of "Transmission electron microscope"

2.7.3 "Energy dispersive X-ray spectroscopy (EDX)"

EDX is a very effective investigating tool for determining the elements present in sample. "X-rays" are formed in EDX by ionising an atom with high-energy radiation (10-20 KeV), which

causes a vacancy in the inner shell. The incident ray stimulates an electron in the inward shell, emits it from the shell, and creates an electron hole. Following this, higher-energy shell electrons fill the vacuum. The energy is emitted in the form of X-rays in this process. This energy is proportional to the difference in energy between the higher and lower energy shell (Figure 2.11). The energy of the "X-rays" emitted by the analyte is measured using an "energy dispersive spectrometer". These "X-ray" results from the energy difference between the two shells, allowing the essential configuration of the sampling to be determined. We can study the elements present in specimens by investigating the nature of the emitted X-rays. [3].

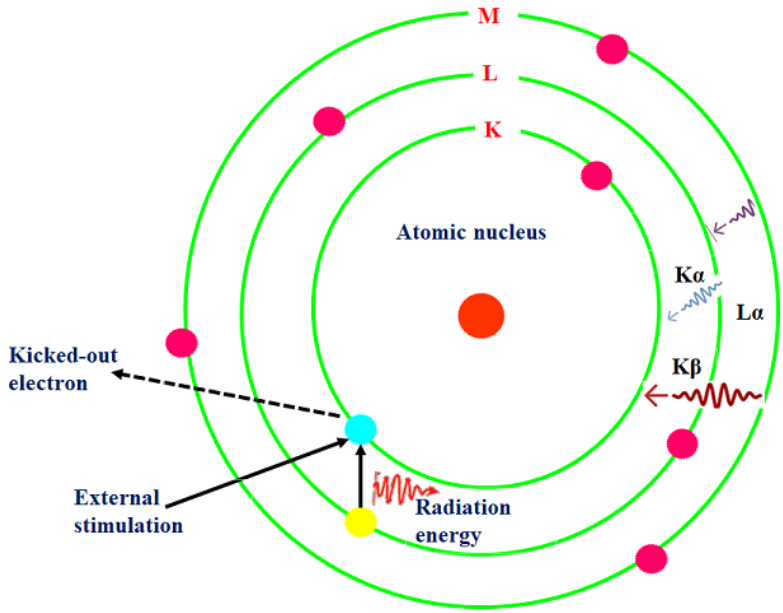

Figure 2.11: Schematic ray diagram of EDX

2.7.4 Field emission scanning electron microscopy (FESEM)

FESEM is a high-resolution microscope that studies the topology, morphology, and structure of materials using electrons rather than light. FESEM images have higher spatial resolution (3-6 times) and magnification (10 X to 300000 X) than scanning electron microscope images (SEM). In FESEM, an electron beam is produced from the cathode through field emission, which results in a narrower beam at low and high electron energy, improving spatial resolution and reducing sample damage. Electrons are released from the source by field emission and accelerated in a high electric field gradient in FESEM. To create a narrow beam, these primary electrons are focused and deflected by electronic lenses in high vacuum. Secondary electrons emitted from the specimen are captured by the detector that generates the electrical signals when a narrow electron beam bombards the sample or specimen. These

electrical signals are then amplified and converted into images, which provide information about the samples. The ray diagram of FESEM is given in figure 2.12.

Figure 2.12: Photograph of "Carl Zeiss Modal No-Ultra Plus-55 FESEM"

2.7.5 Optical Characterization

2.7.5.1 UV-vis-Spectrophotometer

UV spectroscopy involves the molecule absorbing light in the ultra-violet range (200-400 nm). "Perkin-Elmer Lambda 750" "UV-vis Spectrophotometer" was used to measure absorption (Figure 2.13). In UV-vis spectroscopy, light is absorbed, causing electron excitation from the lower to higher state. "UV-vis spectroscopy" is based on the "Beer-Lambert law", which states that the rate at which the strength of a beam of "monochromatic" light reduces due to the width of the engrossing solution is related to incident energy and solution concentration when it travels through a solution of an absorbing substance.

$A=\log (I_0/I) = \varepsilon c l$

A= Absorbance

I_0=Incident light intensity

I= Light incident after passing

c= Solute molar concentration

ε = molar absorptivity

l= Sample cell length

UV-vis apparatus practices “Tungsten filament lamps and Hydrogen-Deuterium lamps” for sources since they coverup entire range. Monochromators are prisms and slits that are widely used in “spectrophotometers”. The energy released by the light is separated by spinning prisms. Slit-selected ray is” monochromatic”, and with the aid of another prism, it is split into two rays. One divided beam pass by the sample solution, whereas second ray pass by the reference solution. Two photocells are found in the detector. The photocells generate very low-intensity current, which is amplified by amplifiers to produce strong signals. The CPU is wired to these amplifiers. The CPU saves all of the data and creates the required compound's spectrum. The ray diagram of a UV-vis-Spectrophotometer is given in Figure 2.14. [4].

Figure 2.13: Picture of UV-visible spectrometer “Perkin-Elmer Lambda 750”

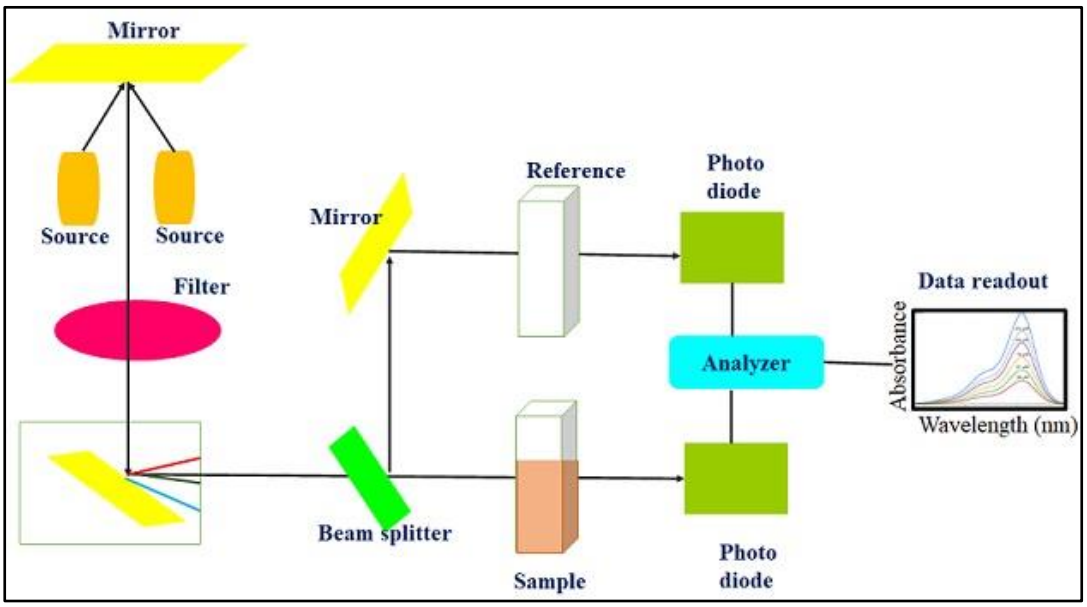

Figure 2.14: Ray diagram of "UV-vis-Spectrophotometer"

2.7.5.2 "Photoluminescence (PL) spectroscopy"

"PL spectrophotometer" is an investigative method for recording a sample's luminescent behaviour. The photo of the "photoluminescence spectrophotometer LS-55" is shown in Figure 2.15.

Figure 2.15: Picture of "photoluminescent spectrophotometer LS-55"

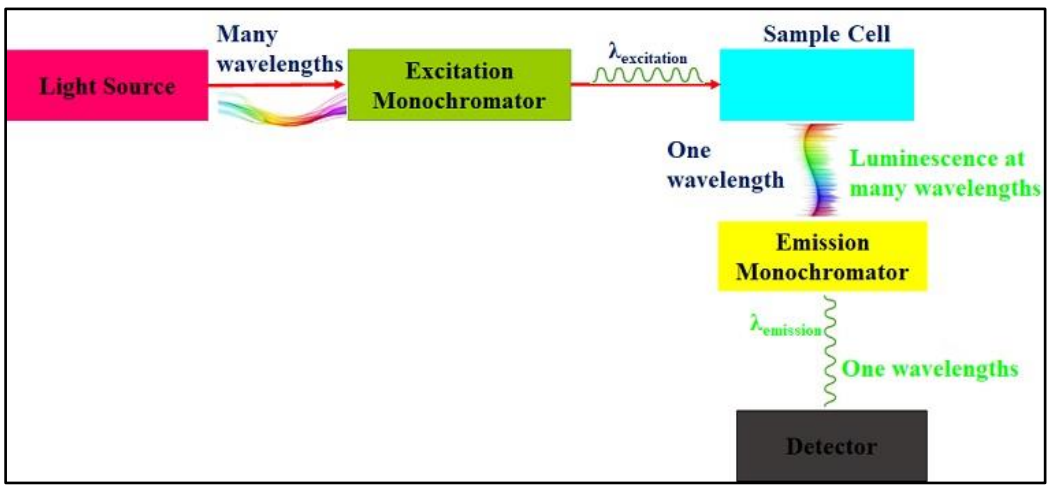

Figure 2.16: Block diagram of "LS-55 Photo Luminescence Spectrophotometer"

The light source for the fluorescence spectrophotometer is a 150 W ozone-free xenon lamp. The elliptical mirror collects the light from the lamp. This light was then concentrated on the excitation monochromator's entrance slit. Monochromators with reflective optics maintain

high resolution throughout the entire spectral spectrum while reducing spherical aberrations. A reflection grating is an essential component of a monochromator. With the aid of its vertical grooves, this grating disperses incident light. Slits in the monochromator's entrance and exit parts can be adjusted at any time. The slits of the emission “monochromator” control the intensity of the fluorescence signal that is eventually captured by the detector. After the exit slit of the excitation monochromator, there is an excitation shutter. The shutter acts as a buffer, protecting the sample from photo bleaching and photo degradation caused by excessive light exposure. An emission shutter protects the detector from bright light by being mounted just before the emission monochromator's entry. The ray diagram of the Photo Luminescence-Spectrophotometer is shown in Figure 2.16 [5].

Photoluminescence is the property of a substance that emits light when it is excited. This method of spectroscopy is flexible, non-destructive, and powerful. Between the conduction and valence bands in semiconducting materials, a radiative transition occurs. To record PL spectra, a laser light with an energy greater than the band gap is used to excite the sample. The excited electrons then relax by recombining with holes and emitting radiation. In the case of semiconductors, these radiative transitions can also include localised impurity and defect states. As a result, PL spectra analysis will reveal defects and impurities, and the magnitude of the PL signal can be used to determine their concentration. It also aids in the comprehension of the recombination mechanism's physics.

2.7.6 Vibrating Sample Magnetometer (VSM)

“VSM model PAR-155” is used for investigating magnetic nature of prepared samples at room temperature in -10 Oersted to + 10 Oersted magnetic field range [6]. Figure 2.17 shows a photograph of a vibrating sample magnetometer model PAR-155. The working of the “Vibrating Sample Magnetometer” is based on the Faraday Laws of Induction, which states that electric field is produced with changing magnetic field. The sample is physically vibrated in the VSM as it is put in a uniform magnetic field, and the induced shifts in the magnetic field are observed by the search coil. Pick up coils calculate the induce shift in field caused by sample movement in up and down directions as a function of time in terms of electric field. The information about changing magnetic fields is provided by the measured electric field, which is proportional to the magnetization of the samples. The induced current in the material increases as the magnetization of the material increases, and this can be amplified, providing knowledge about the magnetic properties of the material such as saturation magnetization,

retentivity, and coercivity. Figure 2.18 shows a schematic diagram of VSM and their components. The magnetic properties of various materials can be determined by graphing the graph of saturation magnetization (MS) versus applied field (H).

Figure 2.17: Picture of "Vibrating sample magnetometer model PAR-155"

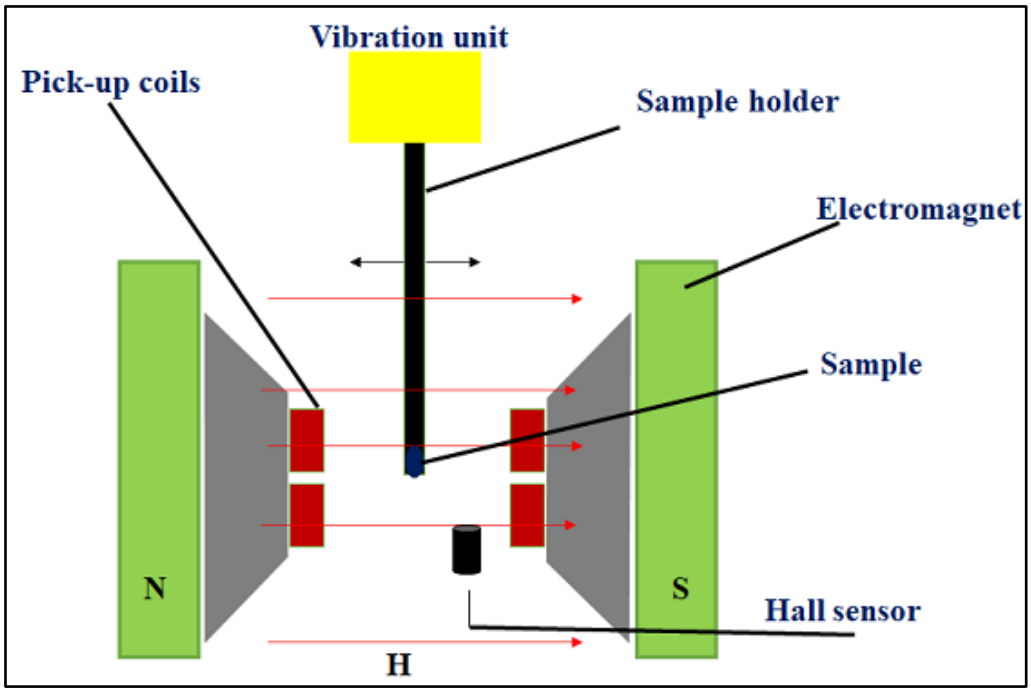

Figure 2.18: Schematic diagram of VSM and their components

2.7.7 "Fourier transforms infrared spectroscopy (FT-IR)"

Figure 2.19 shows a snap of "Cary-630 FT-IR spectrophotometer" [7]. The identification of functional groups in a molecule is done using infrared spectroscopy. This method can also be used to build a one-of-a-kind collection of absorption bands that can be used to test the qualities of a pure substance or detect the presence of specific contaminants. The fact that molecules have precise internal vibration frequencies is the basis for infrared spectroscopy. Frequencies should be in the infrared range, which ranges from 4000 cm^{-1} to 200 cm^{-1}. Infrared spectrometers calculate absorbed wavelengths, and the absorbed energy vs. frequency graph "infrared spectrum". Since different materials have different vibrations and acquiesce special infrared spectra, we can classify substances using FT-IR spectra. Furthermore, absorption frequencies may be used to determine whether or not different chemical groups are present in a chemical structure. The block diagram of a Fourier transforms infrared spectroscope is shown in Figure 2.20.

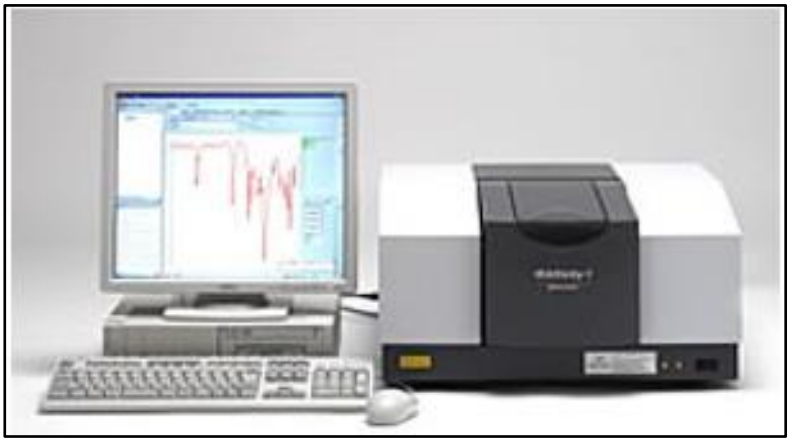

Figure 2.19: Picture of "Fourier transforms infrared spectroscope"

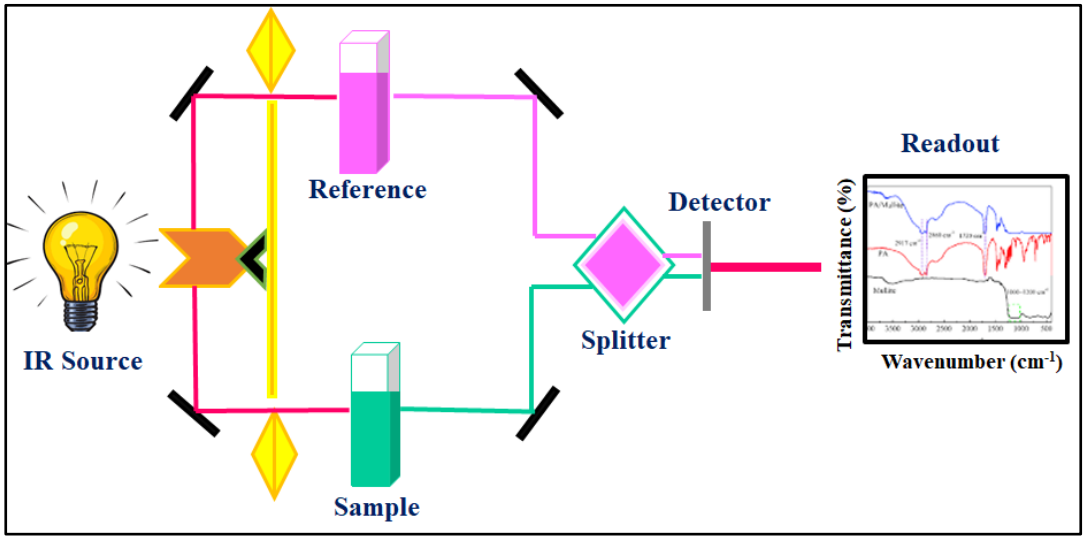

Figure 2.20: Schematic diagram of FTIR and its components

2.8 Derivative spectroscopy Method (DSM)

2.8.1 Derivative spectroscopy method (DSM) for the optical analysis

For qualitative analysis and quantification, with reference to wavelength, DSM uses derivative of absorbance data. “Derivative spectra data was initially given in the 1950s, when it was discovered to offer numerous advantages” [8–10]. The derivative spectra of a spectrum reported as absorbance "A" as a function of wavelength "" are:

$$0 \text{ order, } A = f(\lambda);\ I \text{ order, } dA/d\lambda = f'(\lambda);\ II \text{ order, } d^2A/d\lambda^2 = f''(\lambda)$$

The Ist order derivative, which starts and finishes at zero, governs the variation in absorbance w.r.t λ. Bands perceived is always equal to the one more then derivative order, which is a crucial aspect to remember. We estimated the exact absorbance positions for samples by utilising the 2nd order derivative of absorbance for each sample.

Experimental photoluminescence spectra are resolved with great precision using an enhanced derivative spectroscopy approach. The derivative spectroscopy method has made it possible to discuss some of the aspects that were previously invisible or repressed in PL spectra. When comparing core/shell nanostructures to bare nanoparticles, regardless of how minor the change is, DSM allows us to acquire all of the miniature details about the peak shift and defect states.

2.8.2 Derivative spectroscopy methods (DSM) for the magnetic analysis.

On the as-obtained hysteresis curves, spectroscopy was used to perform a detailed investigation of the magnetic character derivatives. DSM was used to calculate the SFD for the various samples. To characterise the magnetic properties of ferrites and magneto-fluorescent core-shell nano systems, SFDs are critical. The information on spin orientation at high and low magnetic fields is provided by SFD. This information is crucial when comparing the core-shell nanostructure to basic magnetic shell nanoparticles. When switching from bare ferrites to their core-shell nanostructures, a significant difference in SFD was seen. SFD has been estimated by the relation “SFD = ΔH/HC” [11]. SFD is related to size distribution of particle in a nanoparticle medium because size dispersed and profile dispersed units reverses at differing intensities of magnetic fields. [12]. Superior quality can be shown in materials with a high H_C and a lower SFD. A small SFD is generated by a stable switching transition.

Ist derivative of hard ferrite and hard ferrite-based core-shell samples indicated that there are two crests, the first of which is a large crest used to estimate the FWHM for computing the system's SFD, wide hump also reflects the magnetic material's hardness. This wide hump serves as a useful distinction between hard and soft ferrites. The second peak is due to a sharper slop in the small field area.

2.9 Rietveld refinement

Hugo Rietveld invented a technique for characterising crystalline materials called Rietveld refinement. Powder samples diffraction with neutrons and X-rays produces a pattern with reflections (intensity peaks) at certain locations. Many elements of the material's structure can be deduced from the width, height and the position of these reflections. The Rietveld method refines a theoretical line profile using a least squares approach till it matches fine with the experimental profile. The method was a huge step forward in powder sample diffraction analysis because, unlike other techniques at the time, it could reliably deal with significantly overlapping reflections [13]. “Full Prof software” is opted for refining of samples by Rietveld refinement”.

2.10 Formulas

1. The crystallite size (D) of the nanoparticles was measured using Scherer's formula (eqn.2.1)

$$D = K\lambda/\beta \cos\theta \qquad (2.1)$$

In the case of a cubic system, K is Scherer's constant, which has a value of 0.9. [14].

2. The lattice parameters of prepared spinel ferrite nanoparticles, such as lattice constant (a) (eqn.2.2) [15] and d-spacing (d) (eqn.2.3) [16], were determined using the formula.

$$2\,d\sin\theta = n\lambda \qquad (2.2)$$

$$a = d\,(h^2 + k^2 + l^2)^{1/2} \qquad (2.3)$$

where the plane's miller indices are h, k, and l.

3. The lattice parameters such as lattice constant (***a***) (eqn.2.2) and d-spacing (***d***) (eqn.2.3) of prepared hexagonal ferrite nanoparticles were calculated using the formula

$$\frac{1}{d^2} = \frac{4}{3}\left(\frac{h^2+hk+k^2}{a^2}\right) + \frac{l^2}{c^2} \qquad (2.4)$$

where *h*, *k*, and *l* are miller indices of the plane [17].

4. The Stocks-Wilson relation was used to calculate the strain (***ε***) of nanoparticles (eqn.2.4)

$$\varepsilon = \beta/4\tan\theta \qquad (2.5)$$

5. Williamson-Hall (W-H) method was used to calculate **D** and ***ε*** extant in samples. The FWHM of specific peak is stated by relation (eqn.2.5)

$$\beta\cos\theta = K\lambda/D + 4\varepsilon\sin\theta \qquad (2.6)$$

where, D is crystallite size, β is the FWHM of peaks, λ is the Cu Kα radiations wavelength and ε is strain types [18].

6. The "magneto crystalline anisotropy energy" constant (***K***) of prepared nanoparticles has been premeditated via formula (eqn.2.9)

$$H_c = 2K/M_s \qquad (2.7)$$

where H_c and M_s are the coercivity and saturation magnetization of the samples respectively [19].

7. The experimental magnetic moment (***M_μ***) of all prepared samples was calculated using formula

(eqn.2.10) $$M_\mu = (M_w \times M_s)/5585 \qquad (2.8)$$

where M_w denotes the sample's molecular weight and M_s denotes the saturation magnetization of nanoparticles. [19].

8. The formula is used to compute the ferrites' switching field distribution (SFD).

$$SFD = \Delta H/H_C \qquad (2.9)$$

2.11 REFERENCES

[1] Bunaciu A.A., UdriŞTioiu E.G., Aboul-Enein H.Y., "X-ray diffraction: instrumentation and applications", Critical reviews in analytical chemistry, vol. 45(4), pp. 289-299, Oct. 2015.

[2] Wang Z.L., "Transmission electron microscopy of shape-controlled nanocrystals and their assemblies", 2000.

[3] EDX Hafner B., "Energy dispersive spectroscopy on the SEM: a primer", Characterization Facility, University of Minnesota, pp. 1-26, 2006.

[4] Gemta A.B., UV/VIS SPECTROPHOTOMETER (Doctoral dissertation, Addis Ababa University, 2005.

[5] Ye R., Barron A.R., "Photoluminescence Spectroscopy and its Applications", Physical methods in chemistry and nano science, OpenStax CNX, June 2011.

[6] Foner, S. Versatile and sensitive vibrating-sample magnetometer. Review of Scientific Instruments, vol. 30(7), 548-557. 1959.

[7] Doyle W.M., "Principles and applications of Fourier transform infrared (FTIR) process analysis", Process control and quality, vol. 2(1), pp. 11-41, 1992.

[8] Bridge, T. P., Fell, A. F. & Wardman, R. H. Perspectives in derivative spectroscopy Part 1, Theoretical principles. Journal of the Society of Dyers and Colourists 103, pp. 17–27 1987.

[9]. Kus, S., Marczenko, Z. & Obarski, N. Derivative UV–VIS spectrophotometry in analytical chemistry. Chem. Anal. 41, pp. 899–927, 1996.

[10]. Dixit, L. & Ram, S. Quantitative analysis by derivative electronic spectroscopy. Applied Spectroscopy Reviews 21, pp. 311–418, 1985.

[11] S. Kawahara, Y. Nakano, Y. Shimizu. Yamauchi, Magnetic recording medium United States patent., US 5, vol. 188, pp. 907, 1993.

[12] S. Kumar, R.R. Singh, P. B. Barman, Rietveld Refinement and Derivative Spectroscopy of Nanoparticles of Soft Ferrites (MgNiFe), J INORG ORGANOMET P, pp. 1-14, 10.1007/s10904-020-01764-7, 2020.

[13] Rodriguez, C. J. & Fullprof, A. Reitveld refinement and pattern matching analysis program. Laboratory Leon Brillouin (CEA-CNRS) (2011).

[14] Kumar, R., Kumar, H., Kumar, M., Singh, R. R. & Barman, P. B. Enhanced saturation magnetization in cobalt doped Ni-Zn ferrite nanoparticles. Journal of Superconductivity and Novel Magnetism 28, pp. 3557–3564 (2015).

[15] Prabahar S., Dhanam M., "CdS thin films from two different chemical baths—structural and optical analysis", Journal of Crystal growth, vol. 285(1-2), pp. 41-48, Nov. 2005.

[16] Barman J., Sarma K.C., Sarma M., Sarma K., "Structural and optical studies of chemically prepared CdS nanocrystalline thin films", Indian journal of pure and applied physics, vol. 46, pp. 339-343, May 2008.

[17] Rawat, D. and Singh, R.R. Avant-grade magneto/fluorescent nanostructures for biomedical applications: Organized and comprehensive optical and magnetic evaluation. Nano-Structures & Nano-Objects, 26, pp.100714, 2021.

[18] Prabhu, Y. T., Rao, K. V., Kumar, V. S. S., & Kumari, B. S. X-ray analysis by Williamson-Hall and size-strain plot methods of ZnO nanoparticles with fuel variation. World Journal of Nano Science and Engineering, 2014.

[19] Kumar, R., Kumar, H., Kumar, M., Singh, R. R., & Barman, P. B. Enhanced saturation magnetization in cobalt doped Ni-Zn ferrite nanoparticles. Journal of Superconductivity and Novel Magnetism, vol. 28(12), pp. 3557-3564, 2015.

CHAPTER- 3

SYNTHESIS AND CHARACTERIZATION OF NICKEL ZINC FERRITE ($NiZnFe_2O_4$), CADMIUM SULPHIDE (CdS) QUANTUM DOTS (QDS) AND THEIR CORE-SHELL NANOSTRUCTURES FOR DRUG DELIVERY APPLICATIONS

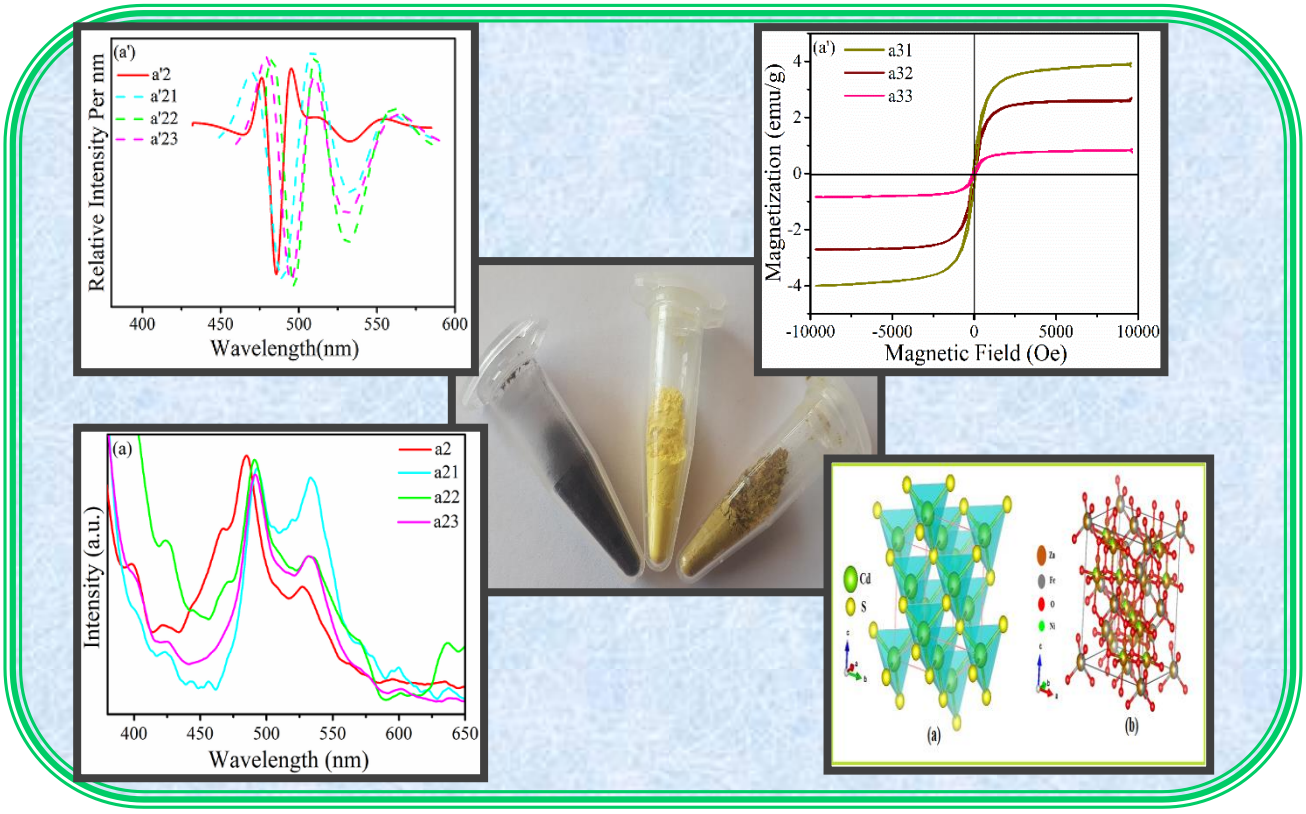

Highlights

- Aqueous synthesis of highly confined luminous CdS QDs.
- Synthesis of Nickel Zinc Ferrite by the sol-gel route.
- Core-shell nanostructures with Nickel Zinc Ferrite core and CdS shell were synthesised.
- Effects of 2-Mercaptoethanol on optical properties and core loading on magnetic properties were investigated.
- Interface of core-shell shows some of the interesting results.
- It has been practically confirmed that the CSNs formed with the minimal core concentration and CdS 2 & CdS1 shell shows the best results.

Abstract

Using NZF as the *"core"* and CdS QDs as the "*fluorescent semiconducting shell"*, a new series of magneto-fluorescent CSNs with outstanding physical and chemical properties were developed. A two-step technique was used to create the magneto-fluorescent nanostructures, which incorporated both "sol-gel" and "wet chemical processes". NZF/CdS CSNs were synthesised for varied loadings of ferrite with varying sizes of CdS QDs, where 2-ME was utilised as a stabilising agent for the regulated growing of CdS QDs. NZF, CdS, NZF/CdS CSNs were studied for their magnetic, optical and structural properties. High-resolution imaging validated the formation of core-shell structures.

3.1 Introduction

The striking candidates for advanced nanomaterials are nanostructures with distinct nanometre scale functionalities [1, 2]. These smart materials will reveal novel physiochemical properties thanks to their balanced interface interaction and structure, which will be crucial for future technological applications [3–8]. As compared to their single constituent materials, these nanostructures have better magnetic, optical, and chemical properties. Due to the combined functionality of core and shell features, which allow them in broad variety of applications, hetero-structured CSNs have recently been the topic of intensive investigation [9–12]. Magneto-fluorescent CSNs preserve optical and magnetic properties of both materials, allowing for potential bioassay applications such as "optical reporters" and "magnetic handles." The Fe based “magneto-fluorescent structures” have been the subject of the majority of available reports. Iron oxide is used in a variety of biomedical applications, but its “magneto-fluorescent” structures are poorly understood [13]. Even though the production of Iron oxide ferrites is a well-established technique, the creation of several phases during the synthesis, such as hematite and magnetite, remains a disadvantage. “Single-phase” spinel ferrite is guaranteed when NZF magnetic nanostructures are prepared with regulated reaction parameters. NZF also has a high resistivity, low saturation magnetization, a high Curie temperature, high mechanical hardness, and chemical stability. As a result, the magneto fluorescent structures based on NZF will be more proficient for their scope in magneto-fluorescent and biological applications. Still, not much research has been done on these types of structures till date. This research delves into the first study of its kind in the region, with the aim of developing structure with unique range of “magneto-optical properties”.

Because of their unusual physical and chemical properties, nanoparticles made of metals such as Ni, Co, and Fe have got a lot of attention. Because of their high resistivity, enhanced magnetization, and chemical steadiness, soft NZF are an important part of the study. “Although CdSe QDs have been extensively studied, we have used CdS instead of CdSe (where the Se ions are replaced by S ions) as a possible approach for reducing the growth of noxious nanoparticles for bio-related applications based on the preceding findings” [14]. “Another reason to employ NZF and CdS as core-shell materials is that, despite the reduction in magnetic behaviour of the core-shell in NZF/CdS compared to bare core NZF, they have persistent coercivity in the CSNs, which is a strong signal for using NZF/CdS in bio-applications” [15].

The aqueous synthesis of strongly confined CdS (1, 2 & 4) that were capped by 2-ME are discussed in this chapter. NZF were produced by the "sol-gel method". Further the core-shell nanostructures were prepared in accordance with the aims of the thesis. As a result, we created core-shell structures with various NZF loadings (0.20 g, 0.10 g & 0.05 g by weight) and varying CdS shells. As prepared nanoparticles have been examined by the means of several practices, and the results of this new type of material are described here.

3.2 Experimental details

CdS QDs of various sizes were made utilising an aqueous chemical method at 70°C. Ferrite nanoparticles were synthesised at 80-90 degrees Celsius before being annealed at high temperatures. The seed growth approach was used to create core/shell nanostructures, in which the core ferrite serves as a substrate for the formation of CdS seeds. The process has been discussed in detail in Chapter 2 (section 2.2.3). Characterization of as prepared samples was achieved by "X-ray diffraction (XRD)", "Transmission electron microscopy (TEM)", "Energy dispersive analysis by X-rays (EDX)", "absorbance spectroscopy", "photoluminescence spectroscopy", "vibrating sample magnetometry (VSM)" and "Fourier transform infrared spectroscopy (FTIR)". "Shimadzu powder x-ray diffractometer" using Cu Kα radiation was used to distinguish various crystal parameters. By placing ultra-thin layer of sample on the surface of copper grid, "transmission electron microscopy (TEM)" was accomplished.

"UV-vis spectroscopy" measurements were done through "PerkinElmer Lambda750 UV–vis spectrophotometer". The luminous behaviour of samples was investigated using a "Perkin Elmer LS55 fluorescence spectrophotometer" in 200-900 nm wavelength range. FTIR spectroscopy was used to confirm the functionality discovered upon the core, shell, and core-shell surface. "The Cary 630 spectrophotometer (Agilent technology)" was used for this work, which had a wavenumber range of 4000 cm^{-1} to 400 cm^{-1}.

3.3 Results and Discussion

NZF is a soft ferrite with exceptional structural and magnetic properties. Because of their high resistance and minimal eddy current losses, they are considered the most adaptable soft ferrites. In NZF, Zn^{2+} and Fe^{3+} ions reside in the T- sites, whereas Ni^{2+} and Fe^{3+} ions occupy the O-sites in the formula AB_2O_4. Quantum dots (QDs) made of cadmium sulphide (CdS) are

binary compound semiconductors with exceptional fundamental optical and electrical characteristics. The spinel structure for the core, as well as for shell are shown in figure 3.1.

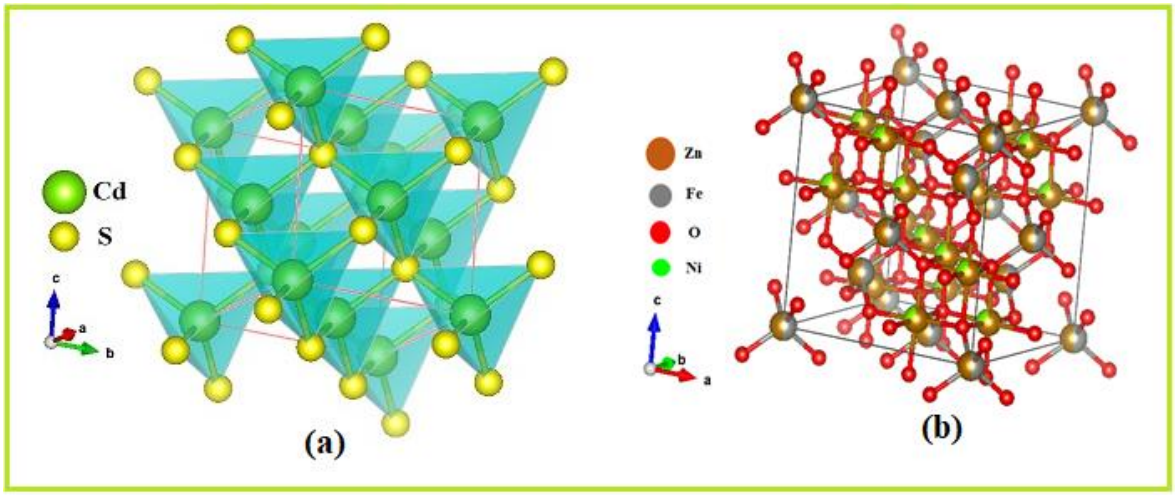

Figure 3.1: (a) Crystal structures of CdS QDs and (b) Crystal structure of Nickel Zinc ferrite

CdS is a well-known direct band gap semiconductor with crystal structures of zinc blende and wurtzite. The properties of both the core and shell are demonstrated in CSNs made using nickel zinc ferrite core and CdS shell.

3.3.1 Structural analysis of CdS QDs, NZF nanoparticles and NZF/CdS CSNs

To learn about structural characteristics, XRD spectra of CdS QDs, NZF, and NZF/CdS CSNs with NZF annealed at temperatures (900°C and 1100°C) were recorded. The graphs for bare core, shell and their CSNs are given in Figure 3.2 (a & b), with the core being annealed at 900°C & 1100°C respectively.

QDs (1, 2 & 4) have three primary peaks at different diffraction angles, as seen in the figure. These peaks are caused by reflections (111), (220), and (311), respectively. The cubic phase of CdS is well aligned with these peaks. For $NiZnFe_2O_4$ annealed at 900°C and 1100°C peaks have been indexed as “(022), (113), (222), (004), (333), and (044)” hkl planes, demonstrating the "single-phase spinel cubic structure" of NZF. On comparing the peak positions of CSNs to bare core and separate shell structures, a shift in the peak position was discovered, confirming the successful creation of core-shell nanostructures. Entire set of samples possess pure crystallinity that were devoid of any form of alloying. Because the spectra for NZF and CdS QDs feature unique peaks, XRD could not be used to calculate

particle sizes for core-shell nanostructures [16]. Tables 3.1 show the results of various parameters derived using XRD spectra.

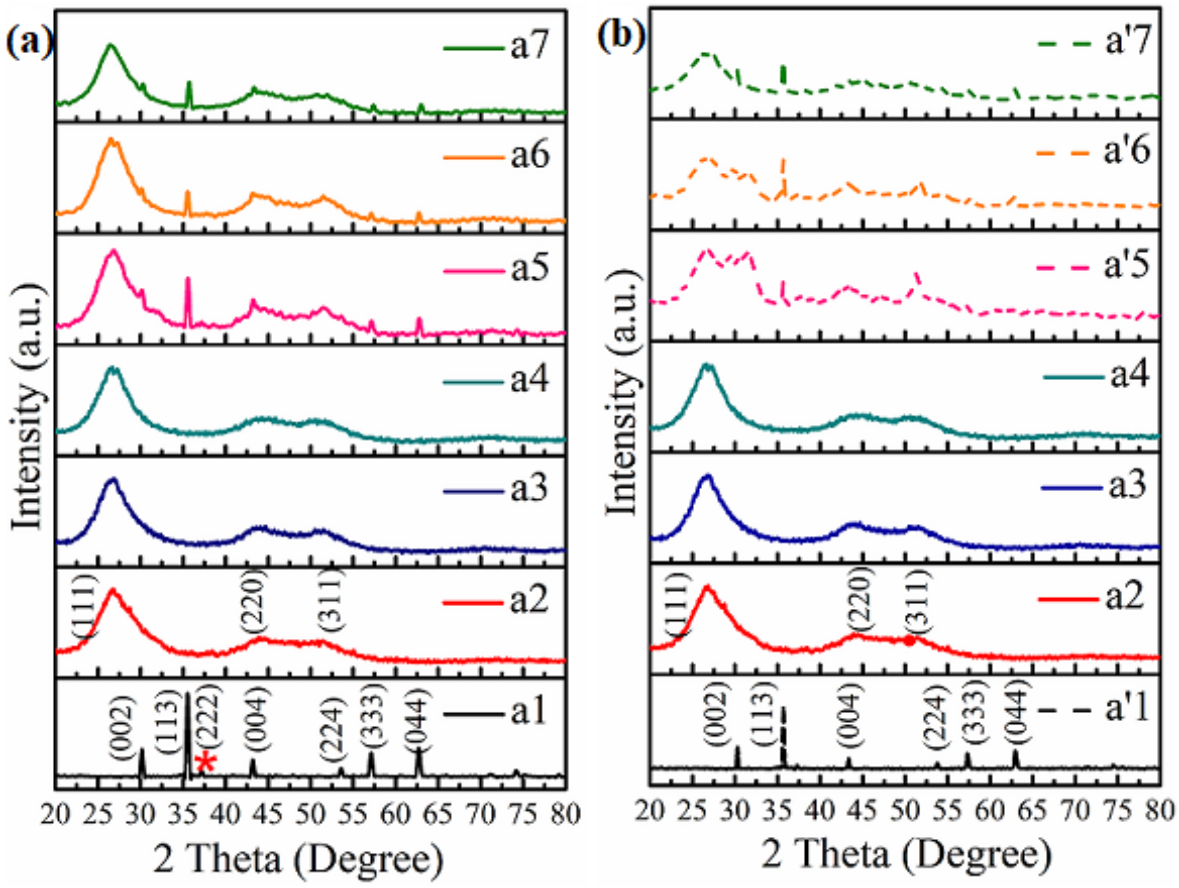

Figure 3.2: (a) and **(b)** Shows the XRD spectra of nanostructures

The following are the labels that were used to discuss the samples:

(a1: a'1): XRD spectra of NZF core annealed at 900°C and 1100°C respectively

(a2, a3 and a4): XRD spectra of CdS QDs shell (CdS1, CdS2 and CdS4 respectively formed with 1ml, 2ml and 4ml 2-ME)

(a5: a'5): XRD spectra for CSNs with 0.2 g NZF loading and CdS2 shell, NZF is annealed at 900°C and 1100°C respectively

(a6: a'6): XRD spectra for CSNs with 0.1 g NZF loading and CdS2 shell, NZF is annealed at 900°C and 1100°C respectively

(a7: a'7): XRD spectra for CSNs with 0.05g NZF loading and CdS2 shell, NZF is annealed at 900°C and 1100°C respectively

Table 3.1: Structural parameters for NZF (900°C and 1100°C), CdS1, CdS2, CdS4 QDs, and their core-shell structures

Sample name	2θ Position	(hkl)	Size from XRD (nm)
a1	30.18/35.53/37.17/43.18/53.59/57.12/62.73	022/113/222/004/224/333/044	26.96
a2	26.85/44.29/51.01	111/220/311	1.83
a3	26.79/44.41/51.45	111/220/311	1.59
a4	26.75/44.21/51.22	111/220/311	1.46
a5	26.72/31.68/35.57/43.51/51.55/57.32/62.90	101/022/113/110/112/333/044	-
a6	26.84/31.68/35.66/43.53/51.69/57.34/62.94	101/022/113/110/112/333/044	-
a7	26.33/31.78/35.16/43.52/51.69/57.34/62.52	101/022/113/110/112/333/044	-
a'1	30.24/35.67/37.22/43.18/53.81/57.18/63.13	022/113/222/004/224/333/044	23.75
a'5	26.28/30.24/35.60/43.29/51.46/57.29/62.88	101/022/113/110/112/333/044	-
a'6	26.51/30.19/35.80/43.37/50.73/57.26/63.01	101/022/113/110/112/333/044	-
a'7	26.29/30.83/35.81/43.37/50.56/57.26/63.16	101/022/113/110/112/333/044	-

3.3.2 Rietveld refinement

By employing "Full Prof software", "Rietveld refinement" of XRD spectra have been performed. The refined graphs for the selected samples are shown in Figure 3.3. The relevant computed profiles (represented by a solid black curve) and the discrepancy between the observed and calculated profiles (shown by a coloured line) are displayed in Figure 3.3. For all the selected set of samples the experimental and calculated profiles are well matched. The "goodness of fit" value for all of the samples was calculated to be near about 1, indicating that the graphs were well fitted. Table 3.2 lists the parameters calculated using Rietveld refinement.

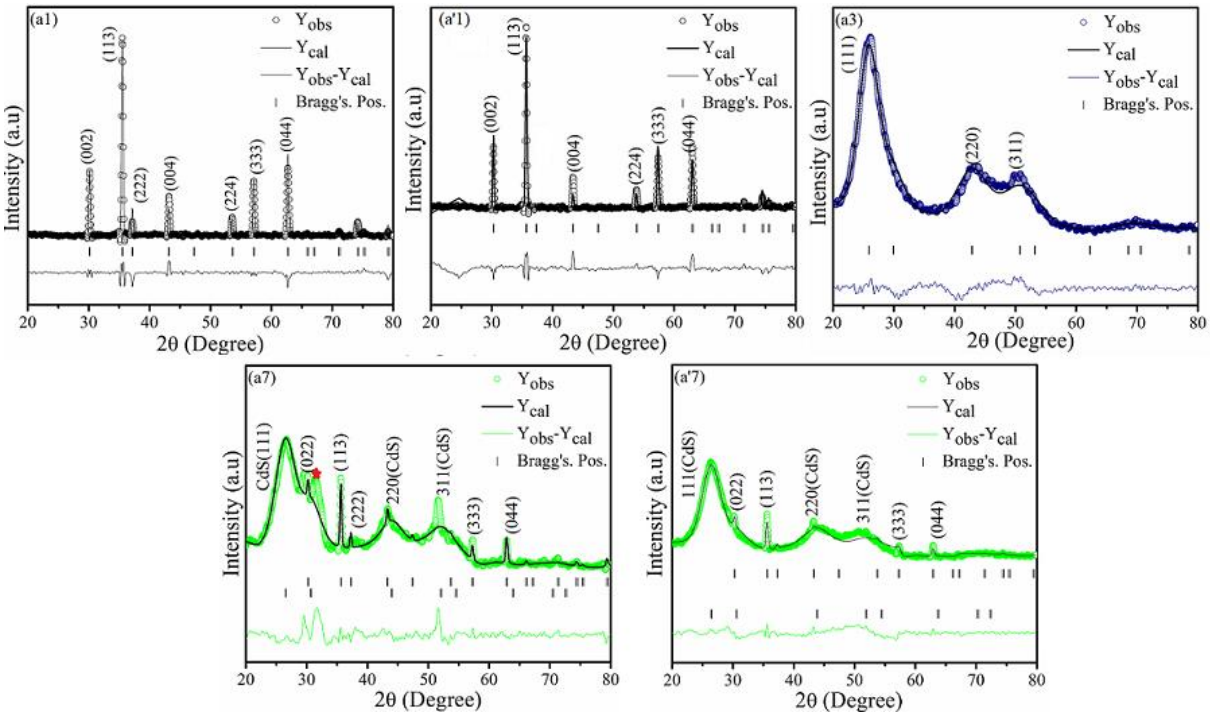

Figure 3.3: Rietveld refined spectra of synthesized nanostructures

The following are the labels that were used to discuss the samples:

(a1: a'1): Rietveld refined spectra for NZF core annealed at 900°C and 1100°C respectively

(a3): Rietveld refined spectra for CdS2 QDs shell (formed with2ml of 2-ME) and

(a7: a'7): Rietveld refined spectra for CSNs with NZF loading of 0.05 g and CdS2 shell, where NZF is annealed at 900°C and 1100°C respectively

Table 3.2: Summary of various parameters calculated using Rietveld refinement

Composition		Lattice Parameter a (Å)	Cell Volume V (A^3)	Phase Fraction (%)	R_B	R_F	G OF	χ^2
a3 (CdS2) (SG: *F-43m*)		5.9	212.4	100	3.6	3.1	1.1	1.4
a1(SG: *F-43m*)		8.3	588.2	100	4.3	3.7	1.4	1.6
a'1 (SG: *F-43m*)		8.3	581.5	100	3.9	3.4	1.3	1.5
a7	CdS	5.8	199.2	95.6	6.3	4.5	1.8	2.3
	NZF	8.3	583.8	4.3				
a'7	CdS	5.8	197.5	94.7	4.8	3.2	1.3	1.6
	NZF	8.3	583.9	5.2				

3.3.3 Transmission Electron Microscopy

The spherical shape of the generated core-shell nanostructures is confirmed by TEM investigation. Figure 3.4 shows micrographs of the minimal core composition with CdS2 shell. Core-shell nanostructures are shown by black colored core surrounded by grayish shell. One micrograph (a) shows a CSNs with the core annealed at 900°C, while the other (b) shows CSNs with the core annealed at 1100 °C.

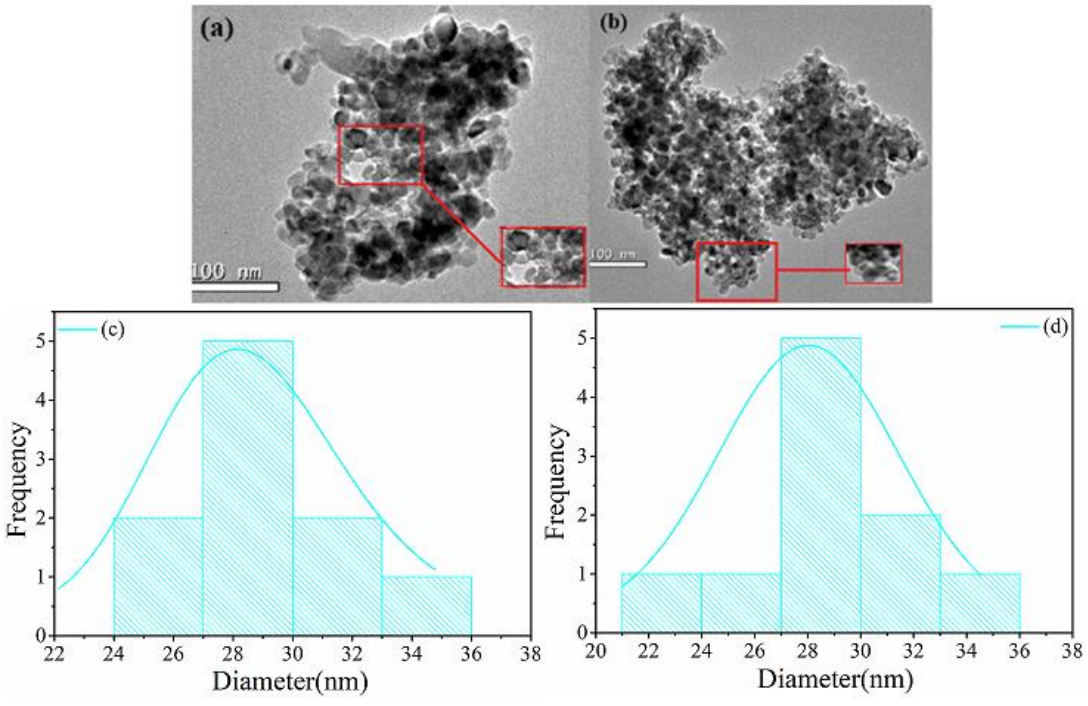

Figure 3.4: (a, b) TEM images for the CSNs with NZF loading of 0.05 g and CdS2 shell where, NZF is being annealed at 900°C and 1100°C respectively. **(c: d)** shows the histograms for the respective samples

Particle size obtained from TEM are presented in histogram plot figure 3.4 (a, b).

3.3.4 Energy dispersive X-ray spectra

The elemental composition of NZF/CdS CSNs was confirmed using "EDX spectra", and the effect of varied core annealing temperatures on the CSNs characteristics was evaluated using EDX spectra. EDX validated the atomic percentage for the CSNs generated with intermediate core loading and a CdS2 shell with the core annealed at two temperatures. The results show that CSNs prepared with 900°C (Fig. 3.5(a)) annealed NZF are out of stoichiometry, but CSNs prepared with 1100°C (Fig. 3.5(b)) annealed NZF have all of the elements in the predicted compositional ratio. Excess oxygen is available due to the existence of oxygen in the compound's formula and in the atmosphere during characterization. The creation of ZnS in a 900°C annealed core as compared to a 1100°C annealed core resulted in a decrease in Sulphur content, as indicated by the XRD and PL data. Elemental atomic percentage of different elements in the CSNs are inscribed in table 3.3.

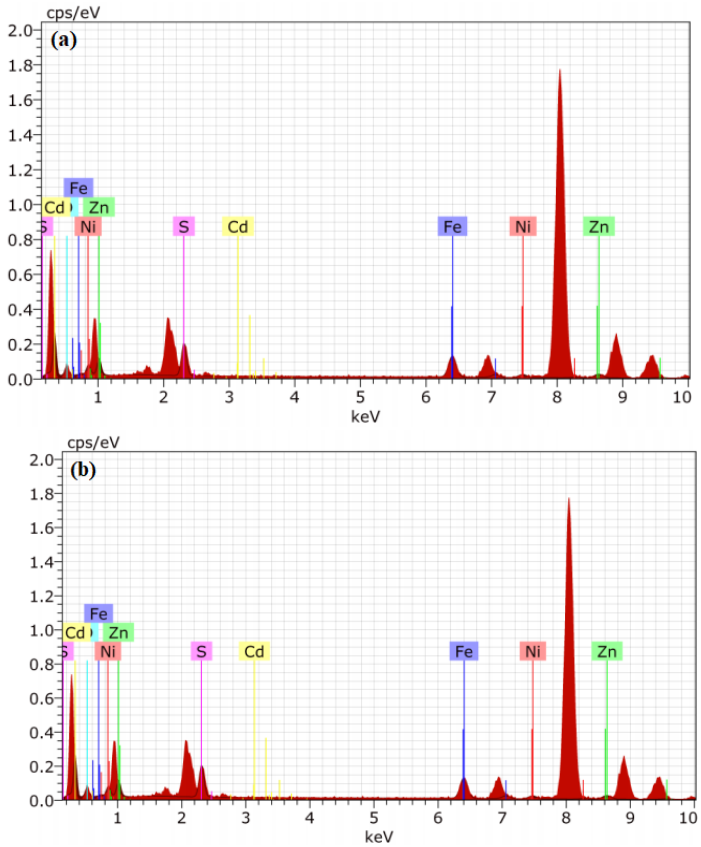

Figure 3.5: (a, b) shows the EDX spectra for the CSNs with NZF loading of 0.05 g and CdS2 shell where, NZF is being annealed at 900°C and 1100°C respectively

Table 3.3: Elemental atomic percentage of different elements in the CSNs

ATOMIC PERCENTAGE (%)			
S. No.	**Elements**	**Sample (a)**	**Sample (b)**
1.	**Fe**	0.55	0.41
2.	**Ni**	0.13	0.10
3.	**Zn**	0.10	0.06
4.	**O**	1.00	1.00
5.	**Cd**	1.00	0.83
6.	**S**	0.85	1.00

3.3.5 Optical studies

3.3.5.1 Absorbance spectroscopy

To analyse the optical behaviour of produced samples, "UV-vis spectra" for NZF, CdS QDs, and their CSNs were recorded. Figure 3.5 shows the absorbance bands for various samples. The band edge absorption of CdS QDs can be seen in all of the figures at 429.60 nm. The "absorbance spectra" of NZF produced are shown in Figure 3.6 (d &d'), and the graph clearly shows no absorption in the range of 380–800nm, which is the range of interest when talking of "magneto-fluorescent structures".

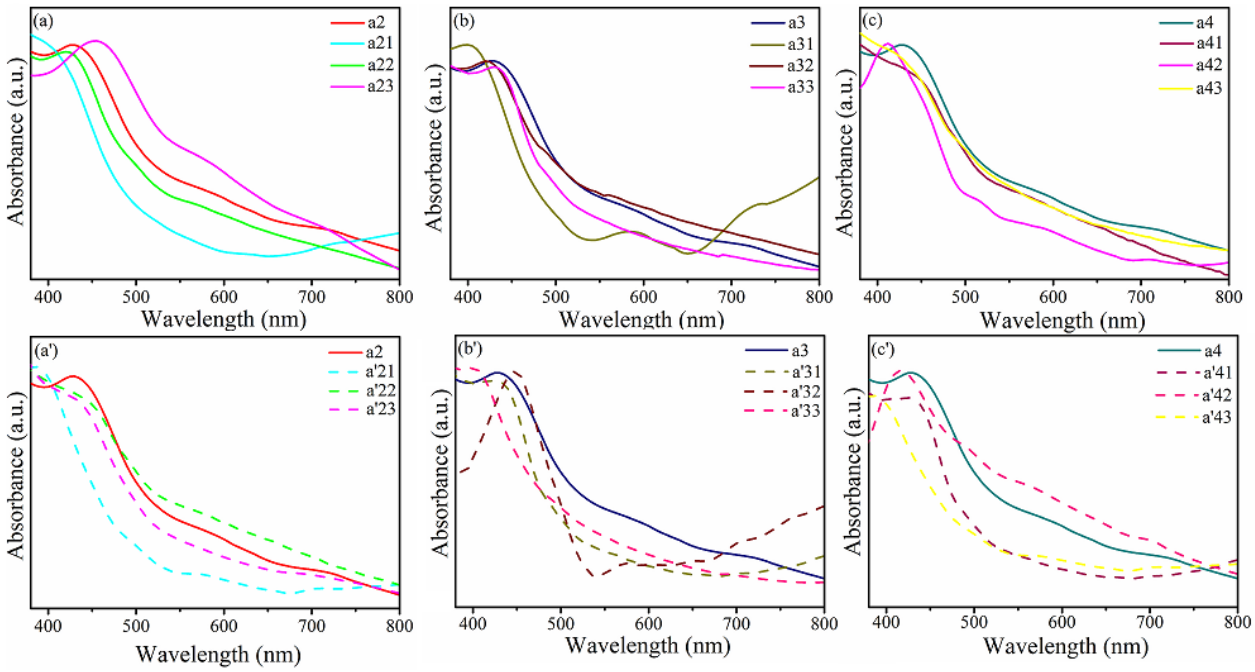

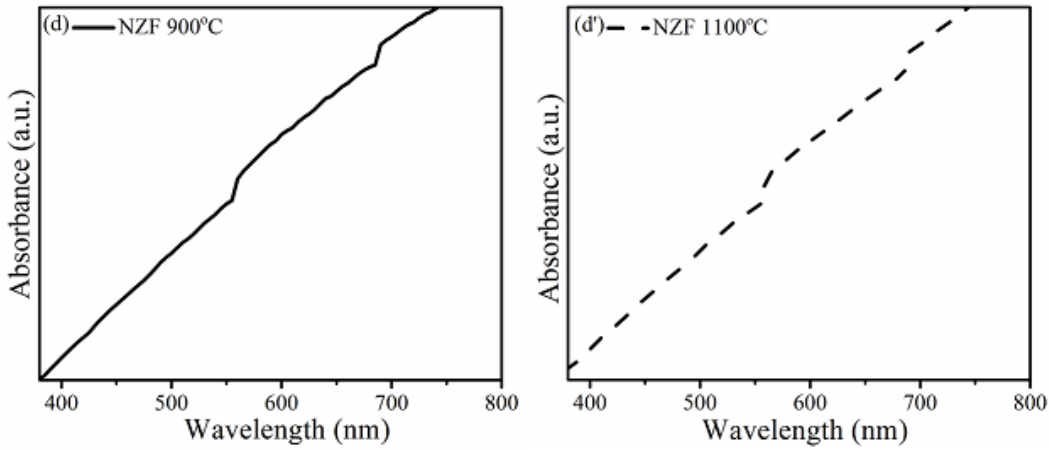

Figure 3.6: UV- vis spectra for prepared nanostructures

The following are the labels that were used to discuss the samples:

Figure (a: a'): UV-vis spectra of CdS1 shell and CSNs of CdS1 with diverse loading of NZF annealed at 900°C and 1100°C respectively

Graph (a2): UV-vis spectra of CdS1 QDs shell (CdS1 formed with 1ml 2-ME)

Graph (a21: a'21): UV-vis spectra of CSNs; 0.2 g NZF loading and CdS1 shell

Graph (a22: a'22): UV-vis spectra of CSNs; 0.1 g NZF loading and CdS1 shell

Graph (a23: a'23): UV-vis spectra of CSNs; 0.05 g NZF loading and CdS1 shell

Figure (b: b'): UV-vis spectra for CdS2 shell and CSNs of CdS2 with different loading of NZF annealed at 900°C and 1100°C respectively

Graph(a3): UV-vis spectra of CdS2 QDs shell (CdS2 formed with 2ml 2-ME)

Graph (a31: a'31): UV-vis spectra of CSNs; 0.2 g NZF loading and CdS2 shell

Graph (a32: a'32): UV-vis spectra of CSNs; 0.1 g NZF loading and CdS2 shell

Graph (a33: a'33): UV-vis spectra of CSNs; 0.05 g NZF loading and CdS2 shell

Figure (c: c'): UV-vis spectra of CdS4 shell and CSNs of CdS4 with different loading of NZF core annealed at 900°C and 1100°C respectively

Graph (a4): UV-vis spectra of CdS4 QDs shell (CdS4 formed with4ml 2-ME)

Graph (a41: a'41): UV-vis spectra of CSNs; 0.2 g NZF loading and CdS4 shell

Graph (a42: a'42): UV-vis spectra of CSNs; 0.1 g NZF loading and CdS4 shell

Graph (a43: a'43): UV-vis spectra of CSNs; 0.05 g NZF loading and CdS4 shell

Figure (d: d'): UV-vis spectra of NZF annealed at 900°C and 1100°C respectively

A modest shift is detected in absorption maxima when we switch from bare shell to the CSNs with various NZF loadings. "The absorption edge fluctuation was caused by the introduction of synergistic effects of low absorption ferrite nanoparticles and high absorption CdS QDs." In the case of CSNs NZF was annealed at 900 °C, the maximum NZF loading (0.2 g) displays a shift in absorption toward blue side of wavelength indicating a decrease in shell particle size on formation of NZF core over the shell. As a result, the blue-shifted absorbance

profiles of core-shell with NZF annealed at 900°C and 1100°C clearly demonstrated the influence of increased strain.

3.3.5.1.1 Derivative study of absorbance

We estimated the precise absorbance positions for samples by utilising the 2nd order derivative of absorbance for each sample. 2nd order derivative for bare CdS QDs, NZF, and their CSNs is revealed in Figure 3.7. Three peaks can be seen in each case of the double derivative graphs, indicating that the bands detected are equal to derivative order plus one, which is strong evidence of second order derivation.

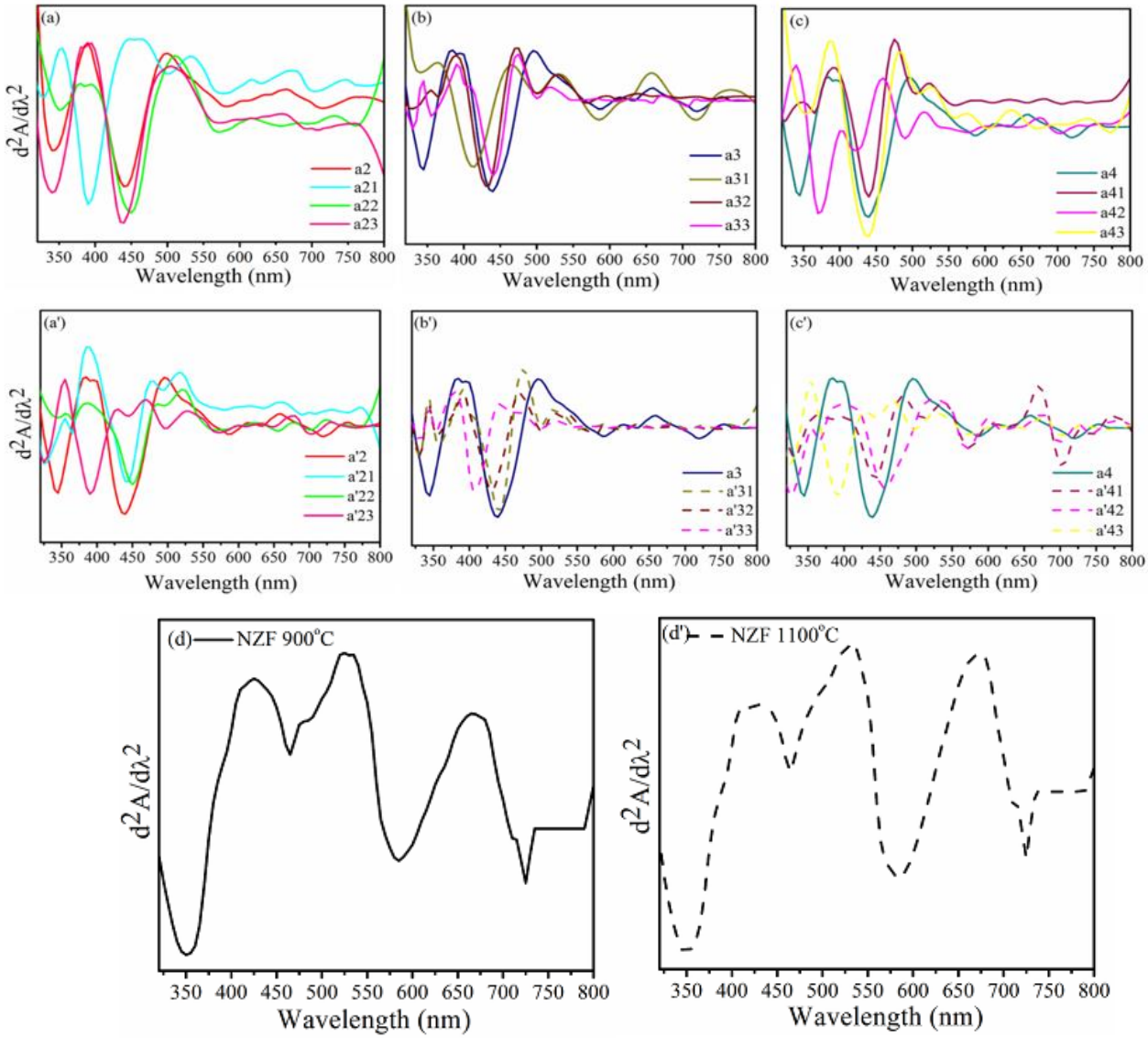

Figure 3.7: Derivative of UV-vis spectra for prepared nanostructures

The following are the labels that were used to discuss the samples:

Figure (a: a'): Derivative spectra of CdS1 shell and CSNs of CdS1 with diverse loading of NZF annealed at 900°C and 1100°C respectively

Graph (a2): Derivative spectra of CdS1 QDs shell (CdS1 formed with 1ml 2-ME)

Graph (a21: a'21): Derivative spectra of CSNs; 0.2 g NZF loading and CdS1 shell

Graph (a22: a'22): Derivative spectra of CSNs; 0.1 g NZF loading and CdS1 shell

Graph (a23: a'23): Derivative spectra of CSNs; 0.05 g NZF loading and CdS1 shell

Figure (b: b'): Derivative spectra for CdS2 shell and CSNs of CdS2 with different loading of NZF annealed at 900°C and 1100°C respectively

Graph(a3): Derivative spectra of CdS2 QDs shell (CdS2 formed with 2ml 2-ME)

Graph (a31: a'31): Derivative spectra of CSNs; 0.2 g NZF loading and CdS2 shell

Graph (a32: a'32): Derivative spectra of CSNs; 0.1 g NZF loading and CdS2 shell

Graph (a33: a'33): Derivative spectra of CSNs; 0.05 g NZF loading and CdS2 shell

Figure (c: c'): Derivative spectra of CdS4 shell and CSNs of CdS4 with different loading of NZF core annealed at 900°C and 1100°C respectively

Graph (a4): Derivative spectra of CdS4 QDs shell (CdS4 formed with4ml 2-ME)

Graph (a41: a'41): Derivative spectra of CSNs; 0.2 g NZF loading and CdS4 shell

Graph (a42: a'42): Derivative spectra of CSNs; 0.1 g NZF loading and CdS4 shell

Graph (a43: a'43): Derivative spectra of CSNs; 0.05 g NZF loading and CdS4 shell

Figure (d: d'): Derivative spectra of NZF annealed at 900°C and 1100°C respectively

3.3.5.2 Photoluminescence spectroscopy

"PL spectra" of CdS QDs and NZF/CdS were recorded and displayed in Figure 3.8. With an excitation wavelength of 350 nm, the PL spectra of whole NZF/CdS, core-shell nanostructures, and CdS (1, 2 & 4) QDs were recorded. CSNs, which incorporates MNPs with CdS have less strong emission as that of CdS QDs which have a strong emission band in their fluorescence spectra. In CdS emission profile a high-intensity band was discovered at 489.2 nm due to "de-trapped charge carrier recombination" [17]. "A weak band at 535 nm was also discovered, which was attributed to recombination of trapped electrons and holes existing at surface defect sites" [18]. In CSNs with 0.2 g NZF (annealed at 900 °C) loading (Figure 3.8(a21, a31, & a41)) an intense peak at 410 nm was discovered. This ZnS signal could be due to the significant amount of Zn in $NiZnFe_2O_4$ reacting with the sulphur present in thiourea during the CdS QDs manufacturing process. The XRD study of core-shell nanostructures also reveals this ZnS peak. This clearly shows that $NiZnFe_2O_4$ annealed at 900 °C is not particularly stable, as the zinc in the ferrite reacts with the sulphur in CdS. As a result, $NiZnFe_2O_4$ annealed at 1100°C is significantly more stable than $NiZnFe_2O_4$ annealed at 900°C because there is no Zn leakage from $NiZnFe_2O_4$ to the CdS QDs shell. In the case of

minimum $NiZnFe_2O_4$ loading, improved luminous intensity and particle size dispersion were attained.

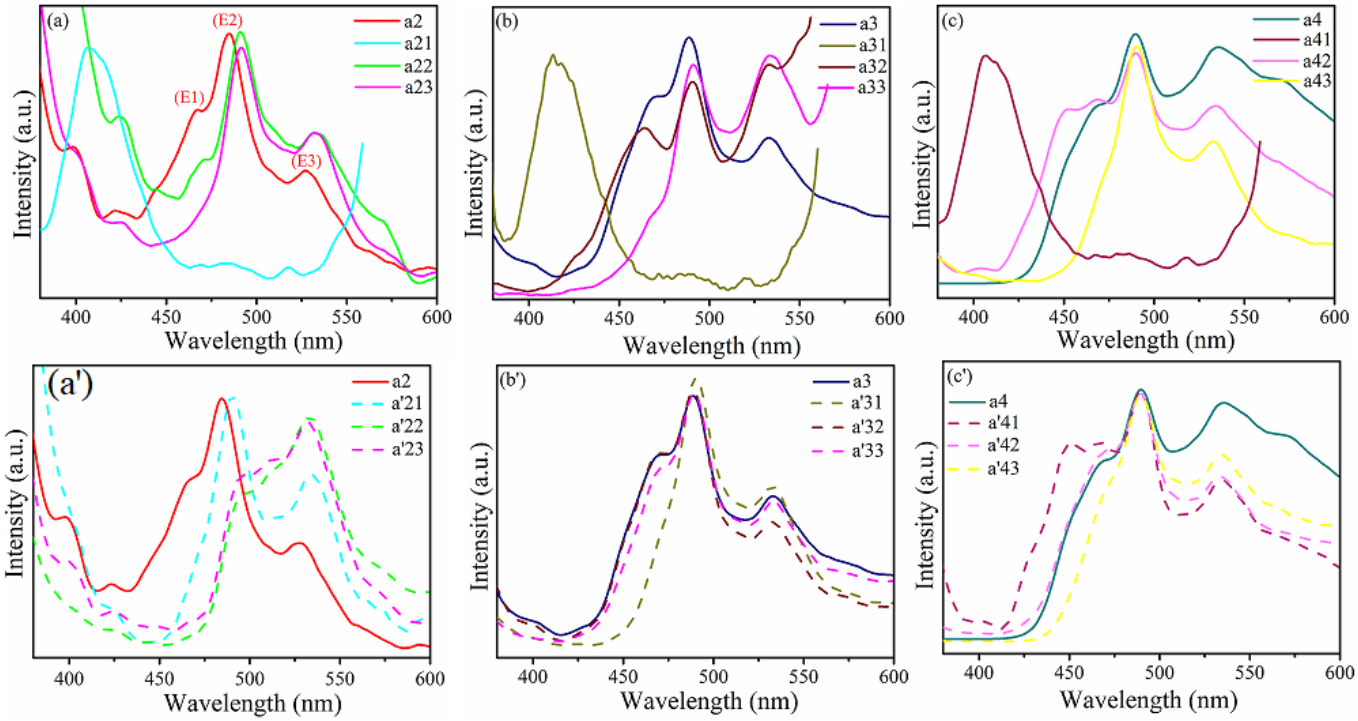

Figure 3.8: Photo luminescence spectra for prepared nanostructures with most prominent emission peaks being represented by E1, E2 and E3 in each profile

The following are the labels that were used to discuss the samples:

Figure (a: a'):PL spectra of CdS1 shell and CSNs of CdS1 with different loading of NZF core annealed at 900°C and 1100°C respectively

Graph (a2):PL spectra of CdS1 QDs shell (CdS1 formed with 1ml 2-ME)

Graph (a21: a'21): PL spectra of CSNs; 0.2 g NZF loading and CdS1shell

Graph (a22: a'22):PL spectra of CSNs; 0.1 g NZF loading and CdS1 shell

Graph (a23: a'23):PL spectra of CSNs; 0.05 g NZF loading and CdS1 shell

Figure (b: b'):PL spectra for CdS2 shell and CSNs of CdS2 with different loading of NZF core annealed at 900°C and 1100°C respectively

Graph(a3):PL spectra ofCdS2 QDs shell (CdS2 formed with 2ml 2-ME)

Graph (a31: a'31):PL spectra of CSNs; 0.2 g NZF loading and CdS2 shell

Graph (a32: a'32):PL spectra of CSNs; 0.1 g NZF loading and CdS2 shell

Graph (a33: a'33):PL spectra of CSNs; 0.05 g NZF loading and CdS2 shell

Figure (c: c'):PL spectra ofCdS4 shell and CSNs of CdS4 with different loading of NZF core annealed at 900°C and 1100°C respectively

Graph (a4):PL spectra ofCdS4 QDs shell (CdS4 formed with4ml 2-ME)

Graph (a41: a'41): PL spectra of CSNs; 0.2 g NZF loading and CdS4 shell

Graph (a42: a'42): PL spectra of CSNs; 0.1 g NZF loading and CdS4 shell

Graph (a43: a'43): PL spectra of CSNs; 0.05 g NZF loading and CdS4 shell

3.3.5.2.1 Derivative study of photoluminescence spectra

The derivative method has made it possible to discuss some of the aspects that were previously invisible or repressed in PL spectra (DSM). When comparing core-shell nanostructures to bare CdS (1, 2 & 4) QDs, derivative method allows us to obtain all of the miniscule marks on the peak shift and defect positions, regardless of how slight the shift is. Figure 3.9 depicts the core-shell nanostructures' double derivative curve. We are receiving good luminescence qualities that are similar to the spectra of CdS QDs. The overview of various parameters calculated by PL spectroscopy for the shell and core-shell are shown in Table 3.4.

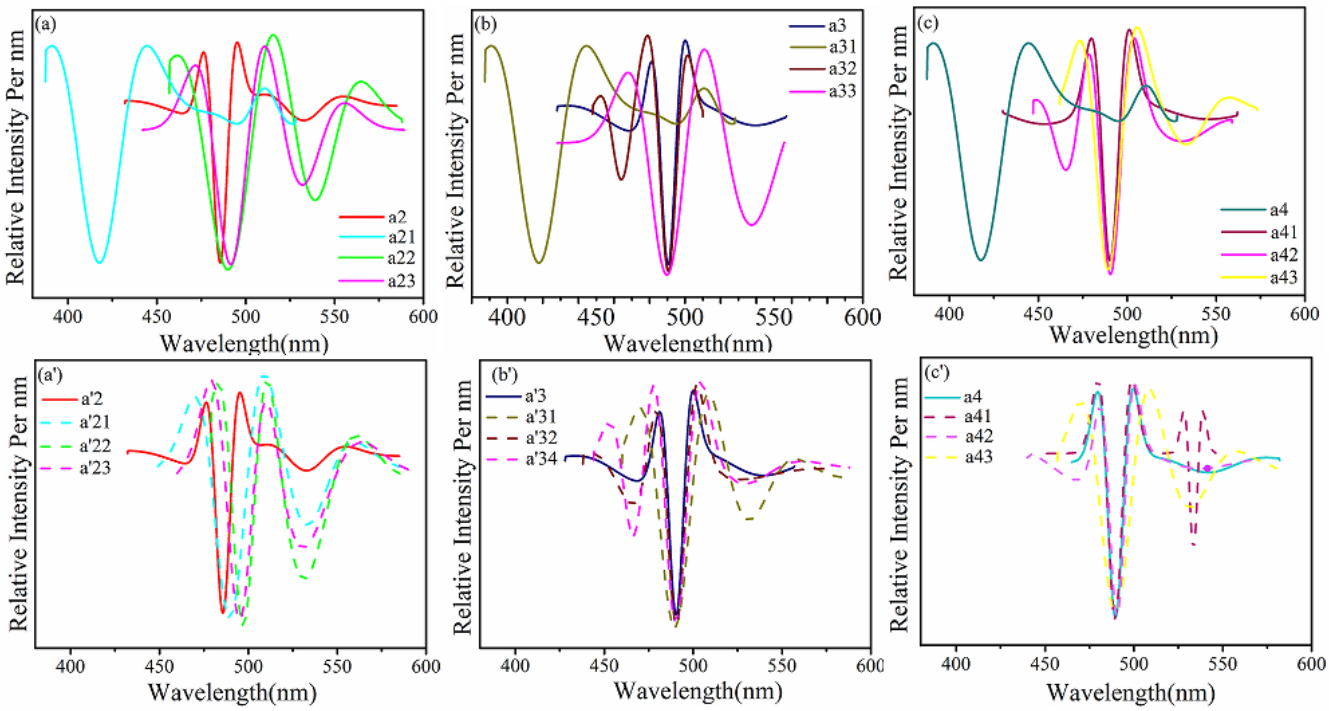

Figure 3.9: Derivative of photo luminescence spectra for prepared nanostructures

The following are the labels that were used to discuss the samples:

Figure (a: a'): PL derivative spectra of CdS1 shell and CSNs of CdS1 with different loading of NZF core annealed at 900°C and 1100°C respectively

Graph (a2): PL derivative spectra of CdS1 QDs shell (CdS1 formed with 1ml 2-ME)

Graph (a21: a'21): PL derivative spectra of CSNs; 0.2 g NZF loading and CdS1shell

Graph (a22: a'22): PL derivative spectra of CSNs; 0.1 g NZF loading and CdS1 shell

Graph (a23: a'23): PL derivative spectra of CSNs; 0.05 g NZF loading and CdS1 shell

Figure (b: b'):PL derivative spectra for CdS2 shell and CSNs of CdS2 with different loading of NZF core annealed at 900ºC and 1100ºC respectively

Graph(a3):PL derivative spectra ofCdS2 QDs shell (CdS2 formed with 2ml 2-ME)

Graph (a31: a'31):PL derivative spectra of CSNs; 0.2 g NZF loading and CdS2 shell

Graph (a32: a'32):PL derivative spectra of CSNs; 0.1 g NZF loading and CdS2 shell

Graph (a33: a'33):PL derivative spectra of CSNs; 0.05 g NZF loading and CdS2 shell

Figure (c: c'):PL derivative spectra ofCdS4 shell and CSNs of CdS4 with different loading of NZF core annealed at 900ºC and 1100ºC respectively

Graph (a4): PL derivative spectra ofCdS4 QDs shell (CdS4 formed with4ml 2-ME)

Graph (a41: a'41): PL derivative spectra of CSNs; 0.2 g NZF loading and CdS4 shell

Graph (a42: a'42): PL derivative spectra of CSNs; 0.1 g NZF loading and CdS4 shell

Graph (a43: a'43): PL derivative spectra of CSNs; 0.05 g NZF loading and CdS4 shell

Table 3.4: Summary of various parameters calculated by the PL spectroscopy for the CdS and $NiZnFe_2O_4$/CdS.

S. No	Sample name	Peak positions (nm)			Intensities (a.u.)		
		E_1	E_2	E_3	I_1	I_2	I_3
1.	a2	466.2	484.3	535.5	184.7	222.0	171.0
2.	a21/a'21	410.02/--	--/**490.30**	--/**534.74**	220/-	--/**221**	--/**158.04**
3.	a22/a'22	470.18/--	491.78/**497.32**	533.16/**533.51**	166.1/**182.4**	202.1/**212.2**	100.02/**98**
4.	a23/a'23	--	490.99/**495.58**	532.05/**532.28**	--	214/**201**	164/**170**
5.	a3	469.10	488.65	532.71	175	214	164
6.	a31/a'31	413.64/-	-/**490.30**	-/**532.71**	163.23/--	-/**90.2**	-/**63.23**
7.	a32/a'32	464.4/**470.32**	490.05/**489.08**	532.30/**532.71**	171.2/**165.32**	210.5/**212.23**	89/**76**
8.	a33/a'33	468.92/**471.82**	490.95/**489.08**	533.78/**533.13**	163.23/**163.24**	209.23/**208.44**	150.21/**156.36**
9.	a4	468.18	488.69	534.24	180.2	224.4	176.32
10.	a41/a'41	413.71/**449.61**	--/**489.85**	--/**533.93**	163.02/**162.23**	--/**212.32**	--/**159.02**
11.	a42/a'42	468.63/**470.32**	488.24/**489.08**	532.23/**534.36**	172.01/**170.5**	220.23/**256.12**	156.3/**155.23**
12.	a43/a'43	-	490.50/**489.45**	532.88/**533.93**	-	226.23/**232**	155.08/**151.96**

3.3.6 Magnetic Studies

Magnetic studies of NZF annealed at (900°C & 1100°C) and NZF/CdS CSNs have been observed. Hysteresis loop for the respective samples is shown in Figure 3.10; however, because shell CdS QDs are entirely diamagnetic, no VSM analysis was required. The decrease in saturation magnetization with increasing annealing temperature of core occurred because of ion diffusion and the creation of pores at higher temperature. Thus causing, domain wall movement to be difficult, which could explain why magnetization was reduced. The saturation magnetization of samples has decreased as a result of the development of pores at higher annealing temperatures [19].

On developing magnetically departed CdS layer upon NZF, saturation magnetization was deteriorated on switching from NZF to NZF/CdS. Furthermore, core-shell structures made of NZF annealed at 1100 °C are more stable and show superior appropriateness in terms of stability in both physical and chemical terms.

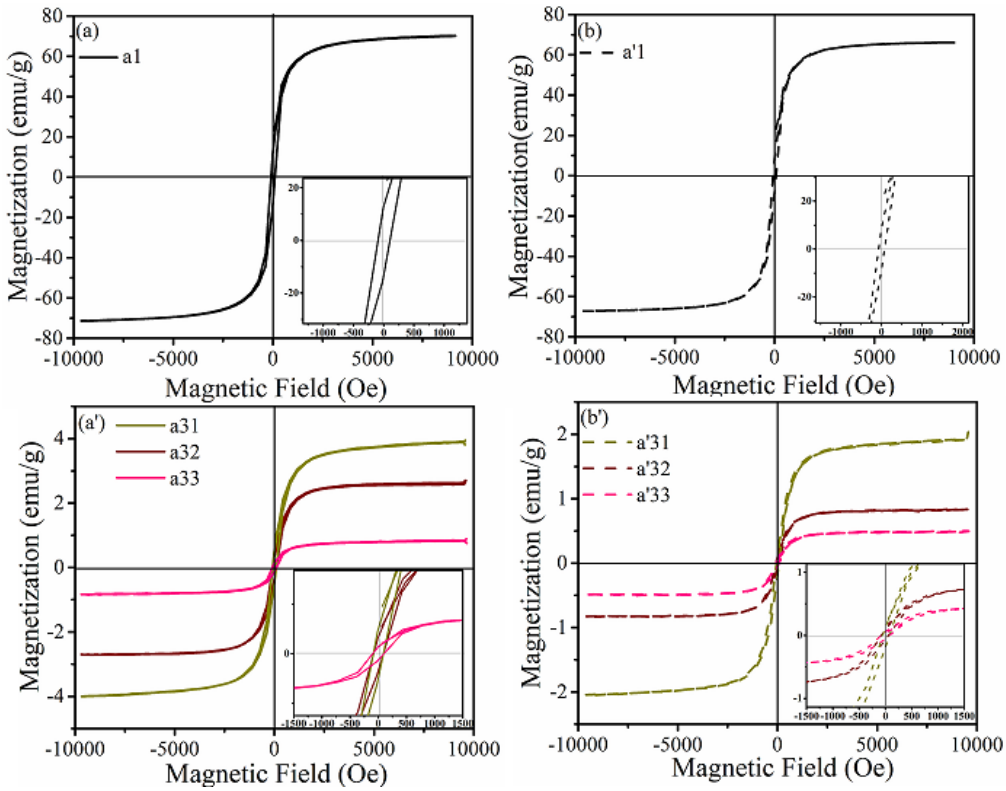

Figure 3.10: Hysteresis curve for the core and CSNs

The following are the labels that were used to discuss the samples:

(a1: a'1): Hysteresis curve of NZF core annealed at 900°C and 1100°C respectively

(a31: a'31): Hysteresis curve of CSNs; 0.2 g NZF loading and CdS2 shell

(a32: a'32): Hysteresis curve of CSNs; 0.1 g NZF loading and CdS2 shell

(a33: a'33): Hysteresis curve of CSNs; 0.05 g NZF loading and CdS2 shell

Insets show the zoomed images of the respective curves.

Table 3.5: Magnetic parameters of ferrite (900°C and 1100°C), and their CSN

S. No	Sample	M_s(emu/g)	M_r(emu/g)	H_c (Oe)	M_r/M_s	K (erg/cm^3)	SFD
1.	a1	70.16	13.04	98.98	0.18	3472.21	2.63
2.	a'1	66.35	6.45	73.16	0.09	2427.08	2.58
3.	a31	4.03	0.45	76.75	0.11	154.65	1.62
4.	a32	2.64	0.34	89.31	0.12	117.88	1.69
5.	a33	0.82	0.19	78.20	0.23	32.06	1.58
6.	a'31	1.97	0.18	68.05	0.09	67.02	1.63
7.	a'32	0.82	2.84	100.39	3.46	41.15	1.58
8.	a'33	0.48	0.056	80.15	0.10	19.23	1.56

3.3.6.1 Derivative study of hysteresis curve

Magnetic field versus susceptibility curve generated from normal B-H curves through derivative of susceptibility is shown in Figure 3.10. It shows the fluctuation in magnetic susceptibility for different core-shell configurations with varied core loading in retort to the applied magnetic field. Table 3.5 shows the SFD computed from the magnetic susceptibility curve. The SFD value tells us about the particle size distribution inside the structure. [20-21].

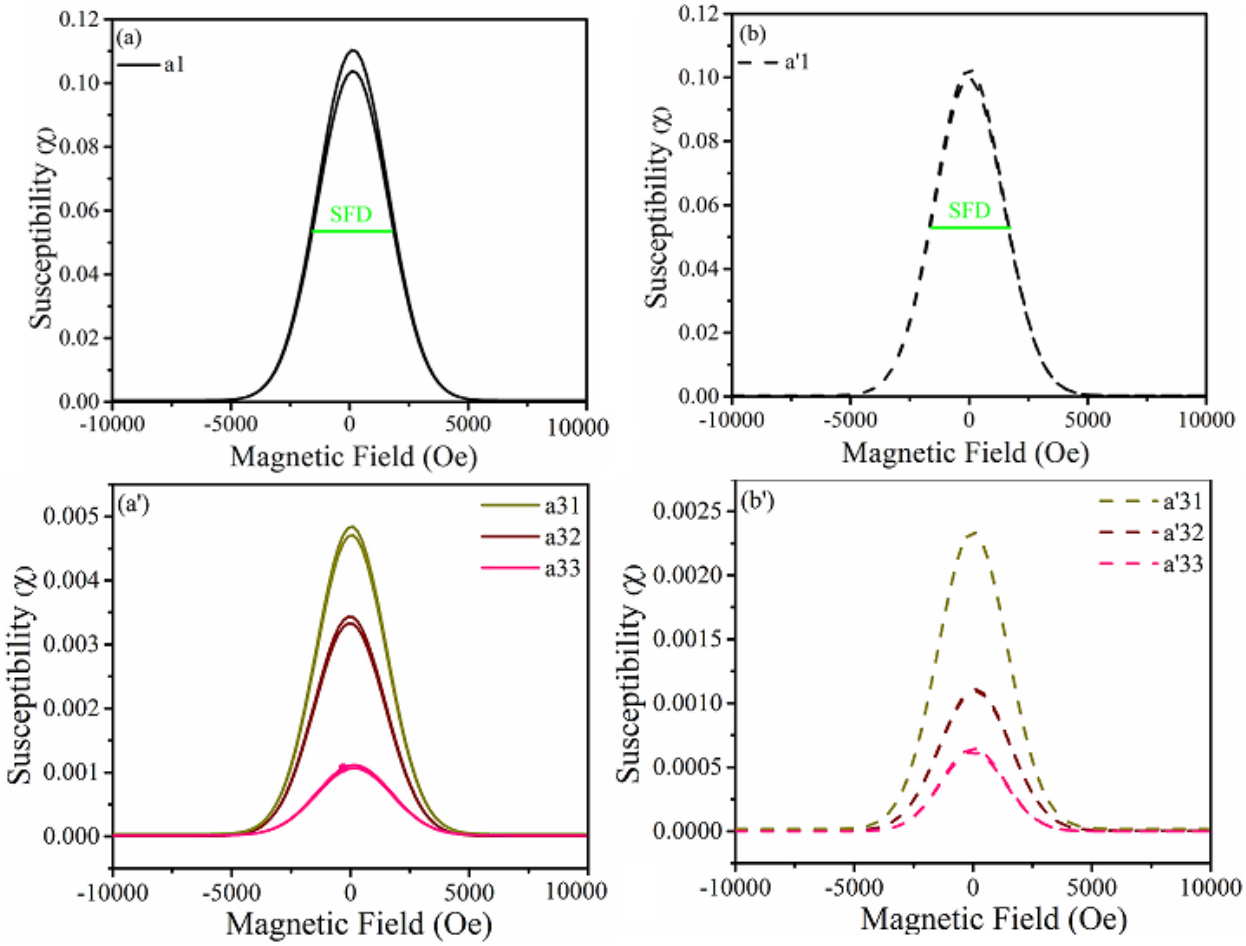

Figure 3.11: 1st order derivative hysteresis curve for the NZF and CSNs

The following labels were used to explain the samples:

(a1: a'1): 1st order derivative hysteresis curve for NZF core annealed at 900°C and 1100°C respectively

(a31: a'31): 1st order derivative hysteresis curve for CSNs; 0.2 g NZF loading and CdS2 shell

(a32: a'32): 1st order derivative of hysteresis for CSNs; 0.1 g NZF loading and CdS2 shell

(a33: a'33): 1st order derivative of hysteresis for CSNs; 0.05 g NZF loading and CdS2 shell

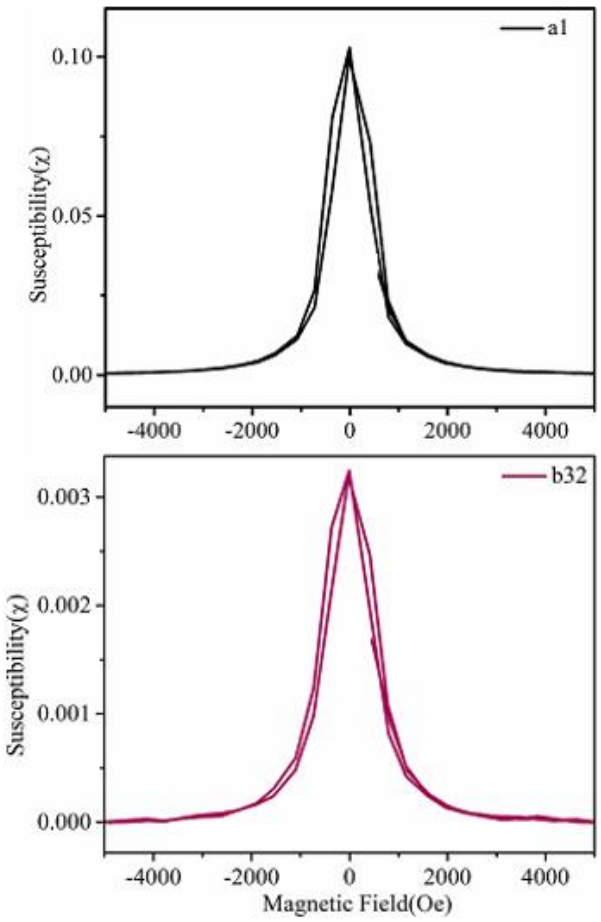

Figure 3.12: Shows the zoomed derivative curves of hysteresis loop for prepared nanostructures. (a1) bare NZF and (b32) core-shell; NZF loading of 0.1 g and shell of CdS2

3.3.7 FT-IR Studies

The FTIR was used to identify constituents, the number of components and sample fineness or uniformity. The spectra of NZF, CdS QDs, and NZF/CdS are shown in Figure 3.11. FTIR spectra in the region of 4000-400 cm^{-1} were used to inspect all the set of samples. In general, spinel ferrites have two wide oxygen metal bands in their FTIR spectra, which are also present in our samples. As a result, the one detected at v1=606 cm^{-1} corresponds to the metal ion's inherent stretching vibration at the "tetrahedral site," whilst the lowest band, observed around v2=460 cm^{-1}, is assigned to "octahedral" metal stretching vibration. [22]. “The band near 3388 cm^{-1} corresponds to H_2O's O–H stretching vibration; the particular absorption peak at 2339 cm^{-1} relates to citric acid's O–H group; the band at 1450 cm^{-1} corresponds to antisymmetric NO_3 stretching vibrations; and the band at 1647 cm^{-1} corresponds to carbo-oxalate anions.

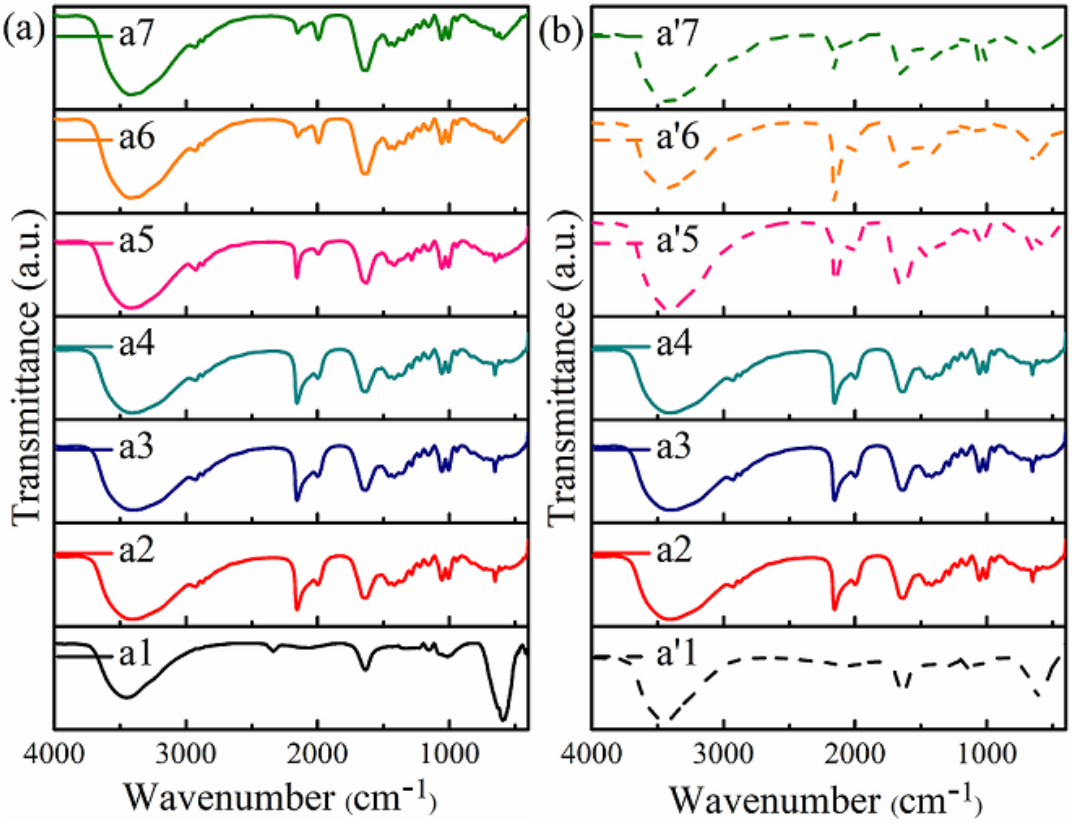

Figure 3.13: (a and b) are FTIR spectra for NZF, CdS QDs and their CSNs where NZF annealed at 900°C and 1100°C respectively

The following labels were used to explain the samples:

(a1: a'1): FTIR spectra of NZF core annealed at 900°C and 1100°C respectively

(a2, a3 and a4): FTIR spectra of CdS (1, 2 & 4) respectively formed with 1ml, 2ml and 4ml 2-ME)

(a5: a'5): FTIR spectra of CSNs with 0.2g NZF core loading and CdS2 shell, with NZF annealed at 900°C and 1100°C respectively

(a6: a'6): FTIR spectra of CSNs with 0.1 g NZF core loading and CdS2 shell with NZF annealed at 900°C and 1100°C respectively

(a7: a'7): FTIR spectra of CSNs with 0.05 g NZF core loading and CdS2 shell with NZF annealed at 900°C and 1100°C respectively

The hydroxyl group is represented by the stretching vibration at 2352 cm^{-1}. C=C, C–H characteristic vibrations in CdS QDs samples were assigned to the broad peak at 2120 cm1, 1383 cm^{-1}, and the faint peak at 1614 cm^{-1}" in Figure [23]. "The stretching vibration of H_2O at 3418 cm^{-1} corresponds to the OH stretching vibration, while the hydroxyl group at 2352 cm^{-1} relates to the hydroxyl group" [24-25]. Table 3.5 summarises the functional groups for ferrite

(annealed at 900 and 1100 degrees Celsius), CdS1, CdS2, and CdS4 QDs, and their CSNs in the fingerprint area (400-1500 cm^{-1}).

Table 3.6: Summary of the functional groups for the ferrites (annealed at 900°C and 1100°C), CdS1, CdS2, CdS4 QDs, and their CSNs

Sample Name	Region (cm^{-1})	Intensity	Interpretation
CdS QDs	400-470	weak	Cd-S bond stretching (CdS nanoparticles)
	820-850	Sharp	S-S-S bending or C-H stretching
	1060-1120	Sharp	C-O or S-O
	1380-1420	Sharp and Broad	C-H bending of CH_3
$NiZnFe_2O_4$	430-470	Small and weak	Lattice vibration of metal at octahedral sites.
	550-580	Sharp and weak	Lattice vibration of metal ions at tetrahedral sites.
	429-588	Broad	Characteristic peaks correspond to the stretching vibration of metal-oxygen bond, indicating the formation of ferrite.
	619	Broad and sharp	Octahedral sites in T-S block boundaries
	934	Weak and small	Vibrational frequency of octahedral sites in S and T block of whole complex
	1001	Sharp and weak	C-O Stretching
	1446	Weak and small	N-O stretching
Core-shell	551	Small and weak	Bending vibration within the molecule
	765-996	weak	"Corresponds to Cd-S bond which approved the formation of CdS nanoparticles"
	1221-1419	Sharp	C–H bending of CH_3"

3.4 Conclusion

- The core-shell nanostructures of NZF/CdS efficaciously created using a "seed mediate growth method" that combines "sol-gel" and "solution growth methods".
- Structural and morphological characterizations demonstrate the well-defined phases and good crystalline quality of NZF core and CdS QDs shell.

- The shell was effectively attached to the core surface, and a strong bond was seen in all cases, especially in the CSNs with low ferrite loading.
- Optical experiments revealed that the nanostructures obtained covered a considerable percentage of the visible light spectrum, with the greatest results obtained with the least amount of core material loaded.
- The creation of ferromagnetic NZF/CdS nanostructures was discovered using VSM.
- On NZF/CdS nanostructures, spin-dependent experiments are carried out utilising the derivative of susceptibility. The CSNs generated has diffused boundaries when the maximum (0.2 g) quantity of core loading is applied and the annealing temperature of core ferrite is set to 900^{o}C. Both the core and the shell interact spin-to-spin at the interface. Magnetic analysis also demonstrates that when a semiconducting shell is organized over magnetic core, saturation value decreased, indicating towards the effective core-shell formation.
- According to FTIR research, the functional groups existing on the surface are favourable for further processing these "magneto-fluorescent nanostructures" for biological applications.
- These findings show that the "magneto-fluorescent nanostructures" could be employed in spintronics as well as medication administration, diagnostics, and imaging applications in nanomedicine.

3.5 REFERENCES

[1] Sharma, D., & Hussain, C. M. *Smart nanomaterials in pharmaceutical analysis.* Arabian Journal of Chemistry, vol. 13(1), pp. 3319-3343, Jan. 2020.

[2] Jeevanandam, J., Barhoum, A., Chan, Y. S., Dufresne, A., & Danquah, M. K. *Review on nanoparticles and nanostructured materials: history, sources, toxicity and regulations. Beilstein journal of nanotechnology*, vol. 9(1), pp. 1050-1074, Apr. 2018.

[3] W. G. Kreyling, M. Semmler-Behnke, and Q. Chaudhry, *"A complementary definition of nanomaterial,"* Nano Today, vol. 5(3), pp. 165–168, Sep. 2010.

[4] M. M. Bellah, S. M. Christensen, and S. M. Iqbal, *"Nanostructures for medical diagnostics,"* Journal of Nanomaterials, vol. (2012), 2012.

[5] M. Nasrollahzadeh, Z. Issaabadi, M. Sajjadi, S. M. Sajadi, and M. Atarod, *"Types of Nanostructures*," in Interface Science and Technology, pp. 29–80, 2019.

[6] Noah, N. M. *Design and synthesis of nanostructured materials for sensor applications*. Journal of Nanomaterials, Oct. *2020*.

[7] Huang, X., El-Sayed, I. H., Qian, W., & El-Sayed, M. A. *Cancer cell imaging and photothermal therapy in the near-infrared region by using gold nanorods.* Journal of the American Chemical Society, vol. 128(6), pp. 2115-2120, Feb. 2006.

[8] Jain, P. K., & El-Sayed, M. A. Universal scaling of plasmon coupling in metal nanostructures: extension from particle pairs to nanoshells. *Nano letters*, vol. 7(9), pp. 2854-2858, Sep. 2007.

[9] Galogahi, F. M., Zhu, Y., An, H., & Nguyen, N. T. *Core-shell microparticles: Generation approaches and applications*. Journal of Science: Advanced Materials and Devices, Sep. 2020.

[10] Zaiats, G., Yanover, D., Vaxenburg, R., Tilchin, J., Sashchiuk, A., & Lifshitz, E. *PbSe-based colloidal core/shell heterostructures for optoelectronic applications.* Materials, vol. 7(11), pp. 7243-7275, Nov.2014.

[11] Wehrenberg, B. L., Wang, C., & Guyot-Sionnest, P. (2002). *Interband and intraband optical studies of PbSe colloidal quantum dots*. The Journal of Physical Chemistry B, vol. 106(41), pp. 10634-10640, Oct. 2002.

[12] Du H., Chen C., Krishnan R., Krauss T.D., Harbold J.M., Wise F.W., Thomas M.G., Silcox J. *Optical properties of colloidal PbSe nanocrystals.* Nano Lett, pp. 1321–1324, 2002.

[13] Ali, A., Hira Zafar, M. Z., ul Haq, I., Phull, A. R., Ali, J. S., & Hussain, A. *Synthesis, characterization, applications, and challenges of iron oxide nanoparticles.* Nanotechnology, science and applications, vol. 9(49), 2016.

[14] Mirnajafizadeh, F., Ramsey, D., McAlpine, S., Wang, F., & Stride, J. A. *Nanoparticles for bioapplications: study of the cytotoxicity of water dispersible CdSe (S) and CdSe (S)/ZnO quantum dots.* Nanomaterials, vol. *9*(3), 465, Mar. 2019.

[15] Rawat, D., Barman, P. B., & Singh, R. R. *Multifunctional magneto-fluorescent NiZnFe@ CdS core-shell nanostructures for multimodal applications.* Materials Chemistry and Physics, vol. 231, pp. 388-396, Jun. 2019.

[16] Joseph, J., Mishra, N., Mehto, V. R., Banerjee, A., & Pandey, R. K. (2014). *Structural, optical and magnetic characterisation of bifunctional core shell nanostructure of Fe3O4/CdS synthesised using a room temperature aqueous route.* Journal of Experimental Nanoscience, vol. 9(8), pp. 807-817, Sep. 2014.

[17] Kumari, A., & Singh, R. R. *Encapsulation of highly confined CdSe quantum dots for defect free luminescence and improved stability*. Physica E: Low-dimensional Systems and Nanostructures, vol. 89, pp. 77-85, May. 2017.

[18] Roshima, N. S., Saravana Kumar, S., Maheswari, A. U., & Sivakumar, M. *Study on Vacancy Related Defects of CdS Nanoparticles by Heat Treatment*. In Journal of Nano Research Vol. 18, pp. 53-61, 2012.

[19] Sangeetha, A., Kumar, K. V., & Kumar, G. N. *Effect of annealing temperature on the structural and magnetic properties of NiFe 2 O 4 nanoferrites.* Advances in Materials Physics and Chemistry, vol. *7*(02), 2017.

[20] Lake Shore Cryotronics Inc. "Measuring Magnetic Media Using a VSM". AZoM. https://www.azom.com/article.aspx?ArticleID=4959. 2020.

[21] D. Neupane, M. Ghimire, H. Adhikari, A. Lisfi, S. R. Mishra, *Synthesis and magnetic study of magnetically hard-soft SrFe12-yAlyO19-x Wt.% Ni0. 5Zn0. 5Fe2O4 nanocomposites,* AIP Adv, vol. 7(2017), pp.055602, 2017.

[22] Waldron, R. D. *Infrared spectra of ferrites.* Physical review, vol. *99*(6), pp. 1727, Sep. 1995.

[23] De, M., Mukherjee, A., & Tewari, H. S. *Characterization of cadmium substituted nickel ferrites prepared using auto-combustion technique*. Processing and Application of Ceramics, vol. *9*(4), pp. 193-197, 2015.

[24] Nejati, K., & Zabihi, R. *Preparation and magnetic properties of nano size nickel ferrite particles using hydrothermal method.* Chemistry Central Journal, vol. *6*(1), pp. 1-6, Dec. 2012.

[25] Mahdavi, M., Ahmad, M. B., Haron, M. J., Namvar, F., Nadi, B., Rahman, M. Z. A., & Amin, J. *Synthesis, surface modification and characterisation of biocompatible magnetic iron oxide nanoparticles for biomedical applications.* Molecules, vol. 18(7), pp. 7533-7548, Jul. 2013.

CHAPTER- 4

SYNTHESIS AND CHARACTERIZATION OF STRONTIUM HEXAFERRITE ($SrFe_{12}O_{19}$), CADMIUM SULPHIDE (CdS) QUANTUM DOTS AND THEIR CORE/SHELL NANOSTRUCTURES FOR MAGNETIC CELL SORTING APPLICATIONS

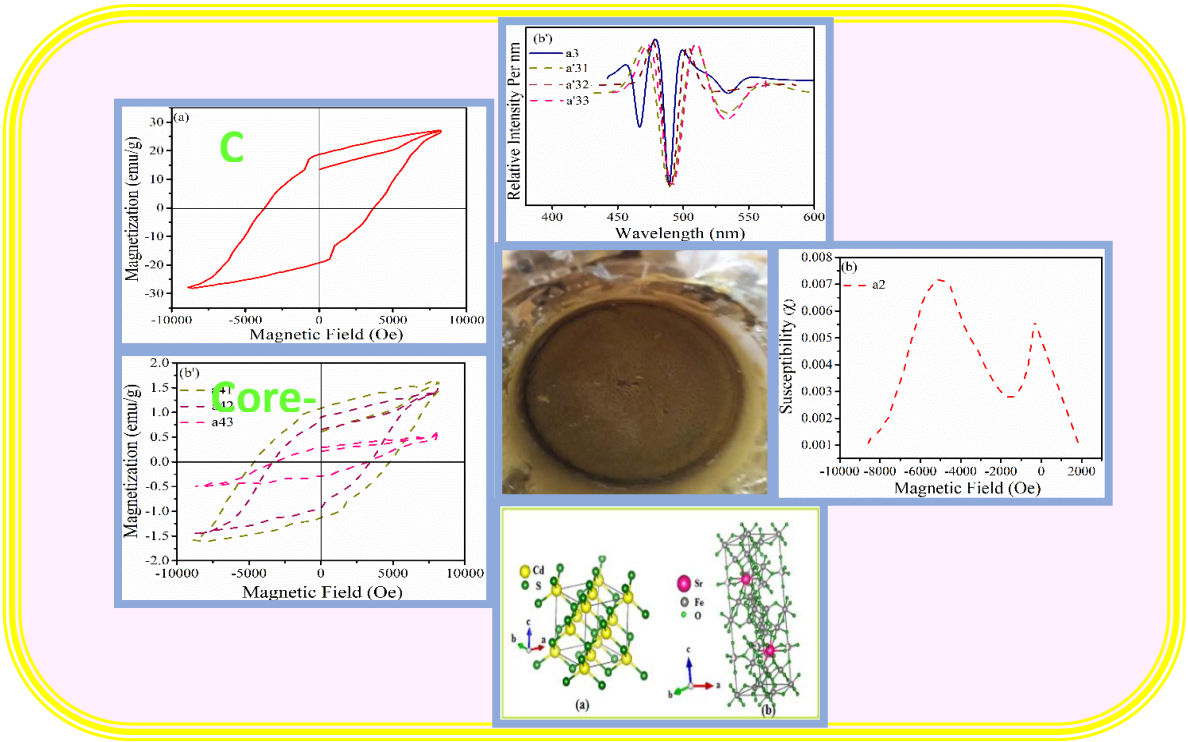

Highlights

- Synthesis of Strontium Hexa Ferrite (SHF) by the "sol-gel route".
- CSNs with SHF core and CdS shell synthesised with three distinct core loadings and three different CdS shell particle sizes.
- The effects of 2-Mercaptoethanol on optical properties and core loading on magnetic properties were investigated.
- Thorough optical and magnetic analysis are done to study interface.
- When there is only one easy direction, uniaxial anisotropy is achieved.
- Functionalizing can help in the use of prepared nanoparticles as they can be magnetically directed, while being optically traced *in-vivo* and *in-vitro*.

Abstract

Pioneering "magneto-fluorescent" CSNs were developed in this chapter by self-assembling CdS QDs on $SrFe_{12}O_{19}$ (SHF) exterior to combine optical and magnetic capabilities into a single unit. The characteristics of SHF/CdS CSNs produced with various core loadings are diverse. The creation of core, shell, and CSNs is supported by "Xray diffraction studies". The luminescence is attributable to CdS QDs with better spectrum resolution, according to optical investigations. High coercivity reveals the MNPs' hard-magnetic character, which persists even after CSNs creation, and implies core-shell formation, as the core and shell do not interact. Hysteresis derivatives provide information about new properties. The distinctive surface features of CSNs are represented by "FTIR spectroscopy". The multifunctionality of CSNs has potential uses, such as "optical reporters with magnetic-handlers for use in bioassays and cell sorting applications that require a permanent magnetic field".

4.1 Introduction

In a wider variety of nanomaterials, the CSNs has been extensively deliberate [1–4]. Furthermore, as the shape, size, and composition of the material changes, this method becomes the norm, presenting an innovative classification of materials design and adaptive features in science and technology applications. Because of its widespread applicability in biological and electronic sectors, “magneto- fluorescent” CSNs are currently attracting a lot of attention. One of the types is the CSNs of SHF and CdS QDs. CdS QDs offer inimitable optical and electrical features, such as a narrow emission band and high photobleaching resistance. “Due to improved saturation magnetization, high Curie temperature, and chemical stability, soft NZF materials are currently the part of essential research”. [5–7]. “SHF is a hard-ferromagnetic material with a very high coercivity that can be employed in situations where persistent magnetism is required. We concentrated on core-shell nanostructures of SHF/CdS in this research because they have a wide range of applications in sectors where both optical and permanent magnetic properties are required in the same entity such as in the cell sorting and drug targeting applications” [8–13]. Existing work is based on SHF/CdS CSNs. We conducted a lot of investigations on the particular category of CSNs and discovered some interesting outcomes. Several findings in this pioneering collection of CSNs lead us to believe that there are significant changes in “structural, optical, and magnetic properties”. According to the literature, both hard-ferrite-core CSNs and soft-ferrite-core CSNs have substantial applications in medicine, opto-electronics, and other domains [14-15]. “Hexagonal MPs can be made in a range of shapes and sizes, however adding a CdS layer to the surface changes the overall shape of the nanoparticles, resulting in a spherical or near-spherical morphology”. When hexagonal nanoparticles with magnetite-rich corners and edges are coated with a CdS layer, they preserve their magnetic characteristics, with the CSNs exhibiting “ferromagnetic behaviour”. We were able to discover the “magneto-fluorescent” properties of the CSNs by a detailed analysis that includes the shell tunability over a variety of cores.

The aqueous “sol gel synthesis” of SHF, solution growth of CdS & their core-shell structures and characterization is the subject of this chapter. At two temperatures, $SrFe_{12}O_{19}$ was annealed (900^{o}C and 1000^{o}C respectively). In addition, the nanostructures were created in accordance with the thesis' objectives. As a result, we created CSNs with varying core loading (0.20 g, 0.10 g & 0.05 g in mass) and variable CdS (1, 2 & 4) shell. Optical,

Structural, morphological, and magnetic behaviour of prepared nanoparticles have been examined, and are conferred in this chapter.

4.2 Experimental details

Ferrite nanoparticles were synthesised at 80-90 degrees Celsius before being annealed at high temperatures. $SrFe_{12}O_{19}$/CdS nanostructures were created using a two-step synthesis procedure. MPs were produced individually in the first stage, and then dispersed in a CdS solution in the second step to form core-shell nanostructures as discussed in 2nd Chapter (section 2.2.3). Several factors that affect the features of bare CdS QDs, bare ferrite, and their CSNs, were characterise through "(XRD) X-ray diffraction (XRD), Transmission electron microscopy (TEM), energy dispersive analysis by X-rays (EDX), absorbance spectroscopy, photoluminescence spectroscopy, vibrating sample magnetometry (VSM) and Fourier transform infrared spectroscopy (FTIR)".

4.3 Results and Discussion

Figure 4.1 (a) showpieces the diagram for the crystal assembly of CdS QDs having the space group *"F-43m"* and Figure 4.1 (b) shows the crystal structure of SHF. "SHF's hexagonal structure is considered to be conjured of alternating spinel (S = $Fe_6O_8^{2+}$) and hexagonal (R = $SrFe_6O_{11}^{2-}$) layers. The O^{2-} ions and Sr^{2+} ions are closed packed, in the hexagonal layer and; the Fe^{3+} ions are spread at the sites ''octahedral'' (12k, 2a and 4f2), ''trigonal-bipyramidal'' (2b) and ''tetrahedral'' (4f1). Super-exchange interactions through the O^{2-} ions assist magnetic moments of the Fe^{3+} ions are coupled to each other. The Sr^{2+} ion is much accountable for the big ''magnetic uniaxial anisotropy'' as it causes agitation of the crystal lattice" [16].

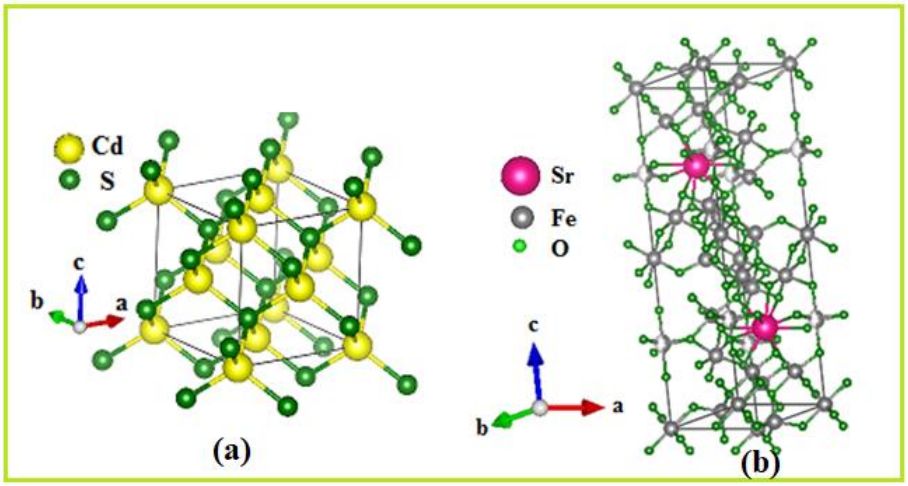

Figure 4.1: (a) Crystal structures of CdS QDs and (b) Crystal structure of Strontium hexa ferrite

4.3.1 Structural analysis of CdS QDs, $SrFe_{12}O_{19}$ and the CSNs of $SrFe_{12}O_{19}$/CdS

"XRD spectra" of the SHF, CdS and the CSNs of SHF/CdS are encompassed in Figure 4.2 (a and b) with SHF being annealed at 900°C and 1000°C respectively. Pattern (b1 and b'1) in both the images shows the XRD spectra for SHF and the planes indexed at (105), (110), (008), (107), (114), (201), (205), (304) and (220) direct towards the "hexagonal structure of SHF according to JCPDS 84-1531". Graphs (a2-a4) in both the images displays the "XRD spectra" for the CdS QDs (1, 2 & 4) with peak reflections at (111), (220) and (311) and specify the "cubic structure for CdS QDs according to JCPDS 80-0019". CSNs spectra were revealed in Figure 3.2 (b5-b7/b'5-b'7). Peaks of both the constituents are in the exact identical positions in the core-shell spectra as they are in their individual spectra. Furthermore, in CdS coated CSNs the relative intensity of the peaks indicating the magnetite phase fall. Reduced SHF peak intensities could indicate higher CdS QD coverage of the core ferrite [17]. The creation of core-shell nanostructure is supported by the nature of CSNs. The Scherrer's formula was used to compute the "crystallite size of the SHF and CdS QDs". Because the peaks for the core and shell are separate, XRD cannot be used to calculate crystallite size for core-shell. Because an only peak for the CSNs is impractical. The parameters computed using XRD analysis and are listed in Table 4.1.

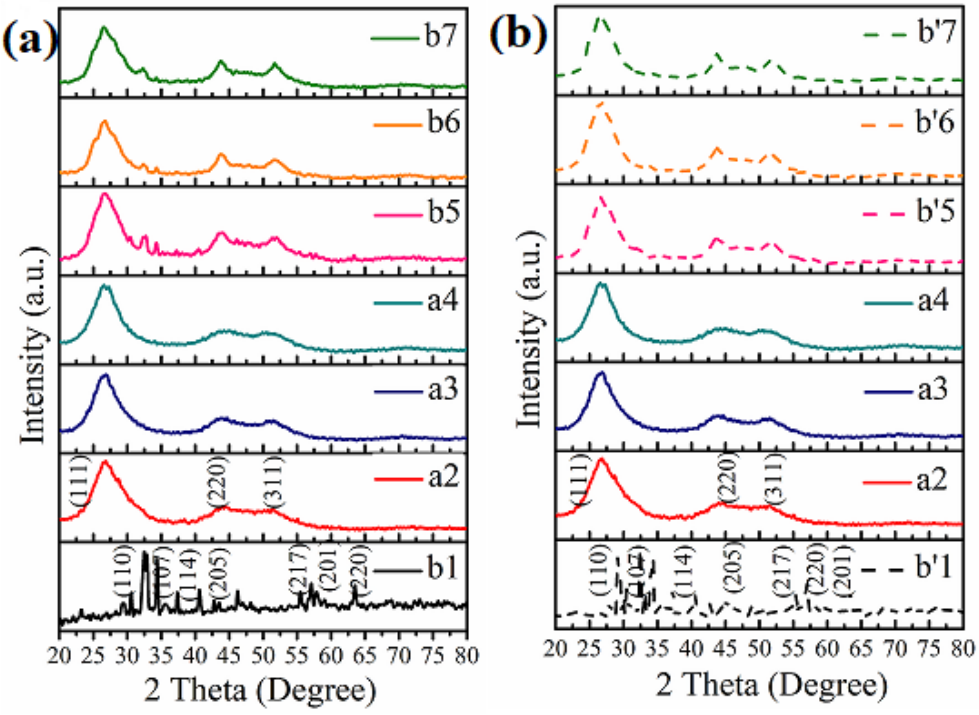

Figure 4.2: (a) and **(b)** XRD spectra of synthesized nanostructures where SHF annealed at 900°C and 1000°C respectively

The following are the labels that were used to discuss the samples:

(b1: b'1): XRD spectra of SHF core annealed at 900°C and 1000°C respectively

(a2, a3 and a4): XRD spectra of CdS QDs (1, 2 and 4 individually formed with 1ml, 2ml and 4ml 2-ME)

(b5: b'5): XRD spectra of CSNs with 0.2 g SHF loading and CdS2 shell, with SHF annealed at 900°C and 1000°C respectively

(b6: b'6): XRD spectra of spectra for CSNs with 0.1 g SHF loading and CdS2 shell with NZF annealed at 900°C and 1000°C respectively

(b7: b'7): XRD spectra of CSNs with 0.05 g SHF core loading and CdS2 shell with SHF annealed at 900°C and 1000°C respectively

Table 4.1: Structural parameters of ferrites (annealed at 900°C and 1000°C), CdS1, CdS2, CdS4 QDs, and their CSNs

Sample name	2θ Position	hkl	Size from XRD (nm)
b1	30.57/3241/34.37/37.33/40.62/55.45/57.73/63.51	110/107/114/203/205/217/201/220	23.54
a2	26.85/44.29/51.01	111/220/311	1.83
a3	26.79/44.41/51.45	111/220/311	1.59
a4	26.75/44.21/51.22	111/220/311	1.46
b5	26.28/27.81/30.42/32.47/34.21/37.25	111/113/110/107/114/203	-
b6	26.28/27.70/32.37/34.32/44.25	111/113/107/114/220/311	-
b7	26.94/28.14/32.58/34.21/44.20/51.26	111/113/107/114/220/311	-
b'1	29.97/32.31/34.26/37.33/40.53/55.39/57.04/63.40	110/107/114/203/205/217/201/220	27.54
b'5	26.51/28.35/30.56/32.47/34.32/37.36/43.98/51.90	101/113/110/107/114/203/112	-
b'6	26.51/28.35/32.80/34.21/44.20/51.26	101/113/107/114/110/112	-
b'7	26.61/28.46/44.30/51.26	101/113/110/112	-

4.3.2 Rietveld refinement

The resulting XRD spectra were refined using the "Full Prof software". The retvield fitted graphs of some of the selected CSNs with their bare species are shown in Figure 4.3. The experimental data is in good agreement with the estimated profile, as can be seen from the graphs. The goodness of fit value nearly indicates that all spectra are well-fitted, as well as the difference amid experiential and computed profiles are in good agreement. "For cubic CdS QDs, hexagonal phase of SHF, and two diverse phases of CSNs, the experimental data is well aligned with the refined data points (black spectra), having space group of *"F-43m"* for CdS QDs and "*63/mmc"* for SHF". The results after refinement proves the efficacy of the method

opted to develop special kind of CSNs. Table 4.2 lists the many parameters that were determined utilizing refinement process.

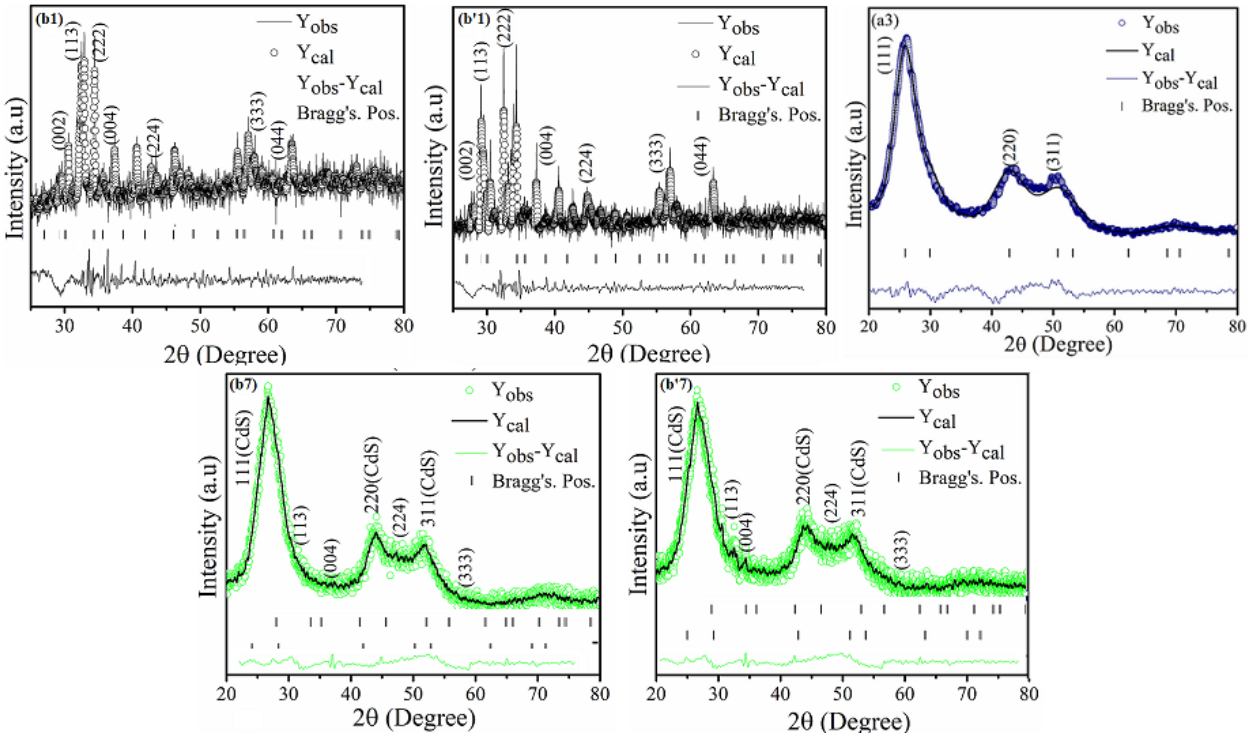

Figure 4.3: Rietveld refined spectra of synthesized nanostructures

The following are the labels that were used to discuss the samples:

(b1: b'1): Rietveld refined spectra of SHF core annealed at 900°C and 1000°C respectively

(a3): Rietveld refined spectra of CdS2 QDs shell (formed with 2ml of 2-ME)

(b7: b'7): Rietveld refined for CSNs with 0.05 g SHF loading and CdS2 shell with SHF annealed at 900°C and 1000°C respectively

Table 4.2: Summary of various parameters calculated using Rietveld refinement

Composition		Lattice Parameter		Cell Volume	Phase Fraction	R_B	R_F	GOF	χ^2
		a (Å)	b (Å)	V (A^3)	(%)				
a3 (CdS2) (SG: *F-43m*)		5.9	--	212.4	100	3.6	3.1	1.1	1.4
b1(SG: 63/mmc)		5.4	23.0	157.46	100	4.3	3.7	2.9	2.3
b'1(SG: 63/mmc)		5.5	23.8	166.37	100	3.9	3.4	3.6	2.5
b7	CdS	5.8	--	199.2	94.5	6.3	4.5	3.8	3.2
	SHF	5.0	22.7	125	4.37.6				
b'7	CdS	5.8	--	197.5	92.3	4.8	3.2	3.9	3.6
	SHF	5.1	22.8	132.65	5.28.1				

4.3.3 Morphological analysis

4.3.3.1 Transmission electron microscopy

TEM pictures of $SrFe_{12}O_{19}$/CdS core-shell nanostructures are shown in Figure 4.4. TEM investigation validates the constructed core-shell nanostructure's spherical shape. The intermediate core composition with the CdS2 shell is depicted in micrographs. Micrographs (a and b) are showing the picture of CSNs with core being annealed at 900°C and 1000°C respectively. Average size of particles obtained from TEM are presented through the histogram plots (c and d). Both of the micrographs display some agglomeration due to the permanent magnetic character of SHF.

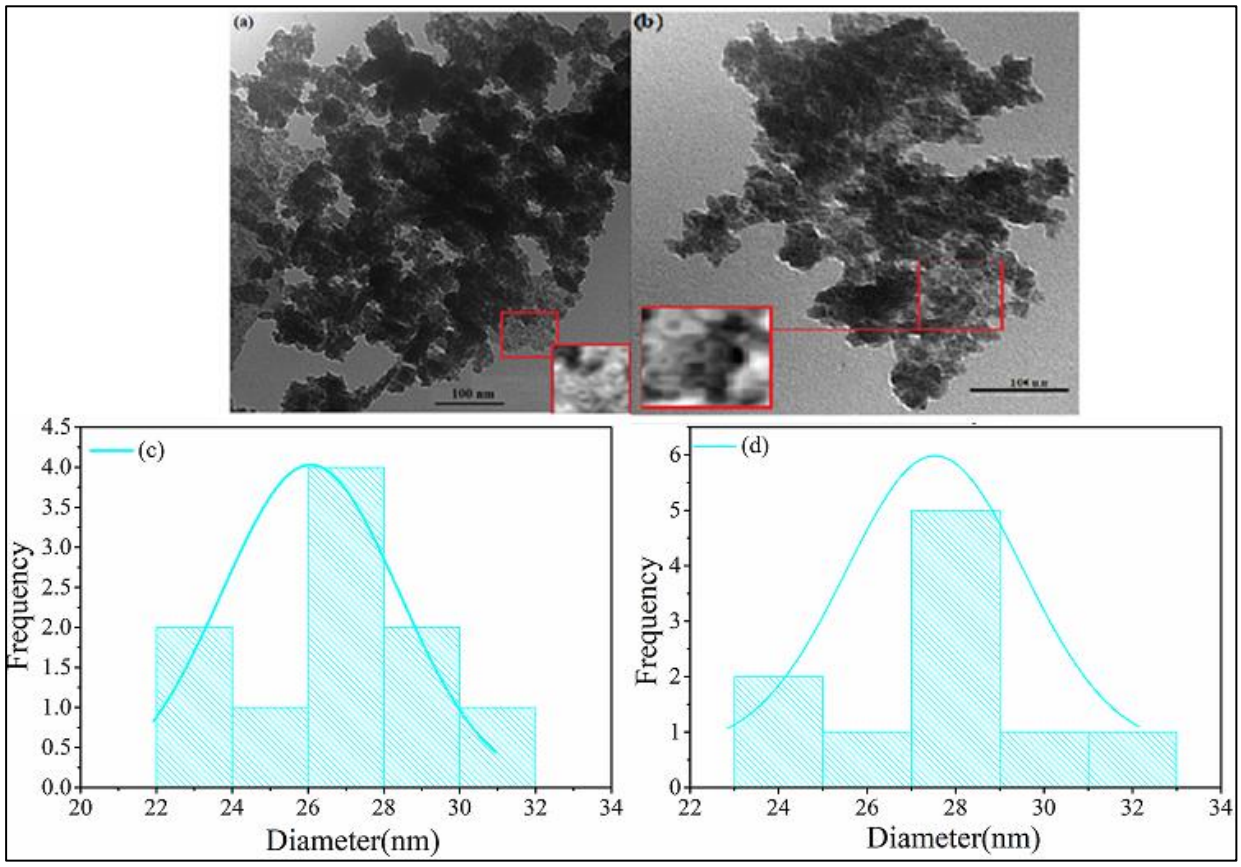

Figure 4.4: (a and b) TEM images for the CSNs with SHF loading of 0.05 g and shell of CdS2 where SHF is being annealed at 900°C and 1000°C respectively. **(c and d)** show the histograms for the respective samples

4.3.3.2 Energy dispersive X-ray spectra

The elemental composition of SHF/CdS CSNs was confirmed using "EDX spectra", EDX validated the atomic percentage for the CSNs generated with minimal core loading and a CdS2 shell and are shown in figure 4.5 (a & b). The presence of peaks of core and shell

elements in CSNs can be seen. As the secondary electron signals gained from the outer layer more efficiently, the peaks from the shell are in perfect stoichiometry. Other peaks, on the other hand, have a good stoichiometric ratio according to the molecular formula utilized in the synthesis process, although there are some discrepancies in the core, as it is in the inner part of CSNs. Because carbon coated copper grids were employed as sample holders for characterization of samples, carbon peaks can be seen in EDX spectra. Moisture effect during characterization is responsible for the presence of oxygen in spectra. In table 4.3, the atomic percentages of different elements in the CSNs are listed.

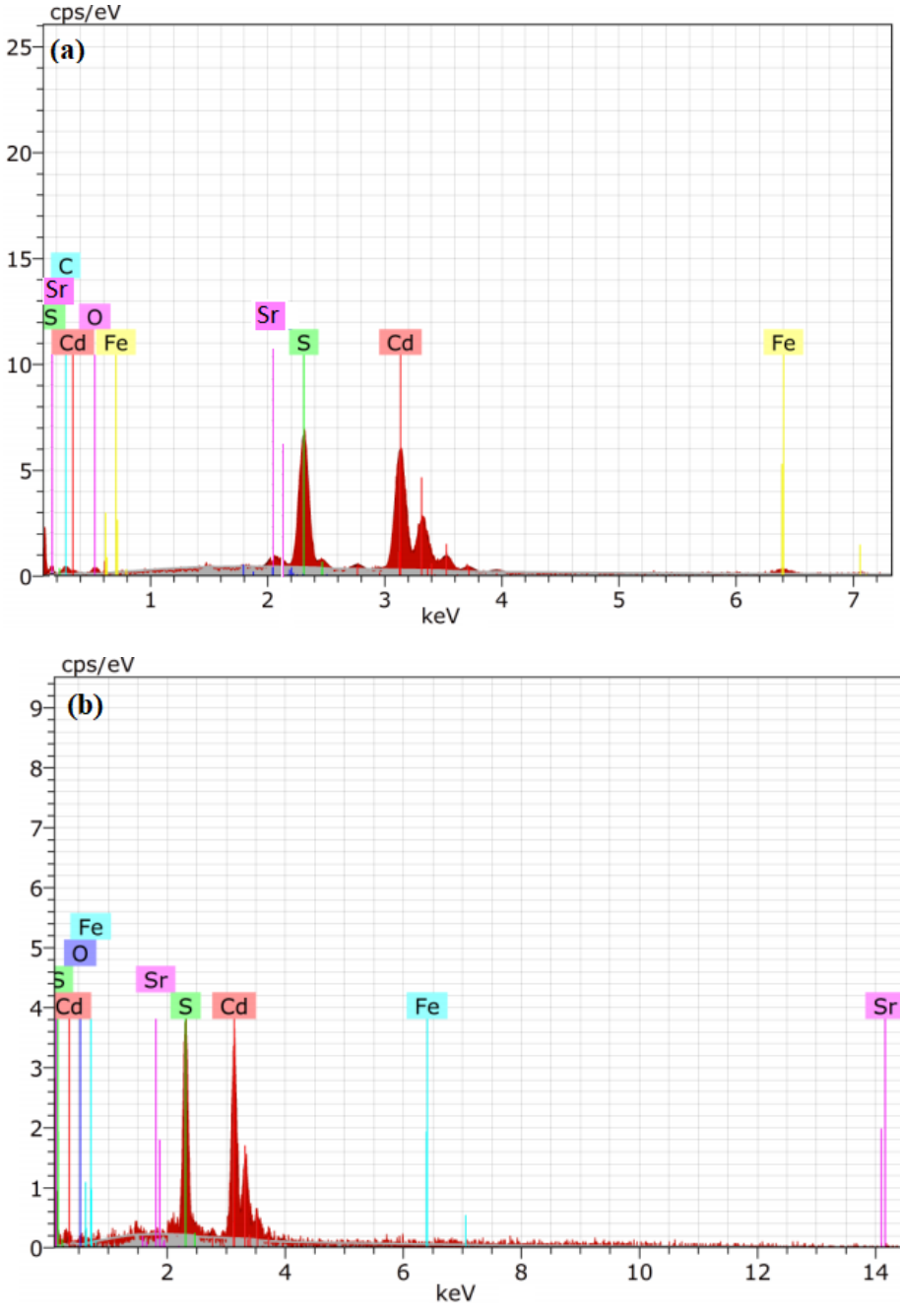

Figure 4.5: (a, b) shows the EDX spectra for the CSNs with SHF loading of 0.05 g and CdS2 shell where, SHF is being annealed at 900ºC and 1000ºC respectively

Table 4.3: Elemental atomic percentage of different elements in the CSNs

ATOMIC PERCENTAGE (%)			
S. No.	Elements	Sample (a)	Sample (b)
1.	Fe	4.96	0.67
2.	C	15.30	Nil
3.	Sr	2.11	0.23
4.	O	10.15	10.78
5.	Cd	32.19	42.13
6.	S	34.57	46.19

4.3.4 Optical studies

4.3.4.1 Absorbance spectroscopy

Figure 4.6 illustrates the "UV–vis spectra" for the basic core, shell and the CSNs in 380–800 nm range where the core is annealed at 900ºC and 1000ºC respectively.

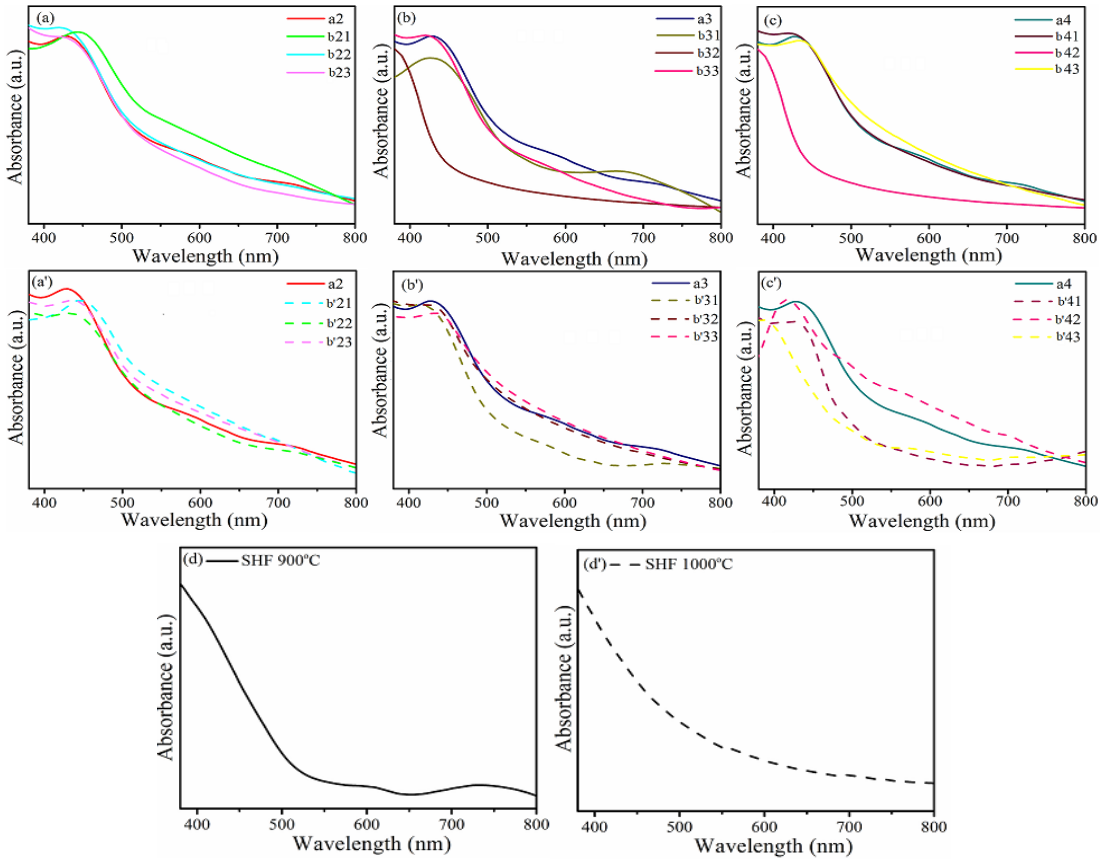

Figure 4.6: Shows UV- vis spectra for prepared nanostructures

The following are the labels that were used to discuss the samples:

Figure (a: a'): UV-vis spectra of CdS1 shell and CSNs of CdS1 with different loading of SHF core annealed at 900°C and 1000°C respectively

Graph (a2): UV-vis spectra of CdS1 QDs shell (CdS1 formed with 1ml 2-ME)

Graph (a21: a'21): Spectra of CSNs; 0.2 g SHF loading and CdS1 shell

Graph (a22: a'22): Spectra of CSNs; 0.1 g SHF loading and CdS1 shell

Graph (a23: a'23): Spectra of CSNs; 0.05 g SHF loading of 0.05 g and shell of CdS1

Figure (b: b'): UV-vis spectra for CdS2 shell and CSNs of CdS2 with different loading of SHF core annealed at 900°C and 1000°C respectively

Graph(a3): UV-vis spectra of CdS2 QDs shell (CdS2 formed with 2ml 2-ME)

Graph (a31: a'31): Spectra of CSNs; 0.2 g SHF loading and CdS2 shell

Graph (a32: a'32): Spectra of CSNs; 0.1 g SHF loading and CdS2 shell

Graph (a33: a'33): Spectra of CSNs; 0.05 g SHF loading and CdS2 shell

Figure (c: c'): UV-vis spectra ofCdS4 shell and CSNs of CdS4 with different loading of SHF core annealed at 900°C and 1000°C respectively

Graph (a4): UV-vis spectra ofCdS4 QDs shell (CdS4 formed with4ml 2-ME)

Graph (a41: a'41): Spectra of CSNs; 0.2 g SHF loading and CdS4 shell

Graph (a42: a'42): Spectra of CSNs; 0.1 g SHF loading of and CdS4 shell

Graph (a43: a'43): Spectra of CSNs; 0.05 g SHF loading and CdS4 shell

Figure (d: d'): Spectra of SHF annealed at 900°C and 1000°C respectively

By comparing the several sets of samples, we were able to determine changes in the absorbance highest and additional optical parameters. The greater dispersion of surface defects of nanomaterials is due to the improved surface-to-volume ratio of smaller nanoparticles; thus, reduced particle sized nanomaterials show wide-ranging and strong absorption peaks. The absorbance maxima of CdS QDs are near 430 nm, corresponding to their band gap. While there is a shift in the absorbance maxima with the core-shell development, this could be related to the SHF substrate effect [18]. SHF nanoparticles serve as a substrate for the formation of CdS nanoparticles in core-shell nanostructures. Small CdS QDs seed development on the SHF substrate causes stress in the CSNs, as previously discussed in "XRD data", which is the cause of the alteration in absorbance positions in CSNs. Another factor for the shift in peak positions is lattice mismatch.

5.3.4.1.1 Derivative study of absorbance

Computation has been done utilizing the 2nd order derivative of absorbance for each sample to obtain the exact absorbance positions for samples. Disparity in the peak behaviour which looks inept to perceive from the "fundamental zero order or D_0 spectra" in the Figure 4.7 is

attainable by DSM. In comparison to the absorbance maxima of CdS QDs, the absorbance maxima of the core-shell nanostructure show a small shift. The successful creation of core-shell nanostructure was attributed to a shift in the absorbance peak location with CSNs establishment.

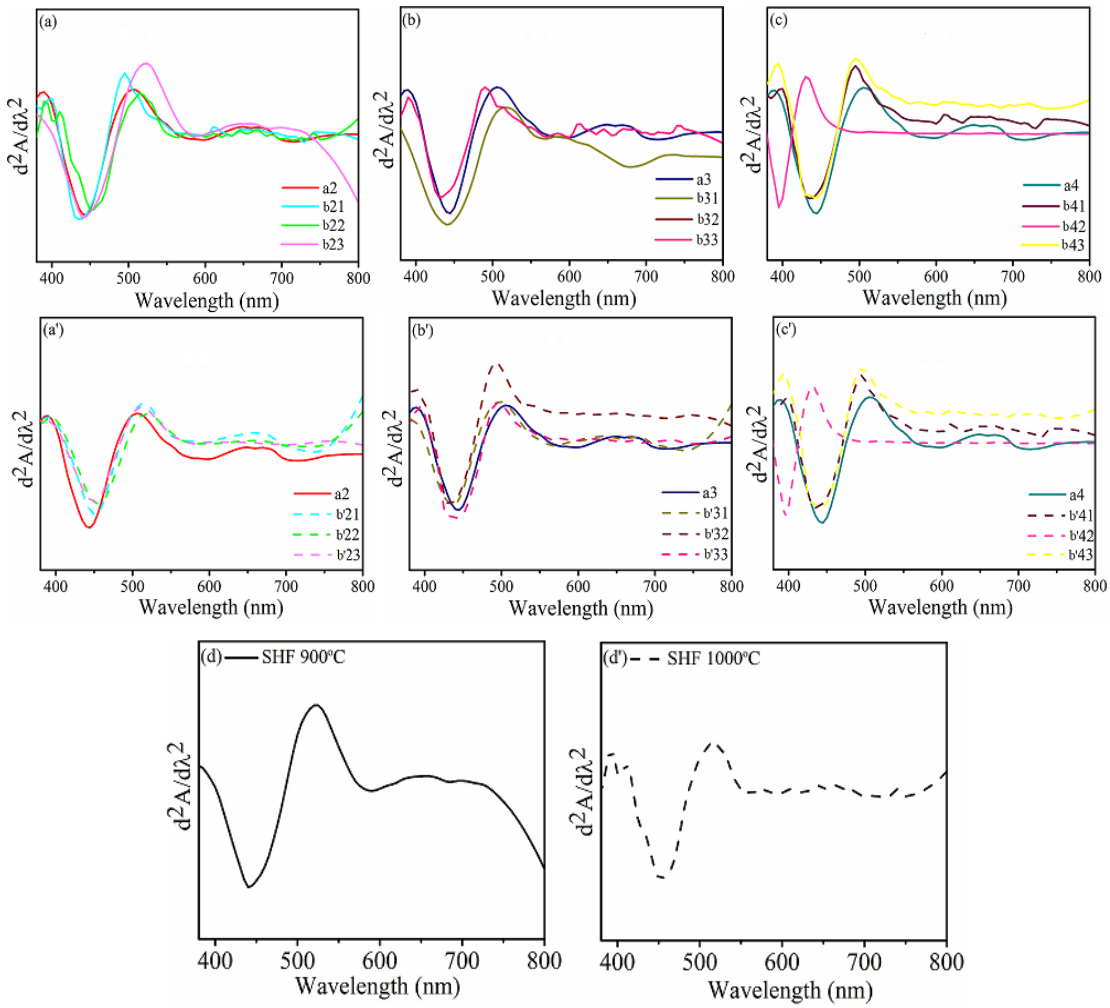

Figure 4.7: Derivative of UV-vis spectra for prepared nanostructures

The following are the labels that were used to discuss the samples:

Figure (a: a'): UV-vis derivative spectra of CdS1 shell and CSNs of CdS1 with different loading of SHF core annealed at 900°C and 1000°C respectively

Graph (a2): UV-vis derivative spectra of CdS1 QDs shell (CdS1 formed with 1ml 2-ME)

Graph (a21: a'21): Spectra of CSNs; 0.2 g SHF loading and CdS1 shell

Graph (a22: a'22): Spectra of CSNs; 0.1 g SHF loading and CdS1 shell

Graph (a23: a'23): Spectra of CSNs; 0.05 g SHF loading of 0.05 g and shell of CdS1

Figure (b: b'): UV-vis derivative spectra for CdS2 shell and CSNs of CdS2 with different loading of SHF core annealed at 900°C and 1000°C respectively

Graph(a3): UV-vis derivative spectra of CdS2 QDs shell (CdS2 formed with 2ml 2-ME)

Graph (a31: a'31): Spectra of CSNs; 0.2 g SHF loading and CdS2 shell

Graph (a32: a'32): Spectra of CSNs; 0.1 g SHF loading and CdS2 shell

Graph (a33: a'33): Spectra of CSNs; 0.05 g SHF loading and CdS2 shell

Figure (c: c'): UV-vis derivative spectra ofCdS4 shell and CSNs of CdS4 with different loading of SHF core annealed at 900°C and 1000°C respectively

Graph (a4): UV-vis derivative spectra ofCdS4 QDs shell (CdS4 formed with4ml 2-ME)

Graph (a41: a'41): Spectra of CSNs; 0.2 g SHF loading and CdS4 shell

Graph (a42: a'42): Spectra of CSNs; 0.1 g SHF loading of and CdS4 shell

Graph (a43: a'43): Spectra of CSNs; 0.05 g SHF loading and CdS4 shell

Figure (d: d'): Derivative Spectra of SHF annealed at 900°C and 1000°C respectively

4.3.4.2 Photoluminescence spectroscopy

The photoluminescence of several sets of CSNs samples is depicted in Figure 4.8 All of the nanostructures' emission spectra were noted at a static wavelength of 350 nm. "The band edge emission of CdS1, CdS2, and CdS4 is at 489 nm, 488 nm, and 484 nm, respectively". Sharp and unambiguous emission peaks have been observed using derivative spectroscopy. When comparing dissimilar sets of CSNs, it was discovered that the CSNs interface, the substrate effect of SHF, and the different sized shell created exterior to core all induce differences in emission. Table 4.4 shows the emission peak intensities and positions based on PL data. Table 4.5 tabulates a systematic discussion of the PL behaviour when the core loading is changed and the CdS shell is changed. We are receiving good luminescence qualities that are similar to

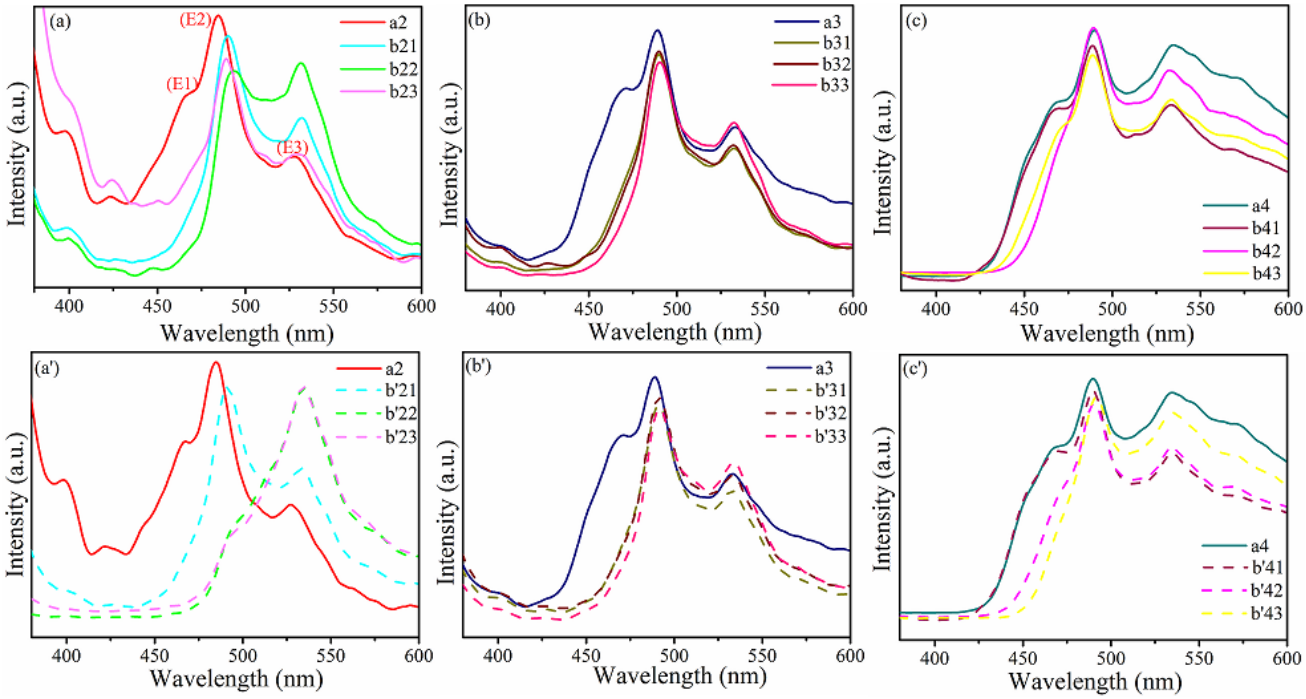

the spectra of CdS QDs. As a result, we can conclude that in CSNs, only the shell participates in the luminescence because the core has no luminescence capabilities.

Figure 4.8: Photoluminescence spectra for prepared nanostructures with most prominent emission peaks being represented by E1, E2 and E3 in each profile.

The labels used to talk about the samples are as follows:

Figure (a: a'): PL spectra for CdS1 shell and CSNs of CdS1 with different loading of SHF core annealed at 900°C and 1000°C respectively

Graph (a2): PL spectra for CdS1 QDs shell (CdS1 formed with 1ml of 5% solution of 2-ME)

Graph (b21: b'21): PL spectra for CSNs; 0.2 g SHF loading and CdS1 shell

Graph (b22: b'22):PL spectra for CSNs; 0.1 g SHF loading and CdS1 shell

Graph (b23: b'23):PL spectra for CSNs; 0.05 g SHF loading and CdS1 shell

Figure (b: b'): PL spectra of CdS2 shell and CSNs of CdS2 with different loading of SHF core annealed at 900°C and 1000°C respectively

Graph(a3): PL spectra for CdS2 QDs shell (CdS2 formed with 2-ME)

Graph (b31: b'31): PL spectra for CSNs; 0.2 g SHF loading and CdS2 shell

Graph (b32: b'32): PL spectra for CSNs; 0.1 g SHF loading and CdS2 shell

Graph (b33: b'33): PL spectra for CSNs; 0.05 g SHF loading and CdS2 shell

Figure (c: c'): PL spectra of CdS4 shell and CSNs of CdS4 with different loading of SHF core annealed at 900°C and 1000°C respectively

Graph(a4): PL spectra for CdS4 QDs shell (CdS4 formed with 2-ME)

Graph (b41: b'41): PL spectra for CSNs; 0.2 g SHF loading and CdS4 shell

Graph (b42: b'42): PL spectra for CSNs; 0.1 g SHF loading and CdS4 shell

Graph (b43: b'43):PL spectra for CSNs; 0.05 g SHF loading and CdS4 shell

"From this result it is also clear that core and shell are not interfering with each other and only doing their separate works this is a good indication for multifunctional CSNs as the core and the shell are completely intact from one another. It is because; if they were not intact there might be the possibilities of quenched luminescence or no luminescence because of the presence of non-luminescent magnetic core. In all the CSNs there is the presence of two peaks which is due to the particle size distribution during synthesis process" [19-20].

Table 4.4: Summary of various parameters calculated by the PL spectroscopy for the CdS shell and CSN

S. No	Sample name	Peak positions (nm)			Intensities (a.u.)		
		E_1	E_2	E_3	I_1	I_2	I_3
1.	a2	466.2	484.3	535.5	184.7	222.0	171.0
2.	b21/b'21	-	489.17/**490.11**	529.89/**534.59**	-	215/**219.09**	162.81/**155.09**
3.	b22/b'22	-	492.78/--	530.58/**535.05**	162.1/**188.13**	200.08/**210.16**	100.12/**89.02**
4.	b23/b'23	426.28/-	486.94/--	529.12/**532.61**	189/-	210/**201.9**	163.23/**171.56**
5.	a3	469.10	488.65	532.71	175	214	164
6.	b31/b'31	-	489.17/**492.30**	533.59/**532.13**	-	120.30/**90.2**	132.02/**63.23**
7.	b32/b'32	-	489.94/**491.15**	532.13/**533.81**	-	211.51/**210.21**	92.02/**79.32**
8.	b33/b'33	-	489.17/**491.40**	532.13/**532.81**	-	209.23/**208.44**	150.21/**156.36**
9.	a4	468.18	488.69	534.24	180.2	224.4	176.32
10.	b41/b'41	-/**469.72**	489.17/**488.54**	533.59/**535.23**	-/**166.19**	220/**212.32**	168/**153.02**
11.	b42/b'42	-	487.71/**491.02**	532.13/**533.61**	-	221.13/**252.33**	156.3/**159.50**
12.	b43/b'43	-	489.17/**490.26**	532.13/**535.23**	-	225.20/**233**	152.08/**150.81**

4.3.4.2.1 Derivative study of photoluminescence spectra

The DSM has made it possible to discuss the features that were previously indistinguishable or curbed in "PL spectra". When comparing CSNs to bare CdS (1, 2 & 4 QDs), DSM allows us to accumulate all of the miniscule info about the peak alteration and defect states, irrespective of how slight the shift is. Figure 4.9 depicts the CSNs' double derivative curve. We are receiving good luminescence qualities that are similar to the spectra of CdS QDs.

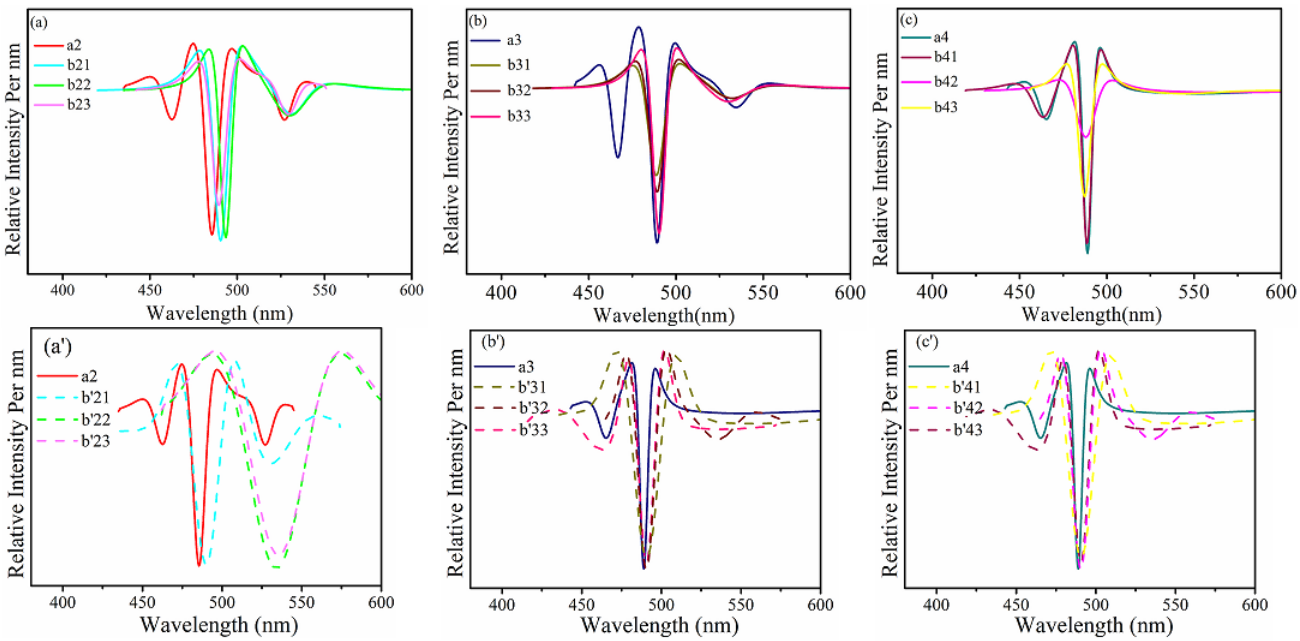

Figure 4.9: Derivative curves of photo luminescence spectra for prepared nanostructures

The labels used to talk about the samples are as follows:

Figure (a: a'): PL derivative spectra for CdS1 shell and CSNs of CdS1 with different loading of SHF core annealed at 900^{o}C and 1000^{o}C respectively

Graph (a2): PL derivative spectra for CdS1 QDs shell (CdS1 formed with 1ml of 5% solution of 2-ME)

Graph (b21: b'21): PL derivative spectra for CSNs; 0.2 g SHF loading and CdS1 shell

Graph (b22: b'22):PL derivative spectra for CSNs; 0.1 g SHF loading and CdS1 shell

Graph (b23: b'23):PL derivative spectra for CSNs; 0.05 g SHF loading and CdS1 shell

Figure (b: b'): PL derivative spectra of CdS2 shell and CSNs of CdS2 with different loading of SHF core annealed at 900^{o}C and 1000^{o}C respectively

Graph(a3): PL derivative spectra for CdS2 QDs shell (CdS2 formed with 2-ME)

Graph (b31: b'31): PL derivative spectra for CSNs; 0.2 g SHF loading and CdS2 shell

Graph (b32: b'32): PL derivative spectra for CSNs; 0.1 g SHF loading and CdS2 shell

Graph (b33: b'33): PL derivative spectra for CSNs; 0.05 g SHF loading and CdS2 shell

Figure (c: c'): PL derivative spectra of CdS4 shell and CSNs of CdS4 with different loading of SHF core annealed at 900^{o}C and 1000^{o}C respectively

Graph(a4): PL derivative spectra for CdS4 QDs shell (CdS4 formed with 2-ME)

Graph (b41: b'41): PL derivative spectra for CSNs; 0.2 g SHF loading and CdS4 shell

Graph (b42: b'42): PL derivative spectra for CSNs; 0.1 g SHF loading and CdS4 shell

Graph (b43: b'43):PL derivative spectra for CSNs; 0.05 g SHF loading and CdS4 shell

Table 4.5: With the altered loading of the core and the changing CdS shell, important findings for PL from SHF/CdS CSNs, where ferrite loadings are 0.2, 0.1, and 0.05, and shell specifications are CdS1, CdS2, and CdS4

S. No.	Shell Particle Size → / Ferrite Loading ↓	CdS1	CdS2	CdS4
1.	0.2 g	With the formation of core\shell band edge intensity is enhanced. *A small hump that is present in CdS at 466 nm is dissolved with the formation of CSNs.* Better particle size distribution as compared to CdS.	With the formation of CSNs small peak present at 469 nm is eliminated. *Better particle size distribution as compared to CdS.* With the formation of CSNs band edge intensity is enhanced.	A small hump that is present in CdS at 466 nm is still present even after the formation of CSNs. *More defect states are present in this structure as compared to CdS1 and CdS2 CSNs because of CdS4 shell defects.*
2.	0.1 g	Band edge and the peak following band edge have same intensity. *Core shell structure formation does not follow the pattern of CdS1 employed.* Some reaction might occur between core and shell at interface which effect the emission profile of shell. *Therefore, this system is not completely intact at the particular composition.*	With the formation of CSNs band edge intensity is enhanced. Core-shell follows the emission profile of CdS2 with better particle size distribution. *Emission peaks are having smallest peak width (enhanced mono-chromaticity), along with higher enough intensities and no defect peaks.* First emission peak is having high intensity ratio in comparison to the second peak which also adds in mono-chromaticity.	In this particular composition small hump is absent. *Defect states arise with the formation of small seed size over the core substrate.*
3.	0.05 g	With the formation of core-shell band edge intensity is enhanced. *A small hump that is present in CdS at 466 nm is appeared slightly even after the formation of CSNs.*	Changing core loading and CdS shell size has not much effect on the emission profile in comparison to the emission profile as that of SHF (0.1) CdS2. *First emission peak is having low intensity ratio in comparison to the second peak with respect to SHF (0.1) CdS2, which negatively*	Maximum defect states are generated in the case of CdS4 shell, different core loading does not affect the CdS emission much in CSNs in comparison to CdS4 because CdS4 already have the many defect states all together.

4.3.5 Magnetic Studies

Figure 4.10 demonstrates the hysteresis loop for the SHF (annealed at 900°C and 1000°C respectively) and the CSNs. A number of parameters have been calculated from the hysteresis curves, which enable us to characterise the nature of magnetism and supplementary variables by which we may get a quick concept for future magnetic investigation. All of the samples' "magnetization, remanence, coercivity, squareness ratio, magnetic anisotropy, and (SFD) characteristics" are listed in Table 4.6. Extreme magnetization is computed for the bare SHF, while maximum magnetization is decayed to several times with the creation of magnetically deceased CdS shell above SHF. In all samples, retentivity follows the same pattern as that of saturation magnetization. Coercivity increases when we move from SHF to SHF/CdS CSNs, where 0.2 g core loading is opted, but it decreases as we move to other sets of CSNs. The anisotropy in the CSNs is broken in some way, resulting in a many-fold less value of anisotropy in CSNs compared to bare core. The most significant sign in the direction of CSNs formation is the degradation of anisotropy with core-shell formation [21-22]. This degradation indicates that the core-shell system is intact, since if the CSNs are not intact, there is a risk of mingling of core and shell materials at the boundary, which could influence anisotropy.

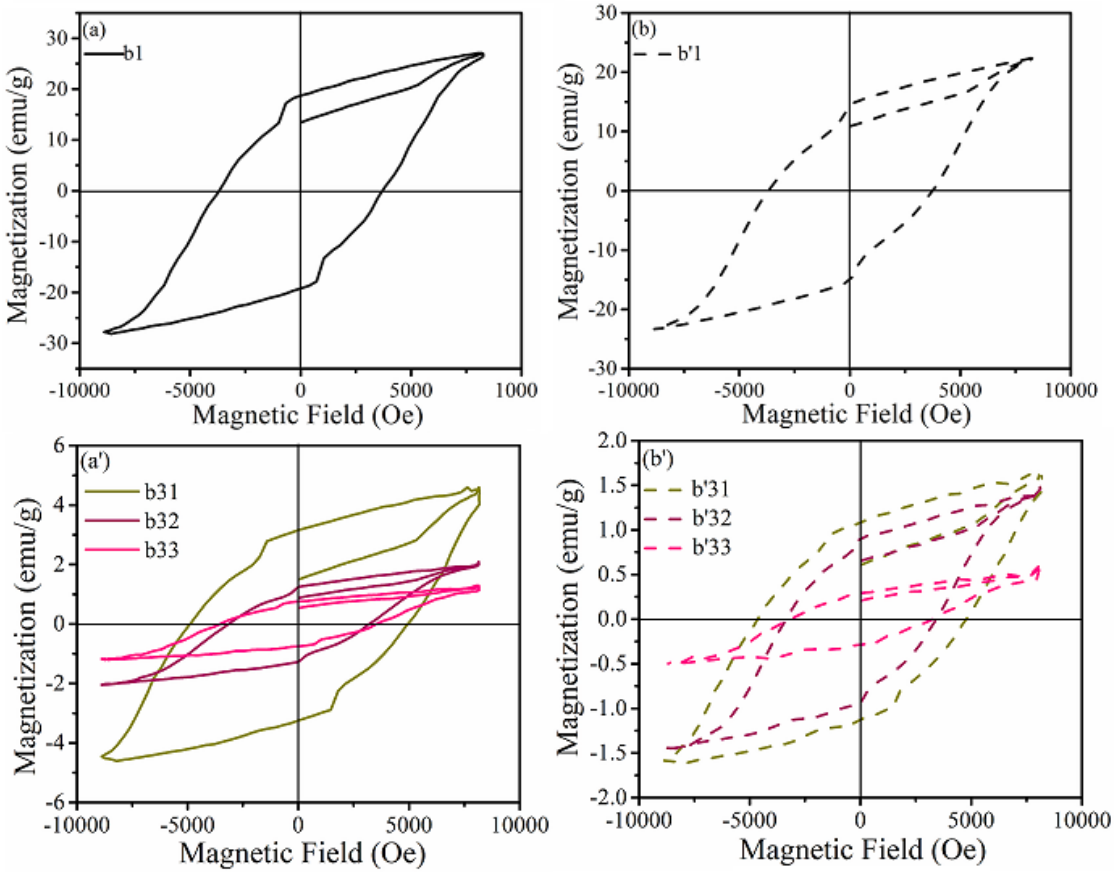

Figure 4.10: Hysteresis curve for the SHF core and CSNs

The labels that were used to discuss the samples are as follows:

(b1: b'1): Hysteresis curve for SHF core annealed at 900°C and 1000°C respectively

(b31: b'31): Hysteresis curve for core-shell; 0.2 g SHF loading and CdS2 shell

(b32: b'32): Hysteresis curve for core-shell; 0.1 g SHF loading and CdS2 shell

(b33: b'33): Hysteresis curve for core-shell; 0.05 g SHF loading and CdS2 shell

However, the anisotropy constant trend is same as that of maximum magnetization trend. Strong coupling is indicated by good squareness and higher remanence. All magnetic moments are parallel in the saturation condition. At the nucleation field, some moments in the layer are already slanted away from the loop direction.

4.3.5.1 Derivative study of hysteresis curve

The magnetic field versus susceptibility curve generated from normal magnetization curves via differential susceptibility is shown in Figure 4.11.

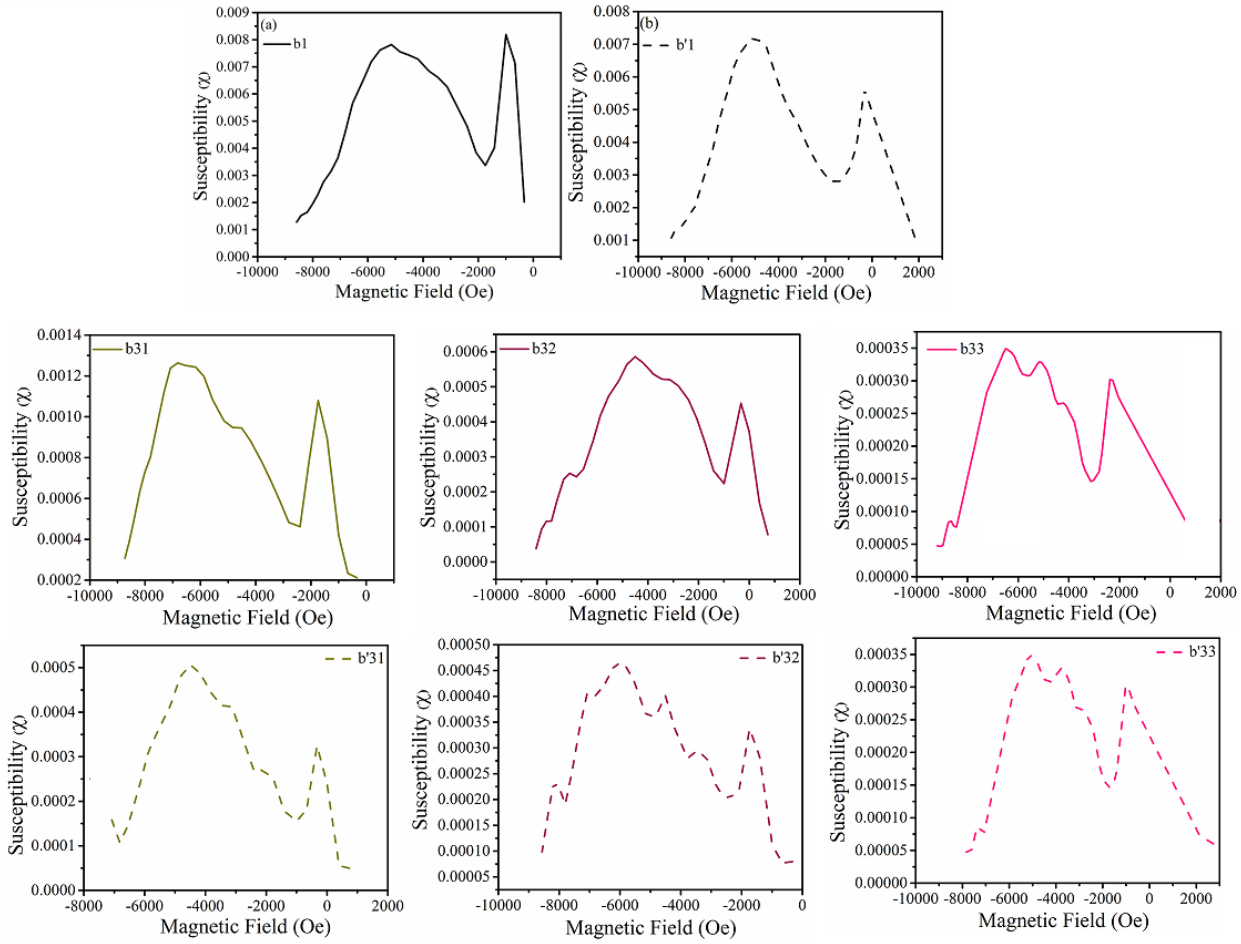

Figure 4.11: First order derivative curve for the core and CSNs

The following are the labels that were used to discuss the samples:

(b1: b'1): 1st order derivative hysteresis curve for SHF core annealed at 900ºC and 1000ºC respectively
(b31: b'31): 1st order derivative hysteresis curve for CSNs; 0.2 g SHF loading and CdS2 shell
(b32: b'32): 1st order derivative of hysteresis for core shell; 0.1 g SHF loading and CdS2 shell
(b33: b'33): 1st order derivative of hysteresis for core shell; 0.05 SHF loading and CdS2 shell

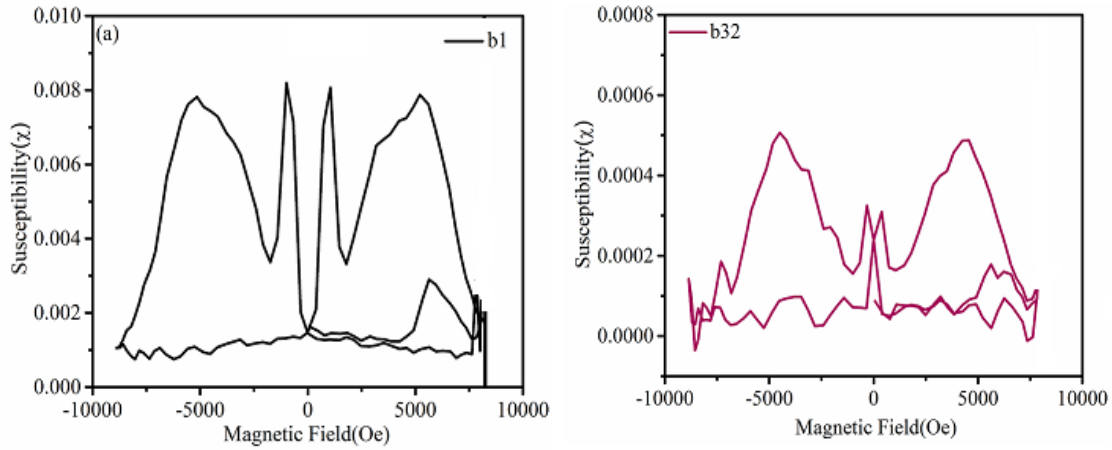

Figure 4.12: Shows the complete magnetization/demagnetization derivative curves of hysteresis loop for prepared nanostructures. (a) bare SHF and (b) core-shell; SHF loading of 0.1 g and shell of CdS2

The SFD curve exhibits a narrow dM/dH peak, which correlates to a small crystallite size dispersal. Furthermore, the large peaks and long tails indicate a percentage of crystallites that aren't adequately "connected via exchange" to the hard phase [23]. When progressing from bare SHF to CSNs with varied SHF loadings, SFD drops. As the amount of SHF in the CSNs system increases, the dM/dH peak widths drop, indicating effective exchange coupling between the "magneto-fluorescent" phases of the nanostructures. The graphs show that every picture has a broad hump followed by a sharp peak; this broad hump is one of the significant pieces of evidence that the SHF is hard magnetic in nature as manufactured. "We can get an indication of the orientation of the spins with a fluctuating magnetic field by calculating the SFD of the samples" [24]. The shift in magnetic nanoparticle loading in the CSNs causes these fluctuations in SFD values. It's possible that this is due to interfacial alterations caused by magnetic-semiconductor exchange coupling.

Table 4.6: Magnetic parameters of ferrite (900°C and 1000°C), and their CSNs

S. No	Sample	M_s(emu/g)	M_r(emu/g)	H_c (Oe)	M_r/M_s	K (erg/cm^3)	SFD
1.	b1	27.55	11.45	3037.79	0.41	41845.55	0.24
2.	b'1	22.87	14.74	3722.79	0.64	42570.10	0.21
3.	b31	4.52	2.79	3514.31	0.61	7942.34	0.14
4.	b32	2.01	1.25	3156.92	0.62	3172.70	0.08
5.	b33	1.19	0.67	2888.88	0.56	1718.88	0.24
6.	b'31	1.59	0.95	3335.62	0.59	2651.81	0.13
7.	b'32	1.45	0.92	3365.40	0.63	2439.91	0.09
8.	b'33	0.5	0.25	2501.71	0.5	625.42	0.05

4.3.6 FT-IR Studies

The FTIR spectra for SHF, CdS QDs, and CSNs in the region of 400–4000 cm^{-1} are shown in Figure 4.13 The majority of the peaks identified in CSNs are of shell, with small alterations in their locations. The absence of SHF peaks on the CSNs spectra indicates that the core is separated from the shell.

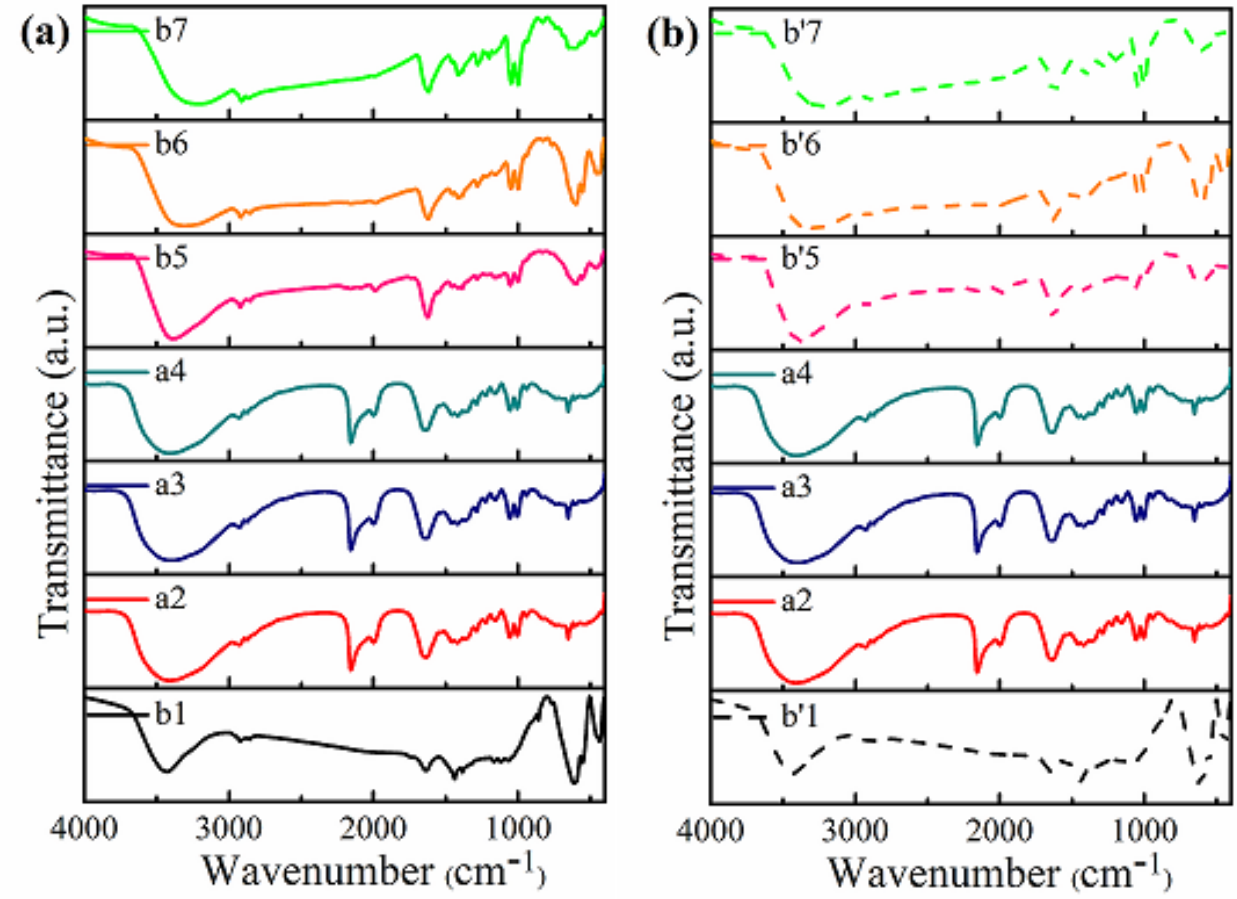

Figure 4.13: (a) and **(b)** Shows the FTIR spectra of synthesized nanostructures

The following labels were used to discuss the samples:

(b1: b'1): FTIR spectra of SHF core annealed at 900°C and 1000°C respectively

(a2, a3 and a4): FTIR spectra of CdS QDs shell (CdS1, CdS2 and CdS4 respectively formed with 1ml, 2ml and 4ml 2-ME)

(b5: b'5): FTIR spectra of CSNs with, 0.2 g SHF loading and CdS2 shell, SHF annealed at 900°C and 1000°C respectively

(b6: b'6): FTIR spectra of CSNs with, 0.1 g SHF loading and CdS2 shell, SHF annealed at 900°C and 1000°C respectively

(b7: b'7): FTIR spectra of CSNs with, 0.05 g SHF loading and CdS2 shell, SHF annealed at 900°C and 1000°C respectively

Table 4.7: Summary of the functional groups for the ferrites (annealed at 900°C and 1000°C), CdS1, CdS2, CdS4 QDs, and their CSNs

Sample Name	Region (Cm^{-1})	Intensity	Interpretation
CdS QDs	400-470	Weak	Cd-S bond stretching (CdS nanoparticles)
	820-850	Sharp	S-S-S bending or C-H stretching
	1060-1120	Sharp	C-O or S-O
	1380-1420	Sharp and Broad	C-H bending of CH_3
$SrFe_{12}O_{19}$	430-470	Small and weak	Lattice vibration of metal at octahedral sites.
	550-580	Sharp and weak	Lattice vibration of metal ions at tetrahedral sites.
	429-588	Broad	Characteristic peaks correspond to the stretching vibration of metal-oxygen bond, indicating the formation of hexaferrite.
	619	Broad and sharp	Octahedral sites in T-S block boundaries
	934	Weak and small	Vibrational frequency of octahedral sites in S and T block of whole complex
	1446	Weak and small	N-O stretching
Core-shell	551	Small and weak	Bending vibration within the molecule
	765-996	Weak	"Corresponds to Cd-S bond which approved the formation of CdS nanoparticles"
	1221-1419	Sharp	C–H bending of CH_3"

4.4 Conclusion

- New classes of nanostructures were created with a set of joint qualities while maintaining the nature of their building blocks.
- The coexistence of both phases in the nanostructures is confirmed by XRD patterns for core, shell, and CSNs with the space groups "*(F-43m)* for CdS and *(P 63/ m m c)* for SHF".
- Optical outcomes support the creation of CSNs deprived of any type of mingling amid core and shell material. When compared to CSNs generated with CdS4 shell, CSN designed with CdS (1 & 2) are defect-free.
- DSM is used for in-depth study of samples in optical analysis. It has proven to be a useful technique for detecting minor variations in peak positions in "UV–visible" and "PL spectroscopy", which can be difficult to detect using 0^{th} order spectra.
- The functional group found in the "FT-IR spectra" of the CSNs spectra is largely attributable to the exterior elements, which is CdS, indicating that CdS was efficaciously grown-up over SHF and indirectly providing strong signal for CSNs creation.
- Magnetic nanoparticles plausibly arranged inside active cells after being functionalized with CdS QDs and optically monitored.

4.5 REFERENCES

[1] Wang, H., Chen, L., Feng, Y. and Chen, H., *Exploiting core–shell synergy for nanosynthesis and mechanistic investigation*. Accounts of chemical research, Vol. 46(7), pp.1636-1646, Jul. 2013.

[2] Liu, W., Zhu, Z., Deng, K., Li, Z., Zhou, Y., Qiu, H., Gao, Y., Che, S. and Tang, Z. *Gold nanorod@ chiral mesoporous silica core–shell nanoparticles with unique optical properties.* Journal of the American Chemical Society, Vol.135(26), pp.9659-966, Jul. 2013.

[3] Lay, A., Siefe, C., Fischer, S., Mehlenbacher, R.D., Ke, F., Mao, W.L., Alivisatos, A.P., Goodman, M.B. and Dionne, J.A., *Bright, mechanosensitive upconversion with cubic-phase heteroepitaxial core–shell nanoparticles.* Nano letters, Vol. 18(7), pp.4454-4459, Jun. 2018.

[4] Zhao, W., Gu, J., Zhang, L., Chen, H. and Shi, J., *Fabrication of uniform magnetic nanocomposite spheres with a magnetic core/mesoporous silica shell structure.* Journal of the American Chemical Society, Vol. 127(25), pp.8916-8917, Jun. 2005.

[5] Moser, A., Takano, K., Margulies, D.T., Albrecht, M., Sonobe, Y., Ikeda, Y., Sun, S. and Fullerton, E.E., *Magnetic recording: advancing into the future*. Journal of Physics D: Applied Physics, Vol. 35(19), p.R157, Sep. 2002.

[6] Lu, X., Liang, G., Sun, Q. and Yang, C., 2011. High-frequency magnetic properties of Ni-Zn ferrite nanoparticles synthesized by a low temperature chemical method. *Materials Letters*, *65*(4), pp.674-676, Feb. 2011.

[7] Coey, J.M.D., *Permanent magnet applications*. Journal of Magnetism and Magnetic Materials, Vol. 248(3), pp.441-456, Aug. 2002.

[8] Liu, J., Zhang, Y., Wang, C., Xu, R., Chen, Z. and Gu, N., *Magnetically sensitive alginate-templated polyelectrolyte multilayer microcapsules for controlled release of doxorubicin.* The Journal of Physical Chemistry C, Vol. 114(17), pp.7673-7679, May.2010.

[9] Dennis, C.L., Jackson, A.J., Borchers, J.A., Hoopes, P.J., Strawbridge, R., Foreman, A.R., Van Lierop, J., Grüttner, C. and Ivkov, R., *Nearly complete regression of tumors via collective behavior of magnetic nanoparticles in hyperthermia.* Nanotechnology, Vol. 20(39), p.395103, Sep. 2009.

[10] Lee, J.H., Huh, Y.M., Jun, Y.W., Seo, J.W., Jang, J.T., Song, H.T., Kim, S., Cho, E.J., Yoon, H.G., Suh, J.S. and Cheon, J., 2007. *Artificially engineered magnetic nanoparticles for ultra-sensitive molecular imaging*. Nature medicine, Vol. 13(1), pp.95-99, Jan. 2007.

[11] Raj, K. and Moskowitz, R., *Commercial applications of ferrofluids*. Journal of Magnetism and Magnetic Materials, Vol. 85(1-3), pp.233-245, Apr. 1990.

[12] Che, R.C., Peng, L.M., Duan, X.F., Chen, Q. and Liang, A.X., *Microwave absorption enhancement and complex permittivity and permeability of Fe encapsulated within carbon nanotubes.* Advanced Materials, Vol. 16(5), pp.401-405, Mar. 2004.

[13] Shi, Y., Ding, J., Tan, S.L. and Hu, Z., *Ni/Fe2O3 magnetic composite synthesized by mechanical alloying.* Journal of magnetism and magnetic materials, Vol. 256(1-3), pp.13-19, Jan. 2003.

[14] Mousavinia, M., Ghasemi, A. and Paimozd, E., *Structural, Magnetic, and Microwave Properties of SrFe 12− x (Ni 0.5 Co 0.5 Sn) x/2 O 19 Particles Synthesized by Sol–Gel Combustion Method.* Journal of electronic materials, Vol. 42(9), pp.2784-2792, Sep. 2013.

[15] Choueikani, F., Royer, F., Jamon, D., Siblini, A., Rousseau, J.J., Neveu, S. and Charara, J., *Magneto-optical waveguides made of cobalt ferrite nanoparticles embedded in silica/zirconia organic-inorganic matrix.* Applied physics letters, Vol. 94(5), p.051113, Feb. 2009.

[16] Li, Q., Song, J., Saura-Múzquiz, M., Besenbacher, F., Christensen, M. and Dong, M., *Magnetic properties of strontium hexaferrite nanostructures measured with magnetic force microscopy.* Scientific reports, Vol. 6(1), pp.1-7, May. 2016.

[17] Rawat, D., Sethi, J., Sahani, S., Barman, P.B. and Singh, R.R., *Pioneering and proficient magneto fluorescent nanostructures: Hard ferrite based hybrid structures.* Materials Science and Engineering: B, Vol. 265, p.115017, Mar. 2021.

[18] Liu, R., Zhao, Y., Huang, R., Zhao, Y. and Zhou, H., *Multiferroic ferrite/perovskite oxide core/shell nanostructures.* Journal of Materials Chemistry, Vol. 20(47), pp.10665-10670, 2010.

[19] Sadollahkhani, A., Kazeminezhad, I., Lu, J., Nur, O., Hultman, L. and Willander, M., *Synthesis, structural characterization and photocatalytic application of ZnO@ ZnS core–shell nanoparticles.* RSC advances, Vol. 4(70), pp.36940-36950, 2014.

[20] Nemade, K.R. and Waghuley, S.A., *UV–VIS spectroscopic study of one pot synthesized strontium oxide quantum dots.* Results in Physics, Vol. 3, pp.52-54, Jan. 2013.

[21] Rawat, D. and Singh, R.R., *Avant-grade magneto/fluorescent nanostructures for biomedical applications: Organized and comprehensive optical and magnetic evaluation.* Nano-Structures & Nano-Objects, Vol. 26, p.100714, Apr. 2021.

[22] Li, D., Pan, D., Li, S. and Zhang, Z., *Recent developments of rare-earth-free hard-magnetic materials.* Science China Physics, Mechanics & Astronomy, Vol. 59(1), p.617501, Jan. 2016.

[23] Neupane, D., Ghimire, M., Adhikari, H., Lisfi, A. and Mishra, S.R., *Synthesis and magnetic study of magnetically hard-soft SrFe12-yAlyO19-x Wt.% Ni0. 5Zn0. 5Fe2O4 nanocomposites.* AIP Advances, Vol. 7(5), p.055602. May. 2017.

[24] S. Torkian, A. Ghasemi, R. S. Razavi, *Magnetic properties of hard-soft SrFe10Al2O19/Co0. 8Ni0. 2Fe2O4 ferrite synthesized by one-pot sol–gel autocombustion*, J. Magn. Magn., Vol. 416(2016), pp.408-416, 2017.

CHAPTER- 5

COMPARISON OF HARD-SOFT FERRITE-BASED CORE-SHELL NANOSTRUCTURES BASED ON STRUCTURAL, MORPHOLOGICAL, OPTICAL, MAGNETIC AND FUNCTIONAL ANALYSIS

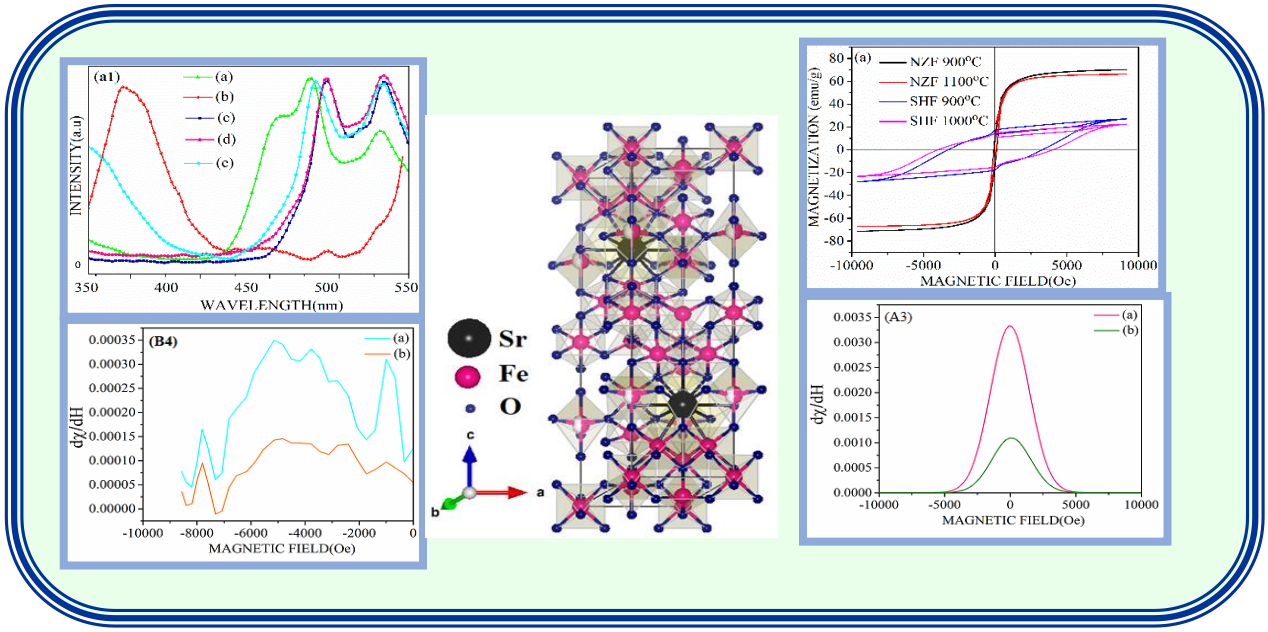

Highlights

- Assessment of two dissimilar sets of CSNs.
- CSNs with NZF core and other set with SHF core are studied.
- In both the sets of CSNs CdS shell is identical.
- All-inclusive optical and magnetic properties were compared.
- Interfacial properties of both the set of CSNs were compared.

Abstract

This chapter addresses the possible comparison of multifunctional CSNs developed with two different core types i.e., “hard ferrite core and the soft ferrite core”. In the ensuing section, we briefly described the nanostructure architecture as well as core and shell options function on the ultimate CSNs performance. Both the sets of core-shell nanostructures present varied features which make them applicable in great range of applications. Since NZF is soft magnetic in nature we can found the applications of NZF based CSNs in drug delivery applications, MRI etc. In case of magnetic cell separation where permanent magnetism is required NZF have restriction because of frail magnetism. thus, we switch for SHF based structures because of their permanent magnetic nature. The comparison of such diverse sets of core-shell nanostructures also paves the way for further research into the type of core-shell nanostructures known as “Magneto-fluorescent heterostructures”, where the core is synthesized by mixing two different ferrites, including both hard and soft ferrites, and a shell made of CdS quantum dots, to create a new class of material with tuneable magnetic and optical properties.

5.1 Introduction

In biological applications, nano-systems have demonstrated promising results and significant advances [1-4]. However, because to their physicochemical and functional qualities, control and targeted distribution of medicines or genes are constrained. “CSNs are a promising nanocarrier method for regulated and targeted medicine delivery applications in this area. Such distinct advantages may make it easier for CSNs to mingle two or more different functional qualities in a single nano system, resulting in the appropriate physicochemical properties needed for successful targeted drug delivery” [5-8]. The current chapter inspects the evolutions and expansions in CSNs schemes made of two distinct core materials (SHF and NZF), as well as their desired “structure-property relationships, newly generated properties, the effect of parameter control, surface modifications, and functionalization, all of which make them useful in a wide range of applications”. Impending study to build “multi-cores/shells” based functional CSNs and to examine these nanostructures for various applications is supported and presented by this Chapter. “Medical technology, biomedical engineering, agriculture, environmental science, chemistry, materials science, physics, and electronics all benefit from nanotechnology” [9-10]. The backbone of building nano-enabled theragnostic, particularly the medication delivery system, is improved due to striking properties of CSNs. Because of their distinctive optical and magnetic features at the nanoscale, the overview of the nano-system on therapeutic development not only limits drug delivery, but also promotes and monitors drug release. CSNs have got a lot of attention in this area because of their unique and controllable properties. As a result, it's more intriguing to combine various categories of nanomaterials and create them into CSNs. Different moieties/entities can be added to CSNs to make them more functional. We compared CSNs comprised of a hard-magnetic core and a soft magnetic core with a fixed shell material in this chapter. Both the sets of CSNs have a variety of features that make them ideal for a wide range of applications. The comparison of such diverse sets of CSNs paves the way for further research into the type of CSNs known as “Magneto-fluorescent” heterostructures, which have a core made of mixed ferrites, including hard and soft ferrites, and a shell made of semiconducting material to create a new class of material with tunable magnetic and optical properties.

5.2 Experimental details

In this chapter, we compared a variety of CSNs with a core made up of two different materials and a shell made up CdS. The NZF (soft ferrite) and SHF (hard ferrite) cores were used for the core-shell synthesis. Both cores have the same shell material, which is CdS QDs. In chapter 2, the detailed synthesis procedure for both sets of CSNs has been covered. Structure, particle size, elemental composition, luminescence, magnetic properties, and functional groups of basic CdS QDs, ferrites, and their CSNs were characterised in detail using "X-ray diffraction (XRD), Transmission electron microscopy (TEM), energy dispersive analysis by X-rays (EDX), absorbance spectroscopy, photoluminescence spectroscopy, vibrating sample magnetometry (VSM) and Fourier transform infrared spectroscopy (FTIR)". "Shimadzu powder x-ray diffractometer using Cu Kα1 radiation was used to know the crystal structure and the crystallite size of prepared sample. Transmission electron microscopy (TEM) was performed by putting a drop of dilute aqueous suspension of sample on surface of 300 mesh copper grid and then copper grid was dried. TEM images were obtained using HITACHI (H-7500). Samples were characterized by EDX using HRTEM instrument TECNAI G2 20S-TWIN (FEI Netherlands) to know elemental composition of samples". "PerkinElmer Lambda750 UV–vis spectrophotometer" records "UV-vis spectra" in 200-800 nm range. Luminous behaviour of samples was recorded through "Perkin Elmer LS55 fluorescence spectrophotometer" with an excitation source of Xenon lamp in 200-900 nm range. For the validation of functionality on the external of core, shell and the core-shell "FTIR spectroscopy" was opted using "Cary 630 spectrophotometer with wavenumber region between 4000 cm^{-1} - 400 cm^{-1}".

5.3 Results and Discussion

5.3.1 Structural analysis of CdS, SHF, NZF, SHF/CdS and NZF/CdS CSNs

The XRD spectra for the two types of cores, shell and CSNs with fixed CdS QDs shell, are shown in Figure 5.1 The CSNs created with NZF/CdS and SHF/CdS, respectively, were explored in the preceding chapters (3 and 4). In this chapter, we have compared the CSNs of hard ferrite-based core (SHF) and soft ferrite-based (NZF) CSNs. Figure 5.1 (a) demonstrate the "XRD spectra" for the bare NZF and SHF annealed at two different temperatures. Figure 5.1 (b) demonstrate the "XRD spectra" for the CSNs with both the ferrites core. Figure 5.1 (c)

demonstrates the “XRD spectra” for the CdS QDs. Figure 5.2 shows the crystal structures for (a) NZF, (b) SHF and (c) CdS QDs.

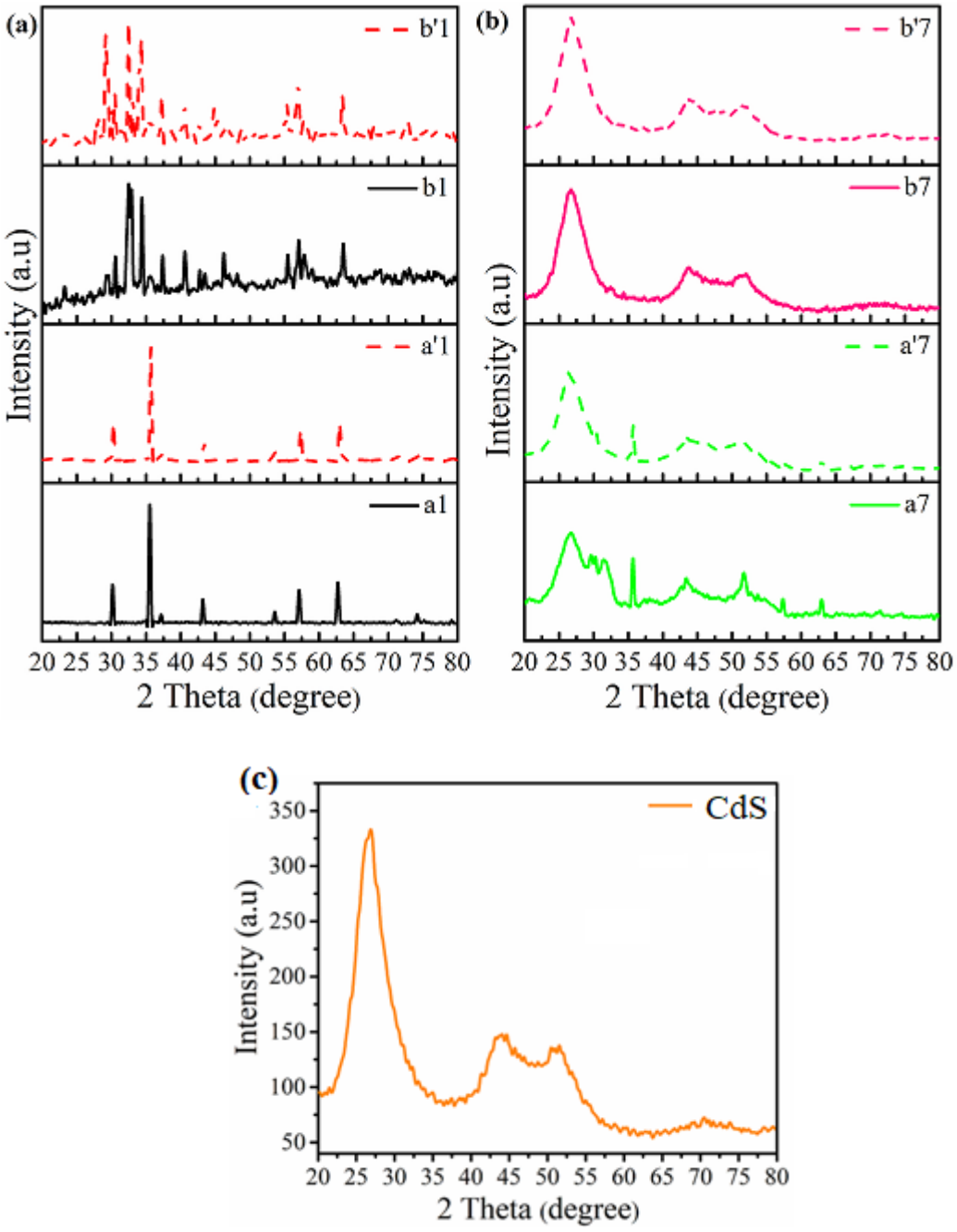

Figure 5.1: Shows the XRD spectra for the prepared nanostructures

The labels that were used to discuss the samples are as follows:

(a1: a’1): XRD spectra of NZF core annealed at 900°C and 1100°C respectively

(b1: b’2): XRD spectra of SHF core annealed at 900°C and 1000°C respectively

(a7: a’7): XRD spectra of CSNs with 0.05 g NZF core loading and CdS2 shell, with NZF annealed at 900°C and 1100°C respectively

(b7: b'7): XRD spectra of CSNs with 0.05 g SHF core loading and CdS2 shell, with NZF annealed at 900°C and 1000°C respectively

(c): XRD spectra of CdS2

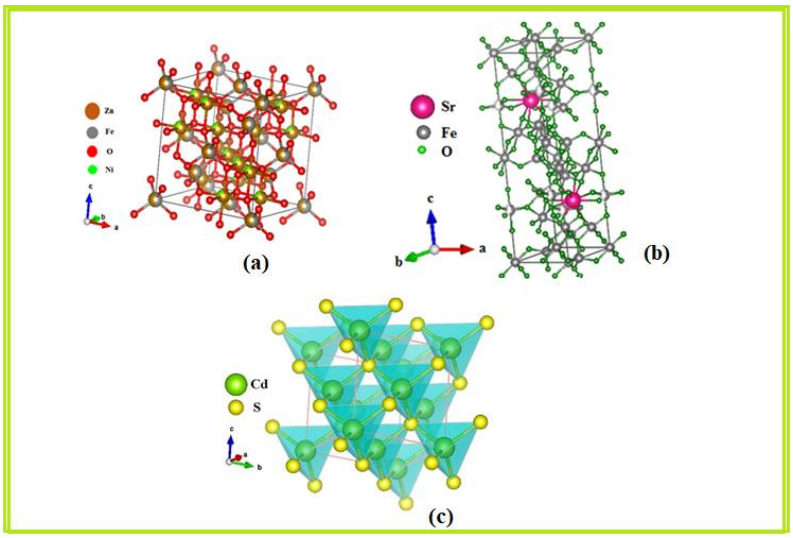

Figure 5.2: Shows the crystal structures for (a) NZF, (b) SHF and (c) CdS QDs

Table 5.1 shows the results of various parameters determined using "Rietveld refinement" of the respective samples. Soft ferrites have cubic symmetry and, as a result, three easy axes, whereas hard ferrites have hexagonal atomic structure and uniaxial anisotropy. When compared to hard ferrite-based CSNs, the GOF for soft ferrite-based CSNs is nearly ideal. This is due to the fact that hard ferrite has a significantly more complex structure than soft ferrite.

Table 5.1: Summary of various parameters calculated using "Rietveld refinement"

Composition		Lattice Parameter		Cell Volume	Phase Fraction	R_B	R_F	GOF	χ^2
		a (Å)	b (Å)	V (A^3)	(%)				
a3 (CdS2) (SG: *F-43m*)		5.9	--	212.4	100	3.6	3.1	1.1	1.4
a1(NZF) 900°C (SG: *F-43m*)		8.3	--	588.2	100	4.3	3.7	1.4	1.6
a'1(NZF) 1100°C (SG: *F-43m*)		8.3	--	581.5	100	3.9	3.4	1.3	1.5
a7 NZF/CdS 900°C	CdS	5.8	--	199.2	95.6	6.3	4.5	1.8	2.3
	NZF	8.3	--	583.8	4.3				
a'7 NZF/CdS 1100°C	CdS	5.8	--	197.5	94.7	4.8	3.2	1.3	1.6
	NZF	8.3	--	583.9	5.2				
b1(SHF) 900°C (SG: 63/mmc)		5.4	23.0	157.46	100	4.3	3.7	2.9	2.3
b'1 (SHF) 1000°C (SG: 63/mmc)		5.5	23.8	166.37	100	3.9	3.4	3.6	2.5
b7 SHF/CdS 900°C	CdS	5.8	--	199.2	94.5	6.3	4.5	3.8	3.2
	SHF	5.0	22.7	125	4.37.6				
b'7 SHF/CdS 1000°C	CdS	5.8	--	197.5	92.3	4.8	3.2	3.9	3.6
	SHF	5.1	22.8	132.65	5.28.1				

5.3.2 Morphological analysis

Figure 5.3 displays TEM image of CSNs made with NZF and SHF as the core. TEM pictures of NZF/CdS CSNs with cores annealed at 900°C and 1100°C are shown in micrographs (a) and (b). CSNs show some diffused boundaries in micrograph (a), whereas the boundaries between core and shell are very sharp in micrograph (b), indicating that the core-shell formed with NZF annealed at 1100°C is much intact, with core and shell completely separated from each other, and thus validating the PL results. In SHF/CdS CSNs micrographs (c and d) both the micrographs are showing the perfect core-shell formation with sharp interface between them. The elemental analysis also revealed that the core-shell nanostructures generated with SHF have a substantially superior stoichiometry than those formed with NZF (discussed in chapter 3 & 4).

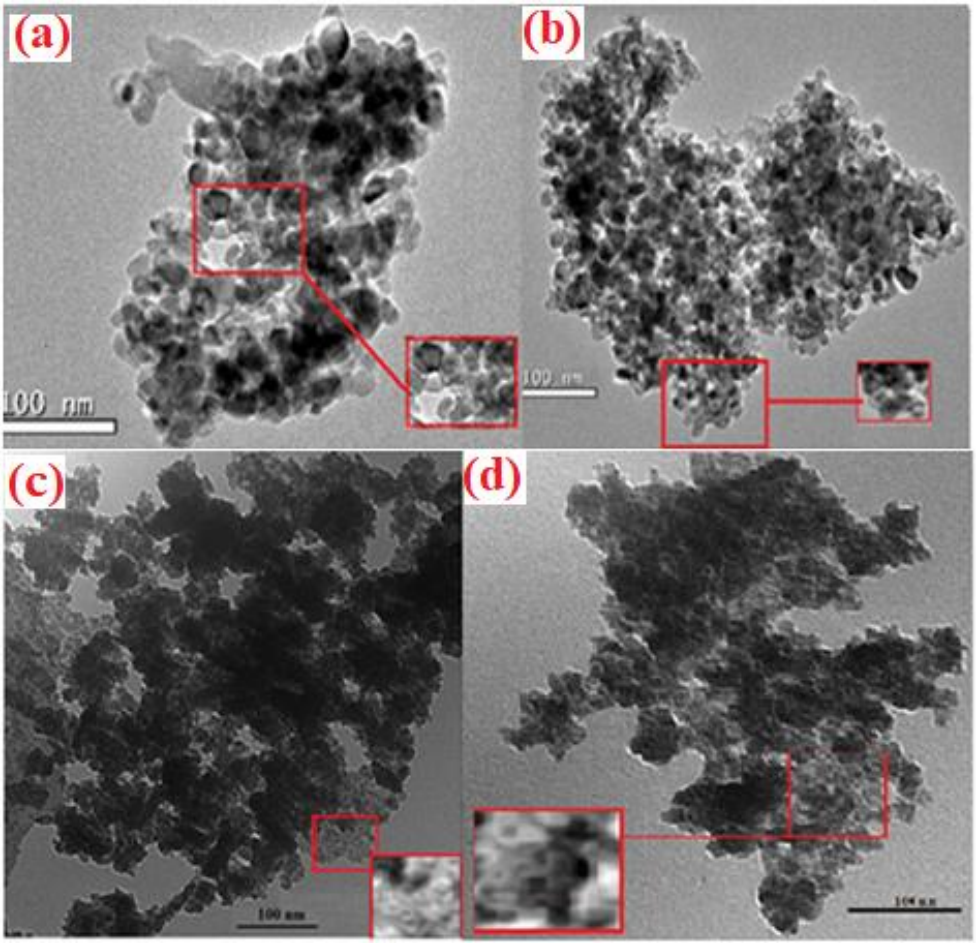

Figure 5.3: (a and b) Show the HRTEM images for the CSNs with 0.05 g NZF loading and CdS2 shell where SHF is being annealed at 900°C and 1100°C respectively. **(c and d)** Show the HRTEM images for the CSNs with 0.05 g SHF loading and CdS2 shell where SHF is being annealed at 900°C and 1000°C respectively

5.3.3 Optical studies

5.3.3.1 Absorbance spectroscopy

The UV–vis spectra of several CSNs, as well as CdS QDs, are presented in Figure 5.4 absorbance profile for the shell and CSNs in the range of 350–800 nm is shown in Figure 5.4. (a1, a2, and a3) when the core is annealed at 900ºC and 1100ºC/1000ºC. We have discovered the deviations in the absorbance maxima of shell and the CSNs using this technique while comparing different groups of samples. "CdS QDs according to its band gap shows the absorbance maxima near 450 nm. While with the core-shell formation there is a shift in the absorbance maxima, this might be due to the substrate effect of core nanoparticle" [11]. In the CSNs, MNPs serve as a substrate for CdS nanoparticle development. The 2nd derivative spectra for the two separate sets of CSNs are shown in picture 5.4 (a1, a2, and a3), which offer us with the more improved and sharp details of the absorbance spectra. Derivatized bands that are observed to be suppressed in fundamental absorbance spectra are clearly represented.

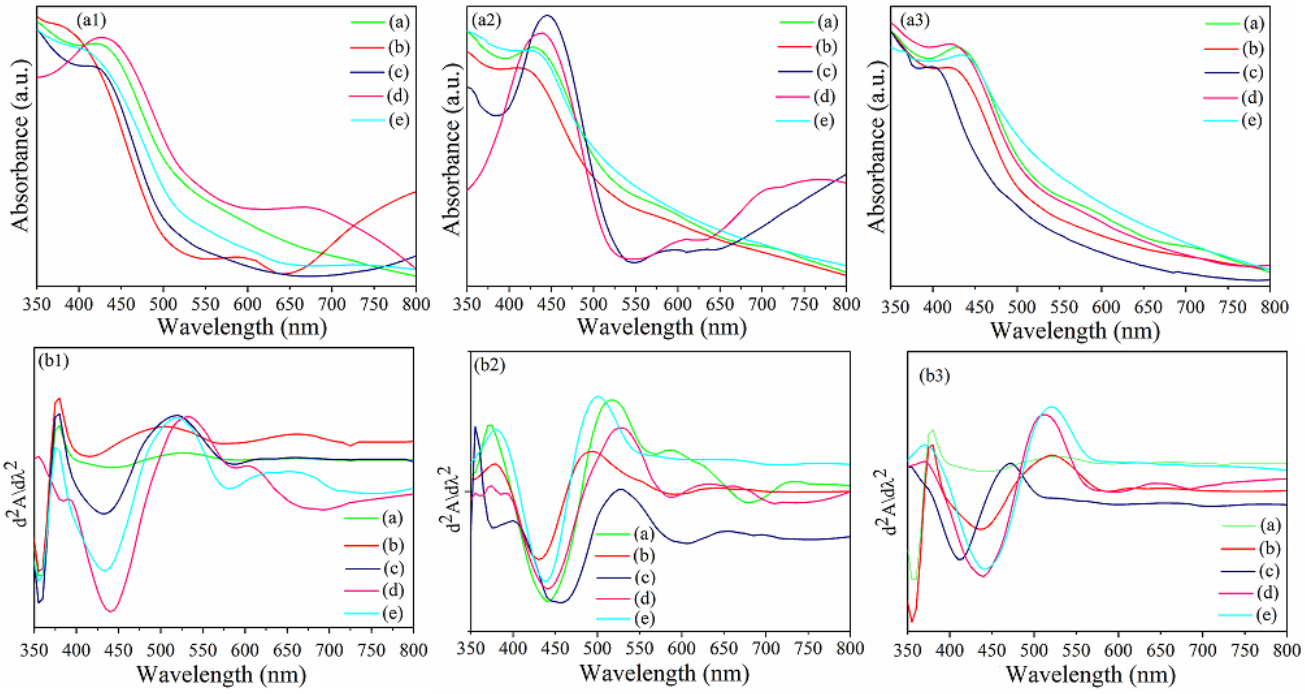

Figure 5.4: Shows the "UV-vis spectra" for prepared nanostructures

The labels that were used to discuss the samples are as follows:

Figure (a1): PL spectra for CdS2 shell and CSNs of CdS2 with 0.2 loading of NZF core annealed at 900ºC and 1100ºC respectively and SHF core annealed at 900ºC and 1000ºC respectively

(a) is CdS 2

(b)is the CSNs; 0.2 NZF with CdS2 with core annealed at 900ºC

(c) is the CSNs; 0.2 NZF with CdS2 with core annealed at 1100°C

(d)is the CSNs; 0.2 SHF with CdS2 with core annealed at 900°C

(e) is the CSNs; 0.2 SHF with CdS2 with core annealed at 1000°C

Similarly **(A2) and (A3)** follow the same trend of labelling only the loading is varied 0.1 g in **A2** and 0.05 g in **A3**

5.3.3.2 Photoluminescence spectroscopy

PL spectra for the shell and CSNs of the CdS shell with both cores are shown in Figure 5.5 (A1, A2, and A3). All of the emission spectra were documented at a static wavelength of 350 nm. The emission profile of all CSNs is similar to that of the CdS shell. When comparing the different sets of CSNs, it was discovered that the "interface between the core and shell, the substrate effect of the core, and the different sized shell produced over the core surface all cause differences in emission" [12-13]. When it comes to the development of CSNs, SHF-based nanostructures have a better particle size distribution than NZF-based CSNs. Due to the intermixing of core and shell elements, CSNs produced with 0.2 g NZF loading and NZF annealed at 900°C display a strong peak of ZnS. When the same sample is annealed at 1100°C, however, this peak is missing, and the core-shell merely follows the CdS emission profile.

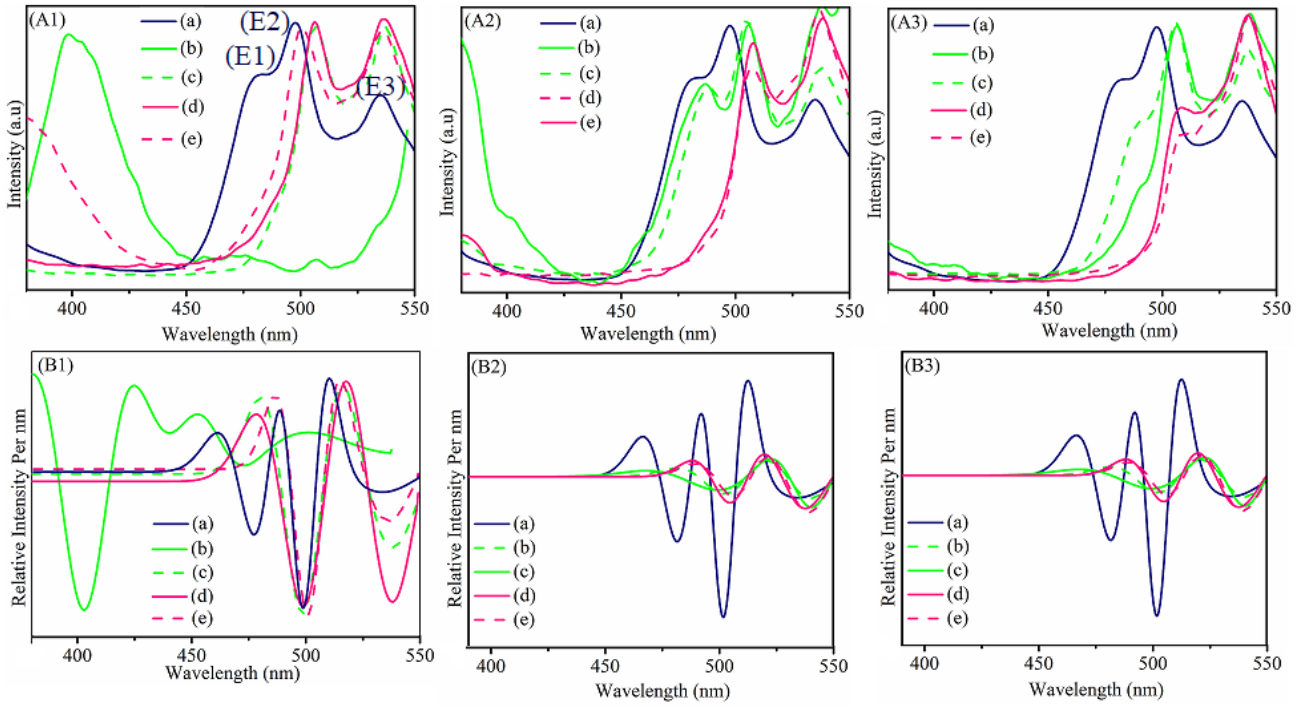

Figure 5.5: Shows the Photoluminescence spectra for prepared nanostructures with most prominent emission peaks being represented by E1, E2 and E3 in each profile

The labels that were used to discuss the samples are as follows:

Figure (A1): PL spectra for CdS2 shell and CSNs of CdS2 with 0.2 loading of NZF core annealed at 900°C and 1100°C respectively and SHF core annealed at 900°C and 1000°C respectively

(a) is CdS 2

(b)is the CSNs; 0.2 NZF with CdS2 with core annealed at 900°C

(c) is the CSNs; 0.2 NZF with CdS2 with core annealed at 1100°C

(d)is the CSNs; 0.2 SHF with CdS2 with core annealed at 900°C

(e) is the CSNs; 0.2 SHF with CdS2 with core annealed at 1000°C

Similarly **(A2) and (A3)** follow the same trend of labelling only the loading is varied 0.1 g in **A2** and 0.05 g in **A3**

Figure (B1, B2 and B3) shows the PL derivative of the same samples

Table 5.2. Summary of the various parameters by the mean of emission peaks profiles of the several samples

S. No		Sample name	Peak positions (nm)			Intensities (a.u.)		
			E_1	E_2	E_3	I_1	I_2	I_3
1.	CdS2	a3	469.10	488.65	535.71	175	214	164
2.	NZF/ CdS	a31/a'31	413.64/-	-/490.30	-/532.71	163.23/--	-/90.2	-/63.23
		a32/a'32	464.4/470.32	490.05/489.08	532.30/532.71	171.2/165.32	210.5/212.23	89/76
		a33/a'33	468.92/471.82	490.95/489.08	533.78/533.13	163.23/163.24	209.23/208.44	150.21/156.36
3.	SHF/ CdS	a31/a'31	-	489.17/492.30	533.59/532.13	-	120.30/90.2	132.02/63.23
		a32/a'32	-	489.94/491.15	532.13/533.81	-	211.51/210.21	92.02/79.32
		a33/a'33	-	489.17/491.40	532.13/532.81	-	209.23/208.44	150.21/156.36

When we annealed the core at a higher temperature, the core and shell remained quite intact. There is no intermixing in any of the samples of SHF-based CSNs. The emission profile of CdS is followed by all of the core-shell nanostructures. Peak positions and intensities of PL data have been presented in Table 5.2. The 2nd order differential spectra for the fundamental PL emission profile are shown in Figure 5.5 (A1, A2 & A3) DSM is utilised to precisely resolve elementary bands in experimental photoluminescence spectra. The DSM has made it possible to discuss some of the aspects that were previously invisible or muted in PL spectra. We're getting good luminescence qualities that are similar to those of CdS QDs spectra.

5.3.4 Magnetic Studies

The hysteresis loops for the SHF and NZF cores annealed at two distinct temperature ranges are shown in Figure 5.6. (A1). The large discrepancy in the width of the hysteresis curve between the loops shows a different type of core ferrite. The nature of magnetism is depicted by the width of the hysteresis loop. The hard-magnetic character of SHF is indicated by the increased width of the SHF hysteresis curve. The nature of coercivity and saturation magnetization in both sets of ferrites is distinct. In the case of NZF, less coercivity is acquired with high magnetization, but in the case of SHF, high coercivity is obtained with low saturation magnetization.

The hysteresis curve for CSNs made with both types of core materials is shown in Figure 5.6. (A2, A3 & A4). All the CSNs have the same parameter trend as their naked entity, except saturation magnetization has faded. The development of a magnetically dead layer of semiconducting CdS over the core causes the magnetization to decline in all of the samples. In comparison to NZF based CSNs, SHF based CSNs have a lower SFD value. The smaller the SFD value, the better the particle size distribution in a given sample [14-15]. As a result, we can state that SHF-based CSNs have a superior particle size distribution than NZF-based CSNs. This is also supported by the PL findings discussed earlier.

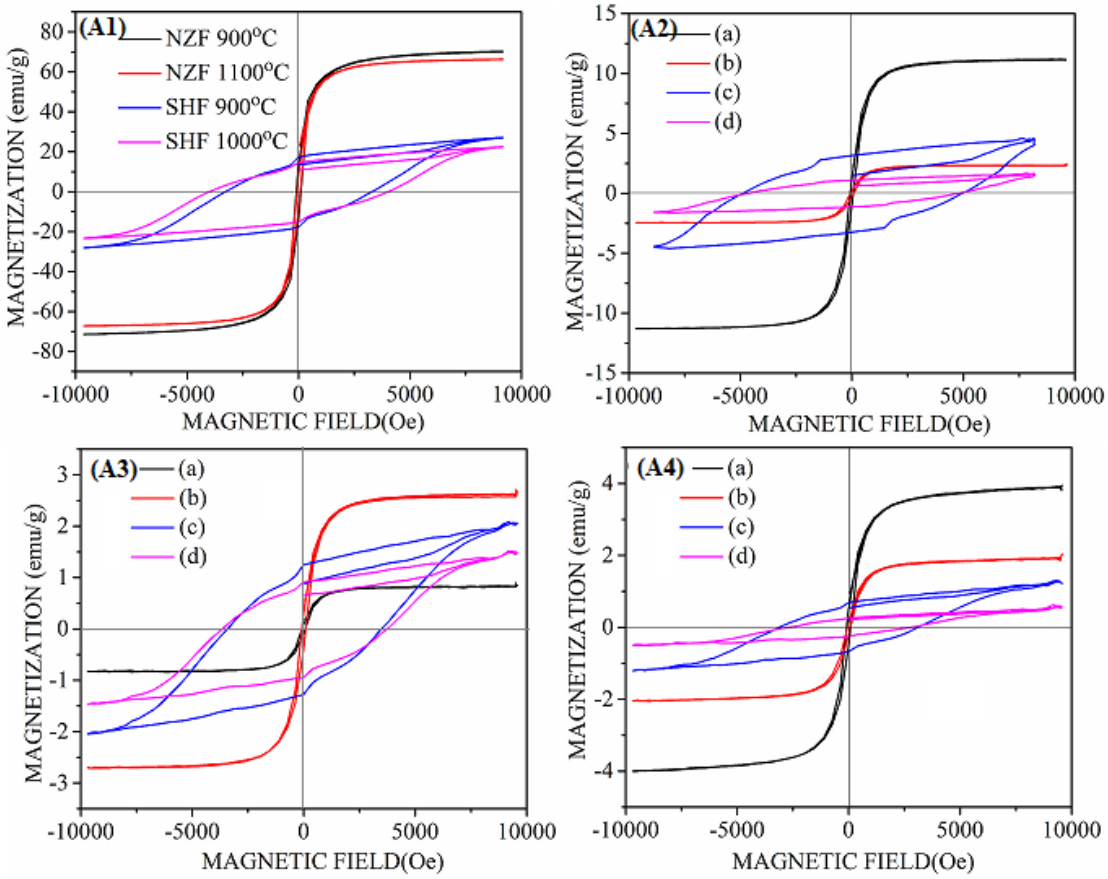

Figure 5.6: Hysteresis curve for the core and the CSNs

The labels that were used to discuss the samples are as follows:

Figure (A1): Hysteresis curve for NZF and SHF core annealed at 900ºC and 1100ºC/1000ºC respectively

Figure (A2): Hysteresis curve for the CSNs. In which **(a and b)** are hysteresis for CSNs of CdS2 with 0.2 loading of NZF core annealed at 900ºC and 1100ºC respectively and **(c and d)** are hysteresis for CSNs of CdS2 with 0.2 loading of SHF core annealed at 900ºC and 1000ºC respectively

Similarly, Figure (A3) and (A4) follow the same trend of labelling only the loading is varied from 0.1 g in **A3**and 0.05 g in **A4**

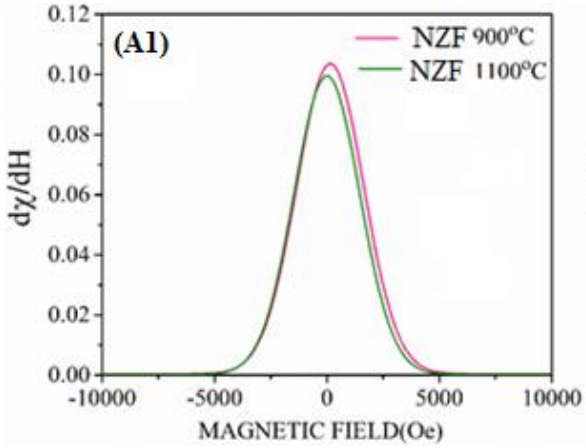
(A1)
NZF 900°C
NZF 1100°C
dχ/dH
MAGNETIC FIELD(Oe)

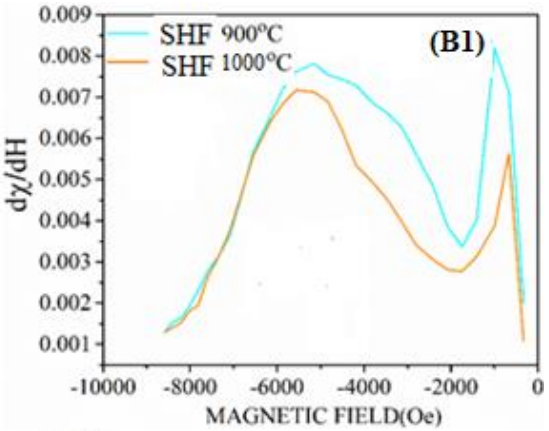
(B1)
SHF 900°C
SHF 1000°C
dχ/dH
MAGNETIC FIELD(Oe)

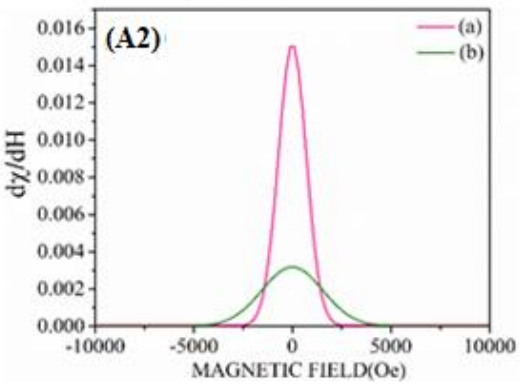
(A2)
(a)
(b)
dχ/dH
MAGNETIC FIELD(Oe)

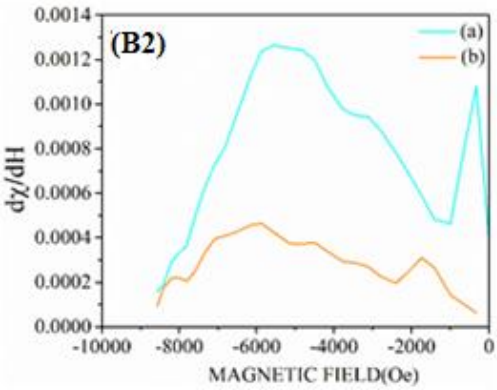
(B2)
(a)
(b)
dχ/dH
MAGNETIC FIELD(Oe)

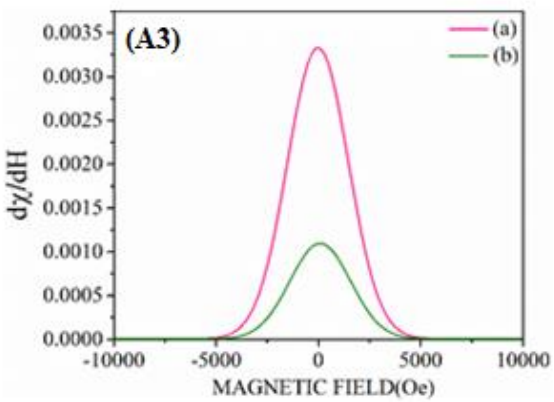
(A3)
(a)
(b)
dχ/dH
MAGNETIC FIELD(Oe)

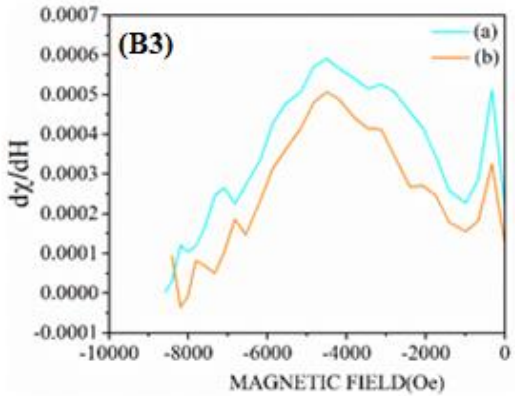
(B3)
(a)
(b)
dχ/dH
MAGNETIC FIELD(Oe)

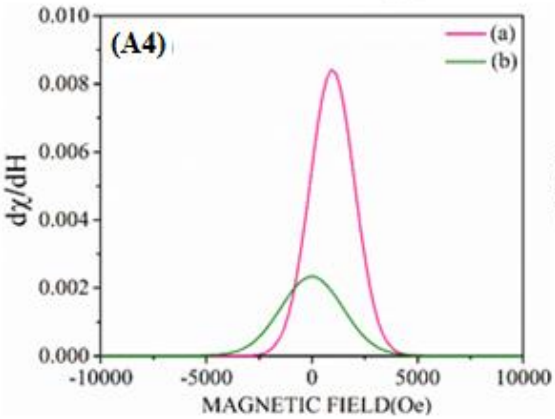
(A4)
(a)
(b)
dχ/dH
MAGNETIC FIELD(Oe)

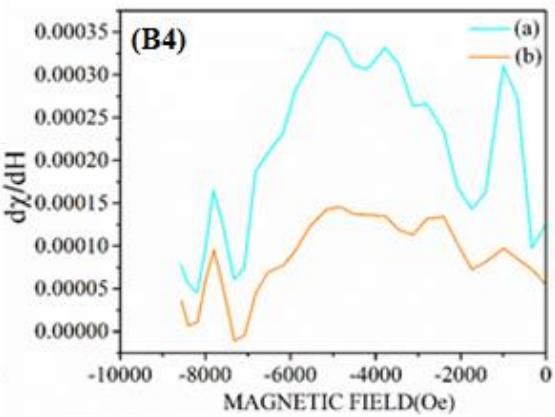
(B4)
(a)
(b)
dχ/dH
MAGNETIC FIELD(Oe)

Figure 5.7: Shows the 1st order derivative of hysteresis curve for the core and the CSNs

The labels that were used to discuss the samples are as follows:

(A1: B1) shows the 1st order differential hysteresis curve for NZF core annealed at 900°C and 1100°C respectively and SHF core annealed at 900°C and 1000°C respectively

(A2: B2) shows the 1st order differential hysteresis curve for core shell; NZF loading of 0.2 g and shell of CdS2, NZF core annealed at 900°C and 1100°C respectively and SHF loading of 0.2 g and shell of CdS2, SHF core annealed at 900°C and 1000°C respectively

(A3:B3) and (A4: B4) follow the same trend of labeling only the loading is varied from 0.1 g in **A3:B3** and 0.05 g in **A4:B4**

The magnetic field vs susceptibility graphs obtained are shown in Figure 5.7. It shows the difference in magnetic susceptibility for different CSNs with variable ferrite loading w.r.t., to applied field. The derivative curve for NZF and NZF-based CSNs has a steeper peak from the FWHM of which, we derived the SFD values for the samples.

The derivative curve of SHF and SHF-based core-shell nanostructures always have a broad hump followed by a steeper peak [16-17]. The broad hump is the indication of hard magnetic behaviour of ferrite [18]. The squareness value for SHF and SHF/CdS CSNs is more than 0.5, showing that SHF is hard-magnetic [19-20]. The squareness value for NZF and NZF/CdS CSNs is less than 0.5 for all samples. Indicating NZF's gentle magnetic nature [21].

Table 5.3: Magnetic parameters of ferrite (900°C and 1000°C), and their CSNs

S No	Sample	M_{max} (emu/g)	M_r (emu/g)	H_c (Oe)	M_r/M_{max}	K (erg/cm^3)	SFD
1.	SHF1000°C	22.87	14.74	3722.79	0.64	42570.10	0.21
2.	SHF 900°C	27.55	11.45	3037.79	0.41	41845.55	0.24
3.	NZF 1100°C	70.16	13.04	98.98	0.18	3472.12	2.53
4.	NZF 900°C	66.35	6.45	73.16	0.09	2427.02	2.68
5.	SHF (0.2) CdS2 1000°C	1.59	0.95	3335.62	0.59	2651.81	0.13
6.	SHF (0.2) CdS2 900°C	4.52	2.79	3514.31	0.61	7942.34	0.14
7.	NZF (0.2) CdS2 1000°C	3.5	0.25	2501.71	0.5	625.42	1.63
8.	NZF (0.2) CdS2 900°C	10.19	0.67	2888.88	0.56	1718.88	1.62
9.	SHF (0.1) CdS2 1000°C	1.45	0.92	3365.40	0.63	2439.91	0.09
10.	SHF (0.1) CdS2 900°C	2.01	1.25	3156.92	0.62	3172.70	0.08
11.	NZF (0.1) CdS2 1000°C	0.81	0.08	69	0.09	27.94	1.58
12.	NZF (0.1) CdS2 900°C	2.65	0.33	84.5	0.12	111.96	1.69
13..	SHF (0.05) CdS2 1000°C	0.5	0.25	2501.71	0.5	625.42	0.05
14.	SHF (0.05) CdS2 900°C	1.19	0.67	2888.88	0.56	1718.88	0.24
15.	NZF (0.05) CdS2 1000°C	1.96	0.14	64	0.07	62.72	1.56
16.	NZF (0.05) CdS2 900°C	3.91	0.44	91	0.11	177.90	1.58

5.3.5 FT-IR Studies

The FT-IR spectra for pure SHF, NZF, and their CSNs are illustrated in Figure 5.7 “Spinel ferrites have two broad oxygen metal bands in their FTIR spectra. As a result, the one detected at v1=606 cm^{-1} corresponds to the metal ion's inherent stretching vibration at the T-sites, while the lowest band, observed around v2=460 cm^{-1}, is assigned to octahedral metal stretching vibration” [22-23]. “The band near 3388 cm^{-1} corresponds to H_2O's O–H stretching vibration; the particular absorption peak at 2339 cm^{-1} relates to citric acid's O–H group” [24-25]. The adsorption of CdS QDs on the exterior of SHF/NZF causes a minor shift in the absorption bands of CSNs when linked to their basic systems (MNPs). Characteristic bands for the corresponding samples were discovered in the finger print region. We discovered the maximum peaks of the CdS shell on the surface in CSNs.

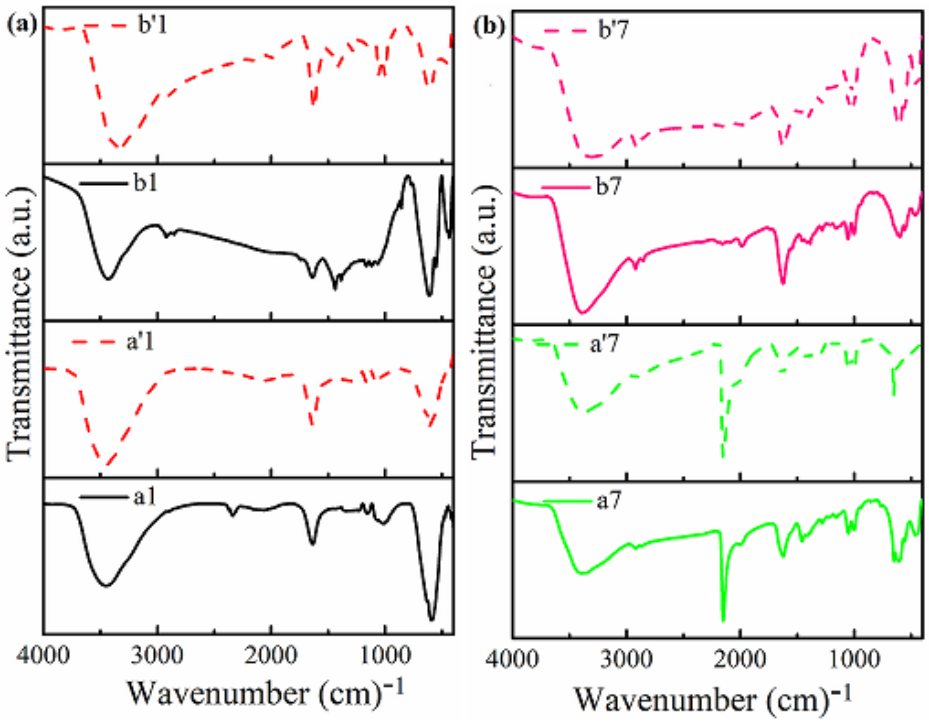

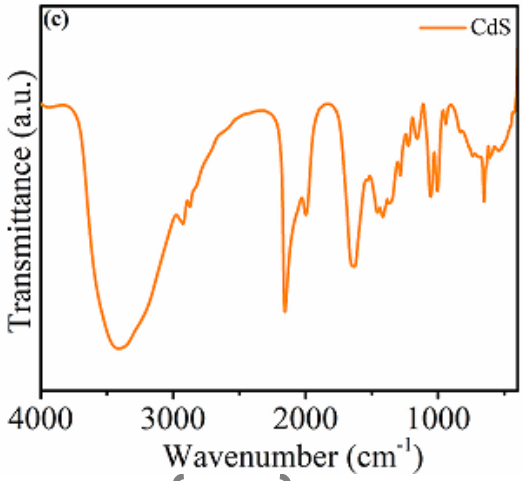

Figure 5.8: (a), (b) and **(c)** shows the FTIR spectra of synthesized nanostructures

The labels that were used to discuss the samples are as follows:

(a1: a'1): FTIR spectra for NZF core annealed at 900°C and 1100°C respectively

(a2: a'2): FTIR spectra for SHF core annealed at 900°C and 1000°C respectively

(b1: b'1): FTIR spectra for CSNs with 0.05 g NZF loading and CdS2 shell, with NZF annealed at 900°C and 1100°C respectively

(b2: b'2): FTIR spectra for CSNs with 0.05 g SHF loading and CdS2 shell, with NZF annealed at 900°C and 1000°C respectively

(c): FTIR spectra for the CdS QDs

5.4 Conclusion

- Innovative nanostructures with a CdS shell over NZF or SHF core have been created.
- The coexistence of both phases (ferrite and QDs) in the nanostructures is confirmed by the XRD for shell, core, and CSNs.
- Because of the difference in the nature of cores for both sets of CSNs, optical, magnetic, and structural data show significant differences.
- In optical and magnetic analysis, 2nd order derivative spectroscopy is employed for detailed study of the samples.
- The functional group found in "FT-IR spectra" of the CSNs spectra is largely attributable to the exterior constituent, which is CdS, indicating that shell is efficaciously grownup overhead SHF/NZF providing strong sign for CSNs construction.
- The comparative study paves the way to explore a new avenue that is single core shell nanostructure in which properties coercivity, retentivity and magnetic saturation can be tailored according to the field of application.

5.5 REFERENCES

[1] Cho, N.H., Cheong, T.C., Min, J.H., Wu, J.H., Lee, S.J., Kim, D., Yang, J.S., Kim, S., Kim, Y.K. and Seong, S.Y., *A multifunctional core–shell nanoparticle for dendritic cell-based cancer immunotherapy*. Nature nanotechnology, vol. 6(10), pp.675-682, Oct. 2011.

[2] Hao, R., Xing, R., Xu, Z., Hou, Y., Gao, S., & Sun, S., *Synthesis, functionalization, and biomedical applications of multifunctional magnetic nanoparticles.* Advanced materials, vol. 22(25), pp. 2729-2742, Jul. 2010.

[3] Chatterjee, K., Sarkar, S., Rao, K. J., & Paria, S., *Core/shell nanoparticles in biomedical applications*. Advances in colloid and interface science, vol. 209, pp. 8-39, Jul. 2014.

[4] Issa, B., Obaidat, I. M., Albiss, B. A., & Haik, Y., *Magnetic nanoparticles: surface effects and properties related to biomedicine applications.* International journal of molecular sciences, vol. 14(11), pp. 21266-21305, Nov. 2013.

[5] Kale, A., Kale, S., Yadav, P., Gholap, H., Pasricha, R., Jog, J.P., Lefez, B., Hannoyer, B., Shastry, P. and Ogale, S., *Magnetite/CdTe magnetic–fluorescent composite nanosystem for magnetic separation and bio-imaging*. Nanotechnology, vol. 22(22), p.p. 225101, Apr. 2011.

[6] Mahdavi, M., Ahmad, M. B., Haron, M. J., Namvar, F., Nadi, B., Rahman, M. Z. A., & Amin, J., *Synthesis, surface modification and characterisation of biocompatible magnetic iron oxide nanoparticles for biomedical applications.* Molecules, vol. 18(7), pp. 7533-7548, Jul. 2013.

[7] Xia, H., Tong, R., Song, Y., Xiong, F., Li, J., Wang, S., ... & Wu, J., *Synthesis and bio-applications of targeted magnetic-fluorescent composite nanoparticles*. Journal of Nanoparticle Research, Vol. 19(4), pp. 149, Apr. 2017.

[8] Kumar, R., Mondal, K., Panda, P. K., Kaushik, A., Abolhassani, R., Ahuja, R., ... & Mishra, Y. K., *Core–shell nanostructures: perspectives towards drug delivery applications.* Journal of Materials Chemistry B, vol. 8(39), pp. 8992-9027, 2020.

[9] Liu, E., Yuan, H., Kou, Z., Wu, X., Xu, Q., Zhai, Y., ... & Zhai, H., *Investigation on spin dependent transport properties of core-shell structural Fe_3O_4/ZnS nanocomposites for spintronic application.* Scientific reports, vol. 5(1), pp. 1-11, Jun. 2015.

[10] Chen, X., Lou, Y., Samia, A. C., & Burda, C. (2003). *Coherency strain effects on the optical response of core/shell heteronanostructures.* Nano Letters, vol. 3(6), pp. 799-803, Jun. 2003.

[11] Israelsen, N. D., Hanson, C., & Vargis, E. *Nanoparticle properties and synthesis effects on surface-enhanced Raman scattering enhancement factor: an introduction*. The Scientific World Journal, Jan. 2015.

[12] Rawat, D., Sethi, J., Sahani, S., Barman, P. B., & Singh, R. R. *Pioneering and proficient magneto fluorescent nanostructures: Hard ferrite-based hybrid structures*. Materials Science and Engineering: B, vol. 265, pp. 115017, Mar. 2021.

[13] Rawat, D., & Singh, R. R., *Avant-grade magneto/fluorescent nanostructures for biomedical applications: Organized and comprehensive optical and magnetic evaluation.* Nano-Structures & Nano-Objects, vol. 26, pp. 100714, Apr. 2021.

[14] Kumar, S., Singh, R. R., & Barman, P. B., *Reitveld Refinement and Derivative Spectroscopy of Nanoparticles of Soft Ferrites (MgNiFe).* Journal of Inorganic and Organometallic Polymers and Materials, vol. 31(2), pp. 528-541, Feb. 2021.

[15] Lake Shore Cryotronics Inc. "Measuring Magnetic Media Using a VSM". AZoM. https://www.azom.com/article.aspx?ArticleID=4959. 2020.

[16] Neupane, D., Ghimire, M., Adhikari, H., Lisfi, A., & Mishra, S. R. *Synthesis and magnetic study of magnetically hard-soft SrFe12-yAlyO19-x Wt.% Ni0. 5Zn0. 5Fe2O4 nanocomposites*. AIP Advances, vol. 7(5), pp. 055602, May. 2017.

[17] S. Torkian, A. Ghasemi, R. S. Razavi., *Magnetic properties of hard-soft SrFe10Al2O19/Co0. 8Ni0. 2Fe2O4 ferrite synthesized by one-pot sol–gel auto combustion*, J. Magn. Magn, vol. 416(2016), pp. 408-416, 2016.

[18] Dahal, J. N., Neupane, D., & Mishra, S. R. *Exchange-coupling behavior in SrFe12O19/La0. 7Sr0. 3MnO3 nanocomposites*. Ceramics, vol. 2(1), pp. 100-111, Mar. 2019.

[19] Tannous, C., & Gieraltowski, J., *The Stoner–Wohlfarth model of ferromagnetism.* European journal of physics, vol. 29(3), 475, Mar. 2008.

[20] Li, D., Pan, D., Li, S., & Zhang, Z., *Recent developments of rare-earth-free hard-magnetic materials.* Science China Physics, Mechanics & Astronomy, vol. 59(1), pp. 617501, Jan. 2016.

[21] Mohapatra, J., & Liu, J. P., *Rare-Earth-free permanent magnets: the past and future.* Handbook of magnetic materials, vol. 27, pp. 1-57, Jan. 2018.

[22] De, M., Mukherjee, A., & Tewari, H. S. *Characterization of cadmium substituted nickel ferrites prepared using auto-combustion technique*. Processing and Application of Ceramics, vol. 9(4), pp. 193-197, 2015.

[23] Waldron, R. D. (1955). Infrared spectra of ferrites. *Physical review*, vol. *99*(6), pp. 1727, Sep. 1995.

[24] Devendran, P., Alagesan, T., Ravindran, T. R., & Pandian, K., *Synthesis of spherical CdS quantum dots using cadmium diethyldithiocarbamate as single source precursor in olive oil medium.* Current Nanoscience, vol. 10(2), pp. 302-307, Apr. 2014.

[25] Nejati, K., & Zabihi, R., *Preparation and magnetic properties of nano size nickel ferrite particles using hydrothermal method.* Chemistry Central Journal, vol. 6(1), pp. 1-6, Dec. 2012.

CHAPTER-6

SUMMARY AND FUTURE SCOPE

1. Formulation of the problem
2. Work Plan
3. Implementation of research work
4. Synthesis and Characterization
5. Results and Interpretations
6. Future research

6.1 Summary

The aim of the thesis was to give the most up-to-date information on core-shell multifunctional nanostructures. The aqueous solvent approach was used to make the CSNs. The application zone of nanostructures is expanded by using water as a solvent in the synthesis process. This magnet inside semiconductor type model of CSNs satisfies the demand for simultaneous targeting and tracking, proving to be a very important tool in "targeted-drug-delivery" and MRI applications. Optical and magnetic results demonstrated that CdS QDs were successfully deployed on the surface of the core MNPs, with an obvious attachment evident in all results, as well as high core and shell stability and intactness.

Chapter 1 briefly introduced QDs, Ferrites, and CSNs, as well as other significant ideas, while Chapter 2 outlined the synthesis and characterization techniques step by step. All QDs, ferrites, and CSNs may be successfully manufactured using a wet chemical aqueous approach, as discussed in Chapter 2. The results for these samples are presented in Chapters 3, 4, and 5.

The "seed mediate growth approach", which combines "sol-gel" and "solution growth methods", was used to successfully construct magneto-fluorescent CSNs of NZF/CdS through an aqueous route, resulting in better magneto-fluorescent characteristics. Using a simple and controlled manner, the generation of single-phase cubical spinel structure in NZF and cubical structure in CdS, as well as the creation of CSNs, are inveterate by "XRD spectra." The effect of varied core loadings on structural characteristics has been demonstrated in CSNs. "UV–visible spectroscopy" shows a red shift in maximum absorption as core loading increases, which is further verified by "PL spectroscopy". Optical studies demonstrated that the CSNs generated are firm and have boosted luminescence, with the best results coming from the least quantity of base material used. Magnetic investigations demonstrate that as a result of semiconductor shell creation to the exterior of the magnetic core, saturation magnetization deteriorates, indicating that the shell above the core has grown successfully. The production of ferromagnetic NZF/CdS nanostructures was confirmed using VSM. NZF/CdS nanostructures have been studied for spin-dependent characteristics utilising derivative of susceptibility. When the largest amount of NZF is applied and the annealing temperature of NZF is lower, the CSNs formed have diffused borders. Both the NZF and CdS relate spin-to-

spin at the interface. CSNs were shown to be much firm when only a small amount of core was loaded and the annealing temperature of the core was raised. According to FTIR research, the functional groups present on the system are promising for further processing these "magneto-fluorescent" CSNs for biological applications. Overall, these "magneto-fluorescent" CSNs could be employed in "spintronics as well as drug administration, diagnostics, and imaging applications in nanomedicine, according to the researches".

The effective synthesis and characterization of hard ferrite-based strontium hexaferrite/CdS multifunctional CSNs with magnetic and optical capabilities in a single entity are demonstrated in Chapter 4. The creation of CSNs is well supported by the results obtained through various characterizations. The shell, which is CdS QD, has a well-defined cubical phase, while the strontium hexaferrite core has a hexagonal phase, according to structural specifications. The optical results from "UV–visible spectroscopy" and "PL spectroscopy" accord well with the generation of CSNs. Particle size dispersal is get enhanced with the development of CSNs, as evidenced by PL data. With nominal core loading, better outcomes are obtained. The hard-magnetic character of the $SrFe_{12}O_{19}$ core has been confirmed by magnetic experiments. Because of the totally diamagnetic character of CdS, it was also proven that CdS is grown precisely over $SrFe_{12}O_{19}$ because the magnetic saturation decays after CdS production. This is also a clear indicator of the creation of the CSNs. The first order derivative of the fundamental hysteresis loop is used to calculate SFD. The information on spin orientation at high and low magnetic fields is provided by SFD. "FTIR spectra" allocated important bands. The development of CSNs is strongly supported by an alteration in the absorption band in "FTIR spectra". We determined that these CSNs can be used in a variety of sectors, including "spintronics and biological cell sorting applications where a persistent magnetic field is required", after analysing their structural, optical, and magnetic properties. The comparative examination of two separate sets of CSNs created with different kind of cores was presented in Chapter 5 (hard magnetic and soft magnetic core-based nanostructures respectively). Because low ferrite loading CSNs produce the greatest outcomes in both CSNs, this chapter compares CSNs created with minimal ferrite loading.

Table 6.1: Table Summarized the various results concluded after characterizing different set of samples

Samples	Structural Properties	Magnetic Properties	Optical Properties	Morphological Study
NZF/CdS	• Highly crystalline phases of NZF/CdS nanostructures achieved for CSNs with core annealed at 1100°C. • Nanostructures formed with core annealed at 900°C are not much intact.	• Hysteresis loop shows the Soft magnetic nature of NZF. • Decaying magnetization with the CSNs formation is the direct proof of CSNs.	• CSNs formed with 0.2 g loading with core annealed at 900°C shows ZnS peak due to the intermixing of core and shell. • CSNs formed with core annealed at 1100°C are stable and intact.	• CSNs formed with core annealed at 1100°C shows much sharp interface in HRTEM micrographs as compared to same CSNs formed with core annealed at 900°C .
SHF/CdS	• Acquired well-defined highly crystalline phases of SHF/CdS nanostructures.	• Hysteresis loop shows the hard magnetic nature of SHF.	• CSNs formed with core annealed at both the temperatures are highly stable . • All the set of CSNs follow the emission profile of CdS with better luminescent and better particle size distribution.	• CSNs micrographs shows sharp interfaces. • Higher degree of agglomeration is found in SHF based CSNs as compared to NZF based CSNs.

6.2 Future scope

The following are some key points that can be applied to this research issue in the future:

- Encapsulation of these CSNs by peptides and other biocompatible groups.
- These CSNs could be connected to specific biomolecules in the future to examine certain cell types *in-vitro*.
- These nanostructures could be employed for cell sorting.
- Magnetic nanoparticles (SHF/NZF) can be utilised to make spring magnets, which have a wide range of uses.
- Synthesis of magneto-fluorescent CSNs with the core made of mixed ferrites which includes hard and soft ferrites; and the shell with CdS quantum dots will be prepared and characterized to attain a new class of material with tuneable magnetic and optical properties. Figure 6.1. shows the schematic for the spring magnet design.

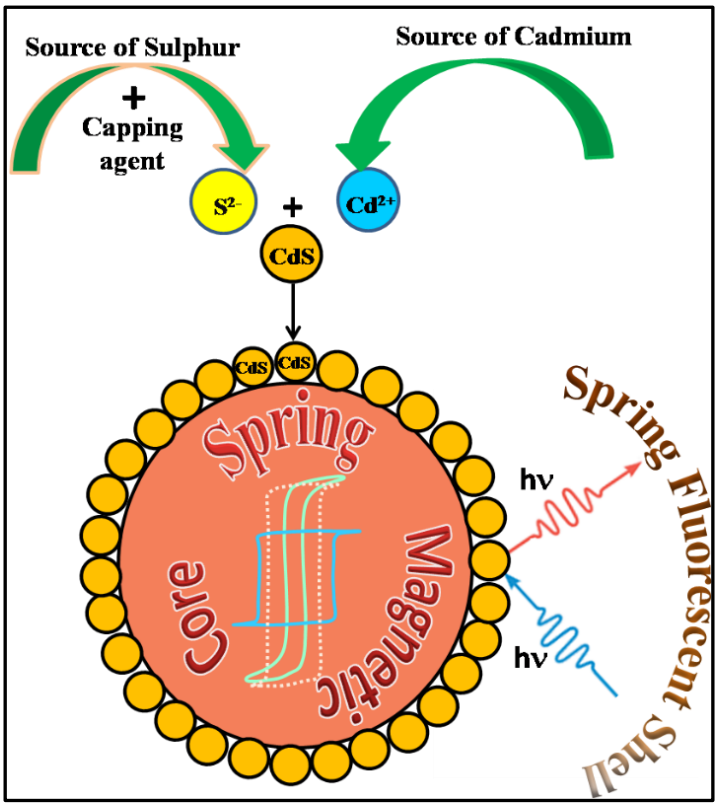

Figure 6.1: Future work conceptualization